University of California
Santa Barbara

Development of a tip-enhanced near-field optical microscope for nanoscale interrogation of surface chemistry and plasmonic phenomena

A dissertation submitted in partial satisfaction
of the requirements for the degree

Doctor of Philosophy
in
Chemical Engineering

by

Alexander Lee Heilman

Committee in charge:

Professor Michael J. Gordon, Chair
Professor Song-I Han
Professor Samir Mitragotri
Professor Megan T. Valentine

June 2017

The Dissertation of Alexander Lee Heilman is approved.

Professor Song-I Han

Professor Samir Mitragotri

Professor Megan T. Valentine

Professor Michael J. Gordon, Committee Chair

May 2017

Development of a tip-enhanced near-field optical microscope for nanoscale interrogation of surface chemistry and plasmonic phenomena

by

Alexander Lee Heilman

To graphene ... (just kidding)

Acknowledgements

Seven years is a long time. But despite the countless frustrations and challenges that inevitably accompany such a long PhD process, I can safely say that I would not change a thing. I am eternally grateful for the experience I have had here at UCSB, in large part because of the wonderful people I have had the privilege to meet and work with throughout my time in Santa Barbara. Without their support and friendship, I doubt I would have made it through the trying experience that is grad school.

First and foremost, I owe an enormous debt of gratitude to my adviser, Dr. Michael Gordon. Mike, your immense knowledge and jack-of-all-trades engineering prowess have been impressive and inspirational to me, as they surely are to everyone who has ever worked closely with you. Thinking back to when I first joined the group, I'm always struck by how much I have learned—from science to cars to whiskies—and grown as a scientist and engineer under your guidance. Not only have you been a supportive and understanding mentor to me these many years, but you have also been a true friend. Thank you for everything.

I have also been extremely fortunate these past few years to have had the opportunity to work alongside some of the absolute best people in the world. Fed, you've been like a brother to me—not least of all regarding the relentless teasing—and I am confident that grad school was merely the beginning of a friendship that will last a lifetime. Katie, you are one of the most genuine and kind people I have ever had the pleasure of knowing, and though our habit of constantly distracting one another may have ultimately added a few months to each of our PhDs, always having you around to talk to has helped me maintain my sanity throughout this long process, especially when the going got tough. Pebbles, you have been not only an excellent and loyal friend but also a role model to me, both in an out of lab; your work ethic, self-discipline, resilience, and humility have been inspiring

and have made me strive to be a better person. Rich, your brilliant scientific mind and methodical approach to the TERS project have been invaluable to my success these last few years. Our countless research discussions never failed to improve my understanding of the field and often helped me refine my project in ways I had not considered. More importantly, though, your friendship and wonderfully dry sense of humor have helped make every day in the Gordon Lab more enjoyable. Chris, Louis, Isaac, and Travis, thank you for taking me under your wing all those years ago when I first joined the group and was helplessly inept at science in general (and of course, Chris, I would be remiss if I did not take the opportunity to acknowledge how your unrivaled wit brightened even the most mundane of group meetings and email threads). And to the rest of the Gordon Group, it has been a privilege to work with and get to know you all. I am sad to say farewell to such an intelligent and fun bunch, but I am confident that the future of the group is in excellent hands.

I am so grateful for my amazing family and for the undying support and love they provided throughout this roller coaster of a process. Mom and Dad, you helped me celebrate and appreciate the high points and accomplishments, but more importantly, you offered comfort, wisdom, and love to help me push through the lows. Chip and Tina, your endless encouragement and genuine enthusiasm for my work have meant the world to me. I love you all.

I am immeasurably thankful for the unwavering support of my wonderful and loving partner. Alice, you believed in me, even—rather, especially—when I did not. Your endless optimism and encouragement helped me overcome the largest obstacle I have ever faced: writing this damn book. I could not have done it without you. I love you with all my heart.

I would like to thank the countless friends and colleagues here in Santa Barbara who have helped make these last seven years the best of my life. In particular, Edward, you

have been a one-in-a-million friend—not to mention the linchpin of seemingly my entire social network—and I cannot image what my grad school experience would have been like without you...nor do I want to.

Lastly, I would like to thank my horrible, horrible cat, whose unwavering indifference toward me has been humbling, even by grad school standards.

Curriculum Vitæ
Alexander Lee Heilman

Education

2010–2017 **Ph.D.** in Chemical Engineering, University of California, Santa Barbara
2016–2010 **B.S.** in Chemical Engineering, University of Kentucky (*summa cum laude*)

Publications

1. **A. L. Heilman**, M. J. Gordon, "Dynamic measurement of gap plasmon resonance characteristics in ATR-illuminated tip-enhanced near-field optical microscopy," In progress.
2. **A. L. Heilman**, M. J. Gordon, "Tip-enhanced near-field optical microscope with side-on and ATR-mode sample excitation for super-resolution Raman imaging of surfaces," *J. Appl. Phys.* **2016**, 119, 223103.
3. A. C. Comer, **A. L. Heilman**, D. S. Kalika, "Dynamic relaxation characteristics of polymer nanocomposites based on poly(ether imide) and poly(methyl methacrylate)," *Polymer* **2010**, 51, 5245-5254.
4. V. A. Kusuma, B. D. Freeman, S. L. Smith, **A. L. Heilman**, D. S. Kalika, "Influence of TRIS-based co-monomer on structure and gas transport properties of cross-linked poly(ethylene oxide)," *J. Membr. Sci.* **2010**, 359, 25-36.

Presentations

Talk *"Probing the optical near-field to achieve nanoscale chemical imaging."*
Clorox-Amgen Graduate Student Symposium Santa Barbara, CA **2015**

Poster *"Design of a tip-enhanced Raman spectroscopy system for nanoscale chemical imaging."*
Clorox-Amgen Graduate Student Symposium Santa Barbara, CA **2014**

Poster *"Investigation of graphene as a novel substrate for near-field optical experiments."*
Center for NanoScience (CeNS) Workshop Venice, Italy **2012**

Talk *"Investigation of dynamic relaxation properties of poly(methyl methacrylate)/silica nanocomposites."*
AIChE Southern Regional Conference Raleigh, NC **2010**

Poster *"Investigation of dynamic relaxation properties of poly(methyl methacrylate)/silica nanocomposites."*
AIChE National Conference Nashville, TN **2009**

Poster *"Effect of developer bias on toner development in EP printing."*
Lexmark Student Symposium Lexington, KY **2008**

Awards

2014	**Best Poster** Clorox-Amgen Graduate Student Symposium
2010	**Oswald Paper Competition (First Place)** Physical and Engineering Sciences Category
2009 – 2017	**Tau Beta Pi** Member
2006 – 2010	**Dean's List (all semesters)** University of Kentucky
2006 – 2010	**Presidential Scholarship** University of Kentucky

Technical Skills

Synthesis, Fabrication & Characterization

AFM • Optical microscopy • Raman/fluorescence spectroscopy • SEM
CVD • Photolithography • E-beam/thermal evaporation • Surface functionalization

Instrument Design & Construction

Optical systems design/prototyping | CAD | Machining | Interfacing/programming

Software & Programming

LabVIEW | Lumerical | Mathematica | MATLAB | Origin | SketchUp | LaTeX

Abstract

Development of a tip-enhanced near-field optical microscope for nanoscale interrogation of surface chemistry and plasmonic phenomena

by

Alexander Lee Heilman

Optical microscopy and spectroscopy are invaluable tools for the physical and chemical characterization of materials and surfaces in a wide range of scientific disciplines. However, the application of conventional optical methods in the study of nanomaterials is inherently limited by diffraction. Tip-enhanced near-field optical microscopy (TENOM) is a hybrid technique that marries optical spectroscopy with scanning probe microscopy to overcome the spatial resolution limit imposed by diffraction. By coupling optical energy into the plasmonic modes of a sharp metal probe tip, a strong, localized optical field is generated near the tip's apex and is used to enhance spectroscopic emissions within a sub-diffraction-limited volume. In this thesis, we describe the design, construction, validation, and application of a custom TENOM instrument with a unique attenuated total reflectance (ATR)-geometry excitation/detection system. The specific goals of this work were: (i) to develop a versatile TENOM instrument capable of investigating a variety of optical phenomena at the nanoscale, (ii) to use the instrument to demonstrate chemical interrogation of surfaces with sub-diffraction-limited spatial resolution (i.e., at super resolution), (iii) to apply the instrument to study plasmonic phenomena that influence spectroscopic enhancement in TENOM measurements, and (iv) to leverage resulting insights to develop systematic improvements that expand the ultimate capabilities of near-field optical interrogation techniques.

The TENOM instrument described herein is comprised of three main components:

an atomic force microscope (AFM), a side-on confocal Raman microscope, and a novel ATR excitation/detection system. The design of each component is discussed along with the results of relevant validation experiments, which were performed to rigorously assess each component's performance. Finite-difference time-domain (FDTD) optical simulations were also developed and used extensively to evaluate the results of validation studies and to optimize experimental design and instrument performance. By combining and synchronizing the operation of the instrument's three components, we perform a variety of near-field optical experiments that demonstrate the instrument's functionality and versatility. ATR illumination is combined with a plasmonic AFM tip to show that: (i) the tip can quantitatively transduce the optical near-field (evanescent waves) above the surface by scattering photons into the far-field, (ii) the ATR geometry enables excitation and characterization of surface plasmon polaritons (SPPs), whose associated optical fields are shown to enhance Raman scattering from a thin layer of copper phthalocyanine (CuPc), and (iii) SPPs can be used to plasmonically excite the tip for super-resolution chemical imaging of patterned CuPc via tip-enhanced Raman spectroscopy (TERS). ATR-illumination TERS is quantitatively compared with side-on illumination. In both cases, spatial resolution was better than 40 nm and tip-on/tip-off Raman enhancement factors were >6500. Furthermore, ATR illumination was shown to provide similar Raman signal levels at lower "effective" pump powers due to additional optical energy delivered by SPPs to the active region in the tip-surface gap.

We also investigate the sensitivity of the TENOM instrument to changes in the plasmonic properties of the tip-surface system in the strongly-coupled regime at small tip-surface separations. Specifically, we demonstrate detection of a resonant plasmonic tip-surface mode (a gap plasmon) that dramatically influences the optical response of the system, and we use experimental results and FDTD simulations to support a hypothesized mechanism. Moreover, we confirm that the gap plasmon resonance has a strong

effect on the enhancement of both fluorescence and Raman scattering, and we propose that this phenomenon could ultimately be exploited to improve sensitivity in super-resolution chemical imaging measurements. Finally, we recommend a straightforward modification to the TENOM instrument that could enable future application of these gap-mode plasmon resonances to increase spectroscopic enhancements by an order of magnitude.

Contents

Chapter 1

Introduction to near-field optical methods

1.1 Thesis goals and outline

The need to image surfaces and materials is ubiquitous across nearly all disciplines of the hard sciences, and our ability to visualize materials with ever-increasing spatial resolution has led to countless scientific advances and breakthroughs. In recent years, as the lengthscale of state-of-the-art science has shrunk far into the nanoscale, the need for robust, high-resolution imaging and material characterization techniques has increased dramatically. While optical techniques are extremely useful for many applications, not least of all because of the rich chemical information that spectroscopy can provide, they are inherently limited when studying nanoscale materials because of diffraction. Thus, the imaging of nanomaterials is dominated by non-optical techniques, such as electron microscopy and scanning probe microscopy (SPM), which can resolve features on the order of angstroms. However, these techniques provide limited chemical information, if any at all, which limits their utility in fields like biology, where the nanoscale spatial

distribution of chemical groups on a multifunctional surface can have profound influence on behavior. As such, there is considerable scientific need for imaging techniques that provide the chemical specificity of optical spectroscopy with nanoscale spatial resolution.

One approach to meet this need is to develop imaging techniques that are sensitive to the unique optical phenomena that occur at the nanoscale, a regime known as the optical near-field. Tip-enhanced near-field optical microscopy (TENOM) is a hybrid technique that marries optical spectroscopy and scanning probe microscopy to overcome the spatial resolution limit imposed by diffraction. By coupling optical energy into the plasmonic modes of a sharp metal probe tip, a strong, localized optical field is generated at the tip's apex and is used to enhance spectroscopic emissions within a sub-diffraction-limited volume. In this work, we outline the design, validation, and successful application of a custom TENOM instrument that can be used for optical and chemical interrogation of surfaces with sub-diffraction-limited spatial resolution (super-resolution). The specific goals of the project are as follows:

1. Design and construct a TENOM instrument that combines an atomic force microscope (AFM), a confocal Raman microscope, and a unique attenuated total reflection (ATR)-geometry illumination system for controlled excitation and detection of near-field phenomena.

2. Demonstrate the instrument's ability to locally enhance and measure surface chemistry with nanoscale spatial resolution by performing correlated topographic and Raman imaging of a nanostructured, chemically patterned surface.

3. Evaluate the instrument's ability to excite and measure a variety of near-field optical phenomena using the ATR system and compare experimental results with both theory and simulations.

4. Quantitatively compare the use of ATR and side-on illumination configurations for chemical imaging experiments with emphasis on their relative signal strengths, enhancement factors, and spatial resolution.

5. Use the TENOM instrument to investigate the optical properties of the coupled tip-surface system at short separation distances, particularly as they pertain to plasmonic behavior and spectroscopic enhancement.

Before discussing any specifics of the instrument design or experimental results, the remainder of this chapter will focus on background concepts necessary to understand and appreciate the later chapters. It will also provide a brief overview of the current state of the art of nanoscale imaging techniques, with emphasis on how the above goals seek to contribute to the literature and progress the field of near-field optical microscopy. Chapter 2 focuses on the design and construction of two components of the TENOM instrument (the AFM and the Raman microscope) and discusses the results of several validation studies used to assess the performance of each sub-system. More importantly, we also demonstrate the combined operation of the two components to achieve nanoscale chemical imaging of a patterned surface. Chapter 3 begins by discussing the motivation for the addition of the ATR-geometry excitation/detection system and briefly describes the theory behind several unique phenomena that can be studied with such a system. We then detail the design and validation of the ATR system, with emphasis on the use of theory and numerical simulations to assess its performance.

In Chapter 4, all three components of the TENOM instrument (AFM, Raman microscope and ATR system) are combined to achieve chemical and topographical imaging of a surface using two different excitation geometries: side-on (conventional) and via the ATR system. We quantitatively assess the relative performance of the two geometries by comparing signal strength, spatial resolution, and Raman enhancement factors, and we

show that both are viable. In Chapter 5, we discuss a very different application of the TENOM instrument made possible by the unique ATR system: the direct study of tip-light interactions in the optical near-field, including the observation and characterization of a special type of optical mode, called a gap plasmon. Furthermore, we investigate the correlation between the optical behavior (*i.e.*, frequency response) of the gap plasmon and the enhancement of fluorescence and Raman scattering. Results suggest that careful optimization of the gap plasmon resonance could yield dramatic signal gain in a variety of future TENOM experiments. Finally, in Chapter 6, we summarize the potentially impactful results of this work and briefly discuss future directions and applications of the TENOM instrument.

1.2 The state of the art of imaging and localized surface interrogation

A variety of techniques exist for imaging and local characterization of surfaces and materials over a range of lengthscales. This section will provide a brief overview of three broad classifications of commonly used imaging techniques and will discuss the strengths and limitations of each as they pertain to chemical specificity and spatial resolution.

1.2.1 Conventional optical techniques

Optical microscopy is the most widespread imaging technique in most fields of the hard sciences and is particularly ubiquitous in biology and medicine. In addition to being relatively inexpensive and highly customizable, optical methods provide another major benefit: through the use of spectroscopy, they can provide a rich depth of information about the physical and chemical structure of materials. A variety of spectroscopic

techniques exist that measure the absorption and/or emission of light in the UV to IR range to determine a wide variety of material properties, such as chemical composition and functionality, molecular conformations and stacking orientations, lattice strain, and defect concentrations.

One of the most common spectroscopic methods for chemical identification of organic compounds is infrared (IR) absorption spectroscopy (see Figure 1.1), in which a broadband IR source passes through a sample, and the wavelength-dependent transmittance of the sample is measured. This yields an absorption spectrum that provides detailed information regarding molecular vibration energies, which can not only determine the presence of certain bonding groups, but can also serve as a "chemical fingerprint" to identify particular molecules. Raman spectroscopy is another common vibrational spectroscopy technique that gives chemical information comparable to IR spectroscopy through a very different optical process. Raman spectroscopy makes use of an inelastic scattering process in which a photon from a monochromatic light source excites a molecule to a "virtual excited state" (not a quantum mechanical excitation but rather a momentary perturbation of the electron cloud) from which it will occasionally fall to a vibrationally excited state. When photons scatter inelastically in this way, they lose energy equal to that of the vibrational transition that is excited. Thus, by measuring the wavelength-dependent scattering from a sample relative to the energy of the excitation source, a vibrational spectrum can be obtained. While the signal obtained from Raman spectroscopy is orders of magnitude weaker than in IR absorption (only 1 in 106 photons scatter inelastically), the technique has the benefit of being much easier to localize. High magnification microscope objectives can be used to focus the Raman excitation laser to a spot less than a micron in diameter to perform local interrogation of surface chemistry.

However, in applications that require spatial resolution higher than a few hundred nanometers, Raman spectroscopy and all other conventional optical techniques are lim-

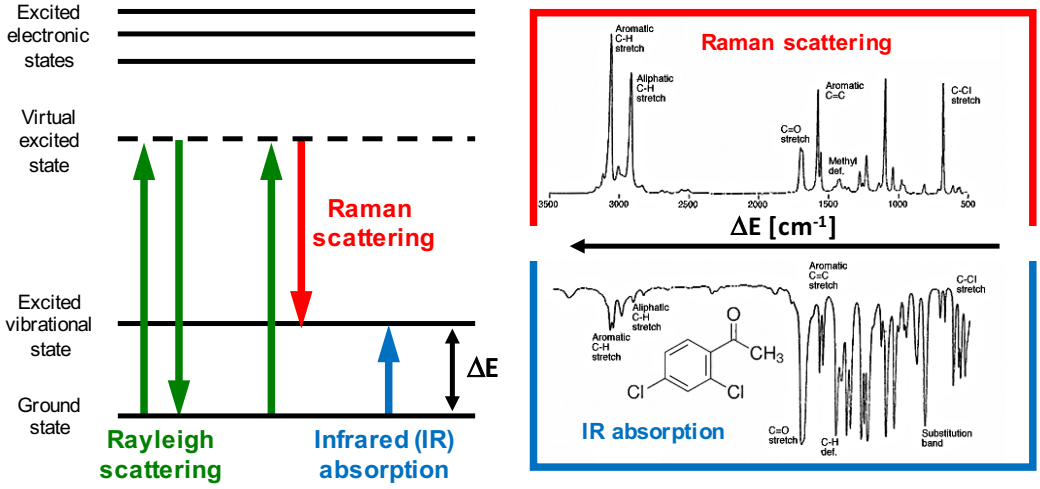

Figure 1.1: **Vibrational spectroscopies.** Left: Energy level diagrams of Rayleigh (elastic) scattering, Raman (inelastic) scattering, and infrared (IR) absorption processes. Raman scattering and IR absorption are both sensitive to the energies of vibrational excitations (ΔE). Right: Raman scattering and IR absorption spectra of 2,4 dichloroacetophenone, which demonstrate the rich chemical information attainable via vibrational spectroscopy.

ited by a fundamental problem: diffraction. As a geometric consequence of the wave nature of light, the smallest point that can be generated by converging wavefronts is limited to a diameter of roughly half the wavelength, which for visible light and state-of-the-art microscope objectives is roughly 200 nm. This makes conventional optical techniques inadequate for the visualization and local characterization of most nanomaterials. To overcome this fundamental limitation, a variety of non-optical techniques have been developed in recent years to achieve spatial resolution in the atomic regime, as will be discussed in the following section.

1.2.2 Non-optical microscopy techniques

Electron microscopies and scanning probe microscopies are by far the two of the most common families of non-optical microscopy techniques. Electron microscopies are, in many ways, directly analogous to optical microscopy, only instead of photons, they use

electrons. Since the deBroglie wavelength of a high-energy electron is orders of magnitude shorter than the wavelength of visible photons, electron microscopes can achieve much higher spatial resolution than their optical counterparts. Like photons, electrons can be controllably generated by a source, focused and steered with lenses, and measured by a variety of detectors, including spectrometers. Even electron-sample interactions, such as transmission, scattering, and x-ray generation, have direct analogs with the light-matter interactions discussed above and can be used not only to provide image contrast, but also to characterize the chemical and physical properties of materials. Electron microscopy techniques, like scanning electron microscopy (SEM) and transmission electron microscopy (TEM), have become ubiquitous in nanomaterials characterization in large part because of their high resolution and remarkable versatility; however, they are not without their limitations. Most electron microscopy techniques are performed in medium to high vacuum, which largely precludes the study of liquid-containing materials (e.g., live cells). Furthermore, many electron microscopies require certain preparation procedures, such as gold sputter-coating, that can fundamentally alter or destroy the functionality of the sample before any measurements can be done. Most importantly, the chemical information attainable with electron microscopy is limited compared to optical spectroscopies. While energy dispersive x-ray spectroscopy (EDX) can be used to provide a high resolution elemental map of the sample surface, these maps provide no information about the types of bonds or functional groups present, which makes them inadequate for the characterization of complex organic surfaces. For these reasons, the nanoscale characterization of organic surfaces is dominated by scanning probe techniques.

Scanning probe microscopy (SPM) is a broad family of non-optical imaging and characterization techniques that are used to locally interrogate surface properties by monitoring the interactions between the sample and a nanoscale probe tip near the surface. A variety of SPM techniques exist that measure different types of tip-surface interactions,

but the most prevalent—and most significant to the coming chapters—is atomic force microscopy (AFM). AFM is a family of techniques that use tip-surface mechanical forces as feedback parameters to regulate tip height while mapping sample topography and other physical properties. In part because of the breadth of available techniques, SPM offers a variety of unique benefits that electron microscopy cannot provide (though not all of the following advantages apply to all SPM techniques). In addition to the fact that SPM is non-destructive and requires no special sample preparation procedure, most SPM measurements are done at ambient conditions, and in some special cases, surfaces can even be studied in a liquid environment. Furthermore, SPM enables the local characterization of electrical and mechanical behavior and can be particularly sensitive to surface properties, such as adhesion. The in-plane spatial resolution of many SPM techniques is on the order of the physical size of the probe tip apex, which is commonly around 50 nm for commercially available probes. However, some SPM techniques, namely scanning tunneling microscopy, can achieve higher resolution than their tip geometry might suggest and are commonly used to resolve individual molecules. Despite its versatility and high resolution, SPM is not without its drawbacks. Most techniques require physical raster-scanning of the sample and simultaneous regulation of the tip height to produce an image, which often leads to imaging times of several minutes. More importantly, SPM techniques provide little or no direct chemical information about the sample.

While electron microscopy and SPM have become invaluable tools for the characterization of a wide range of nanoscale materials, their lack of chemical sensitivity often limits their utility. This shortcoming has given impetus to the recent development of a family of "super-resolution" optical microscopy techniques that cleverly overcome the diffraction limit in different ways and maintain many of the unique benefits of optical interrogation while still achieving nanoscale spatial resolution.

1.2.3 Super-resolution optical microscopy techniques

There are two broad categories of super-resolution techniques: deterministic and stochastic. Perhaps the most notable example of a deterministic super-resolution technique is stimulated emission depletion (STED) microscopy [1], which uses a two-step excitation/depletion process to controllably "shape" the region of fluorophore excitation into a nanoscale spot. In the first step, a pulsed laser is focused to a diffraction-limited spot and excites fluorophores in that region. Next, a delayed pulse from a second (lower energy) laser is focused into a ring pattern around the initial excitation spot, causing fluorophores in that region to undergo stimulated emission and return to their ground electronic state. As a result of this de-excitation process, the remaining excited fluorophores are localized to a spot many times smaller than the diffraction limit, enabling point-by-point scanning and imaging with a spatial resolution of 50 nm or better. Several other deterministic techniques exist, (*e.g.*, ground state depletion microscopy [2, 3] and saturated structured-emission microscopy [4]), that rely on other non-linear optical properties of fluorophores to precisely tune the localization of their excitation to nanoscale dimensions.

In contrast to deterministic techniques, which achieve super-resolution by manipulating the excitation of fluorophores, stochastic techniques exploit the unique temporal properties of fluorophore emission to isolate and spatially map individual emitters. These techniques operate on the principle that the spatial position of an isolated emitter can be determined with much higher accuracy than the diffraction limit by using centroid tracking image processing algorithms. However, if multiple emitters, spaced at nanoscale distances, are fluorescing simultaneously, their emission patterns overlap, and they cannot be individually resolved. Many stochastic techniques, like photoactivated localization microscopy (PALM) [5, 6] and stochastic optical reconstruction microscopy (STORM)

[7], overcome this limitation by exciting photoswitchable fluorophores in such a way that only a small subset of the fluorophores are active at any time. Since the probability of any active fluorophore being immediately adjacent to another is so low, each emitter is assumed to be isolated, and localization techniques are used to accurately identify its spatial position. By repeatedly activating different random fluorophore subsets and mapping the emitter positions in each iteration, an image is slowly constructed. While other stochastic techniques use different means to optically isolate adjacent fluorophores, they all operate on the same principle of image construction via time-resolved centroid tracking of isolated fluorophore emission.

Although these techniques have successfully pushed the limits of optical resolution well into the nanoscale regime, they are not without significant drawbacks and limitations. First, these techniques rely entirely on the labelling of samples with special fluorophores. Not only does labelling process involve complex and challenging biochemical preparation techniques to ensure fluorophore binding at (and only at) the desired locations, but it also requires an a priori knowledge about the sample itself. This requirement, along with the fact that the optical emissions from each fluorophore contain no chemical information about its local environment, precludes the application of these super-resolution techniques for the chemical interrogation of unknown materials. Thus, there remains a need for "true" super-resolution optical microscopy techniques that are capable of directly manipulating and probing the optical interactions and events that take place at nanoscale distances, *i.e.*., in the near-field regime.

1.3 Measuring the optical near-field

Important optical events, like absorption, fluorescence and scattering, occur at length-scales well below the diffraction limit, but to develop a technique that is locally sensitive

to these events, it is critically important to first understand how light behaves in the near-field regime. In this section, we describe the fundamental principles that govern the behavior of light at the nanoscale, and we discuss the importance of plasmons for the manipulation of optical fields in this lengthscale regime.

1.3.1 The optical near-field

When considering optical events at lengthscales below the diffraction limit, the transition from far-field behavior (propagating radiation) to near-field behavior is somewhat gradual and begins at roughly the wavelength of the light. The defining characteristic of the near-field is that local optical behavior is no longer dominated by the propagating components of light but is instead primarily defined by so-called evanescent optical fields. Evanescent fields (or evanescent waves) are non-propagating electromagnetic fields that oscillate at optical frequencies and decay exponentially with distance from their source. These fields are bound to surfaces and surface features and contain local optical information about their surroundings. However, because they cannot propagate, this information does not escape into the far-field and thus cannot be measured with conventional optical techniques. Nevertheless, it is possible to measure these local phenomena by bringing an optical probe into the near-field to locally excite, collect, and/or scatter the evanescent fields; this family of techniques is known as scanning near-field optical microscopy (SNOM).

There are a handful of SNOM variants that use different excitation and detection geometries to measure different characteristics of the optical near-field. In many of these techniques, a nanoscale aperture, generally formed by coating a tapered optical fiber with a thin metal layer, is used as an optical probe to confine the illumination and/or light collection to subwavelength dimensions [8–12]. Although these aperture-SNOM

techniques are sufficient to measure properties like transmittance and reflectance, the large optical losses associated with confining light to a nanoscale aperture (transmission scales with the fourth power of aperture diameter [13, 14]) make it difficult to illuminate with or collect enough light to perform spectroscopy. Thus, the utility of aperture-SNOM as a robust chemical imaging technique is inherently limited. There is, however, another class of SNOM techniques that probe local optical fields in a different way. These methods, which will be discussed in the following section, make use of the unique interactions between light and metallic nanostructures, namely the excitation of special optical modes called plasmons.

1.3.2 Plasmons

Plasmons are collective oscillations of the free electrons in a metal that are typically excited by optical fields. While plasmons can exist at any metal-dielectric interface, the plasmonic behavior of nanostructured metals and the excitation of so-call localized surface plasmons (LSPs) are particularly applicable to near-field optical methods. When light interacts with a metallic nanostructure, free electrons in the metal move in response to the associated electric field, and the electron density increases on one side of the nanostructure, giving it a local negative charge. Correspondingly, the fixed metal ions on the opposite side of the nanostructure provide an equal and opposite positive charge, leading to a dipolar electric field that opposes the initial optical field and provides a strong restoring force to the displaced electrons. Like all phenomena that involve restoring forces, this process gives rise to resonant behavior, such that nanostructures of a certain size, shape, and material will have a particular optical frequency (wavelength of light) that most efficiently excites these LSP oscillations. Under this resonant excitation condition, the coupling of light into LSP modes results in very strong dipolar electric fields in the

immediate vicinity of the nanostructure.

LSPs have several practical applications in the context of near-field optical measurements. First, by coupling light into LSP modes, optical energy can be concentrated into a small volume around a nanostructure. In the case of SNOM measurements, exciting LSPs in a sharp metallic probe generates enhanced optical fields at the tip apex, which can be used as a light source to locally interrogate the surface [15]. Since the spatial extent of this enhanced field depends primarily on the size of the tip apex, which is often on the order of tens of nanometers, this technique enables optical measurements with nanoscale resolution. Furthermore, just as plasmons provide a mechanism by which light can be converted into localized electric fields, LSPs can also facilitate the reverse process and mediate the radiation of local evanescent fields into the far-field, where they can be detected [16]. The reason that evanescent fields are non-propagating is because there are no pathways by which they are physically permitted to radiate their energy; however, the introduction of a metal SNOM tip can provide new radiative emission pathways. In the simplest case, the SNOM tip acts as an optical antenna, oscillating with the local evanescent field and radiating some of its energy into the far-field. In the special case that the evanescent field is oscillating near the tip's LSP resonant frequency, LSP modes can act as intermediaries to dramatically improve the efficiency of energy transfer from the evanescent field to the tip and subsequently increase the overall efficiency of the radiative process. Another way in which the LSP modes of a plasmonic tip can facilitate nanoscale optical interrogation is by locally enhancing spectroscopic emissions. This family of techniques, known as tip-enhanced near-field optical microscopy (TENOM), includes several common methods, such as tip-enhanced fluorescence microscopy [17] and tip-enhanced Raman spectroscopy (TERS).

1.4 Tip-enhanced Raman spectroscopy

Since the primary intended application of the TENOM instrument described in this work is to perform fundamental and applied TERS measurements, a brief discussion of the relevant principles and current state of the art of TERS are presented in this section.

1.4.1 Principles of TERS

As discussed previously, Raman spectroscopy is an inelastic scattering process that provides vibrational information similar and complementary to IR absorption spectroscopy. As such, it is a useful technique for detecting the presence of different functional groups, as well as identifying molecules by their unique Raman fingerprints. In TERS, the strong electric field generated at the apex of a plasmonic tip is used to locally enhance Raman scattering from a nanoscale region on a surface, thereby enabling super-resolution chemical interrogation. This local increase in Raman scattering occurs primarily by way of a two-step electromagnetic mechanism in which the signal is enhanced by the local field during both excitation and scattering. From the standpoint of a molecule on the sample surface, the strong dipolar electromagnetic field of tip constitutes an intense light source, and Raman excitation increases proportionally to the local field intensity, *i.e.*., with the square of the local electric field. By the opposite pathway through which the LSPs of the tip concentrate the optical excitation energy, they can also behave like an antenna to facilitate the scattering of the local Raman field into the far-field. This scattering process provides an additional signal enhancement, again proportional to the square of the local field. Thus, the overall Raman enhancement provided by the local E field of the tip is proportional to $|E_{excitation}|^2 \times |E_{scattering}|^2 \approx |E_{local}|^4$. It is because of this dramatic fourth-order Raman enhancement that TERS is a viable surface interrogation method, despite the overwhelming challenges associated with the technique.

In practice, nanoscale chemical imaging via TERS requires three components working in synchrony: (i) a scanning probe microscope to precisely control the position of the plasmonic tip relative to the sample surface, (ii) an illumination system to excite plasmons at the tip apex, and (iii) an optical detection system to collect and analyze the Raman scattered light. The generalized measurement process, illustrated schematically in Figure 1.2, is as follows:

1. The tip, which is often made of/coated with Au or Ag because of their strong plasmonic coupling with visible light, is lowered into close proximity with the sample surface.

2. The illumination system is used to focus a laser spot and align it with the tip for optimal LSP excitation.

3. The strong plasmonic fields at the tip apex locally enhance Raman scattering from the molecules near the tip-surface junction by a factor of —Elocal—4.

4. This enhanced Raman scattering, as well as the far-field (un-enhanced) Raman scattering from elsewhere in the excitation spot, is collected, generally with the same optical system used for illumination.

5. The collected light is analyzed by a monochromator to obtain a tip-enhanced Raman spectrum.

6. The tip is moved in discrete steps across the sample in either a line or raster pattern, and a Raman spectrum is collected at each position.

7. The Raman spectra are used to construct line profiles or 2D images by plotting or mapping the intensity of specific spectral (chemical) features as a function of tip position.

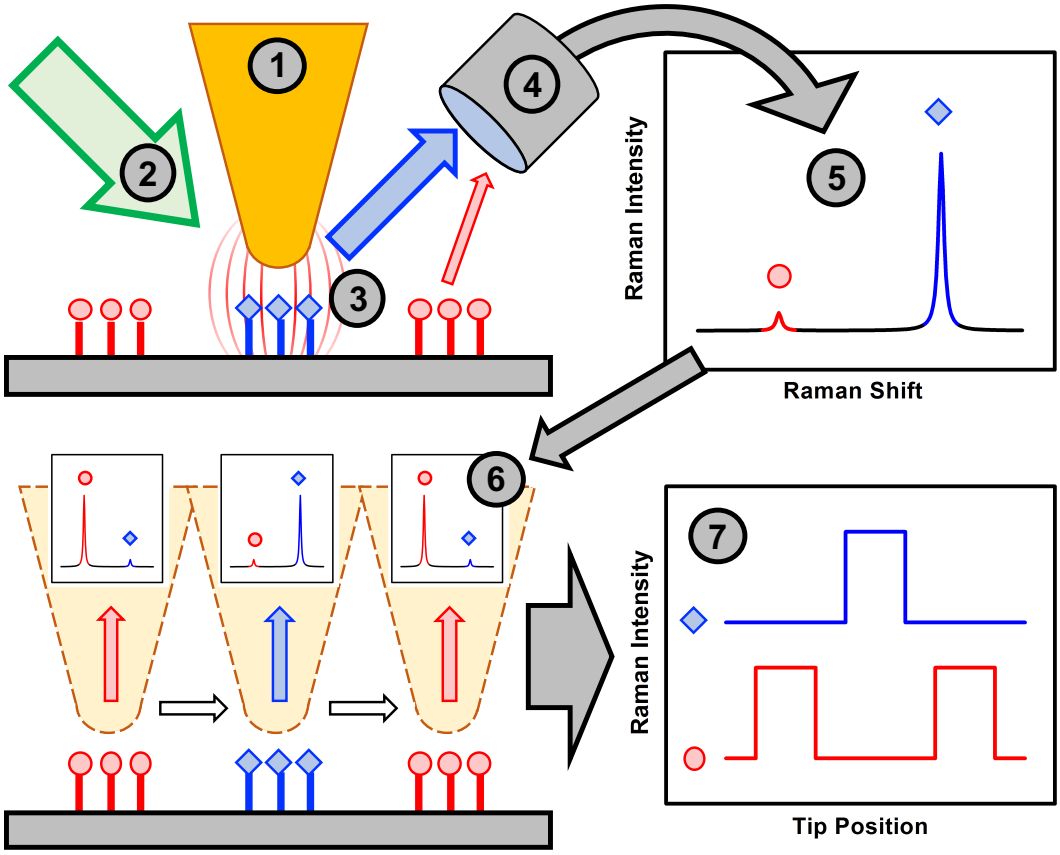

Figure 1.2: **Tip-enhanced Raman spectroscopy.** Schematic representation of the experimental procedure used to perform chemical imaging via TERS. See text for corresponding step-by-step explanation.

When chemically imaging a surface in this way, the spatial resolution depends on two factors. In a practical sense, the step size (*i.e.*., the change in tip position between subsequent Raman spectra) sets an upper bound for the resolution of a given scan, irrespective of the properties of the tip. Although the step size can be made arbitrarily small to ensure optimal resolution, there is an obvious tradeoff between pixel density and scan time/area. In a physical sense, the spatial extent of the tip's plasmonic field dictates the ultimate achievable resolution of the system; like other scanning probe techniques, this resolution depends mostly on the geometry of the tip, particularly its radius of curvature. In free space, the diameter of the plasmonically enhanced region is roughly

equal to that of the tip apex. However, when the tip is near a surface, especially if that surface is metallic, the plasmonic nature of the LSPs changes in such a way that the field concentrates in the tip-surface gap [18], shrinking to a fraction of the tip diameter and making spatial resolutions of 20–50 nm commonly attainable.

Nanoscale chemical imaging with TERS is challenging for many reasons, and a number of common issues must be carefully considered and avoided to successfully implement the technique. Given the geometric disparity between the active and background regions in TERS experiments, it is remarkable that the desired signal can be detected at all. Even in the best-case scenario, in which the excitation source is a diffraction-limited laser spot, the area of interest (at the tip apex) is no more than a few percent of the total illuminated area, and in many TERS instruments, it can be several orders of magnitude less. Therefore, to detect the enhanced Raman signal over that of the background, the local signal from the region of interest must be enhanced by several thousand times, which requires highly active plasmonic tips. Furthermore, TERS measurements must often contend with other optical emissions that can contribute significantly to the background signal. For example, fluorescence is a common phenomenon when visible wavelengths are used for excitation and is particularly pervasive in the study of biological materials; this poses a considerable problem for TERS measurements because fluorescence is more efficient than Raman scattering by several orders of magnitude. Thus, TERS interrogation of fluorescent samples often results in strong, broad spectral backgrounds that either obscure or completely overwhelm the comparatively weak Raman signals, even if they are strongly enhanced by the tip. This issue limits the application of TERS in many systems and necessitates the careful design of samples and instruments to both minimize fluorescence and maximize Raman enhancement. Despite these challenges and inherent shortcomings, TERS has been successfully applied toward the study of a wide range of material systems in the 15 years since its initial development and continues to be one of

the most promising techniques for detailed chemical characterization of surfaces at the nanoscale.

1.4.2 The state of the art of TERS

In 2000, Stöckle *et al.* published the first demonstration of TERS in which they showed a dramatic increase in Raman scattering from a thin layer of brilliant cresyl blue when a Ag tip was brought into contact with the surface [19]. Since then, TERS research has proceeded in two main directions: (i) fundamental and theoretical studies that seek to deepen the understanding of relevant principles and improve the sensitivity and resolution of the technique, and (ii) applied studies that aim to demonstrate the characterization capabilities of TERS on a diverse range of material systems. Much of the theoretical framework and understanding of TERS principles, such as Raman enhancement mechanisms and plasmon-molecule interactions, is built upon the field of surface-enhanced Raman spectroscopy (SERS), which was established in the 80's and 90's [20, 21]. However, the development of TERS provided an experimental platform with which many of the theoretical principles of SERS could be directly measured and applied in new ways. Many early studies explored the effects of a variety of factors, such as tip geometry [22, 23], surface roughness [24], tip/substrate material [25, 26], and tip-surface distance [27, 28], and used combinations of experiments, theory and numerical simulations to improve the scientific understanding of the primary mechanisms that influence TERS sensitivity.

In addition to these fundamental studies, the field was further improved by practical refinements in instrument design and experimental methods. Most notable among these experimental improvements is the development of alternative excitation geometries, each with its own advantages. The first reported TERS experiments employed a bottom illu-

mination scheme (see Figure 1.1(a)), in which an inverted optical microscope was used to excite the tip through a transparent sample. This technique has the primary benefit that a high numerical aperture (NA) objective can be used; compared to other illumination schemes, this geometry can achieve a smaller excitation spot, lower optical background, higher local field intensity at the tip, and higher collection efficiency. However, bottom illumination requires the use of transparent samples; this limitation spurred the development of alternate illumination geometries (Figure 1.3). Side-on [29], parabolic [30], and top-illumination [31] configurations can all be used to perform TERS on opaque samples. Despite the lower NA of the optics used in these configurations, the techniques are compatible with the use of metal substrates, which can couple in special ways with plasmons in the tip to provide dramatic Raman enhancements (this coupling behavior will be discussed in greater detail in Chapter 5). Furthermore, it is well known that metal substrates can also effectively quench the fluorescence of nearby analytes, which can provide a reduction in the optical background during TERS measurements and enable the study of new systems. Between instrument design refinements and improvements in the production of sharp and highly active plasmonic tips [32], the sensitivity and spatial resolution achievable by TERS has reached impressive levels in recent years, culminating in the Raman imaging of a single molecule by way of a special plasmonically-tunable ultra high vacuum TERS technique [33].

While this sort of ground-breaking fundamental research has been invaluable in refining and pushing the limits of TERS, these experiments typically make use of special analytes with strong Raman signals (*i.e.*, resonant Raman scatterers) and are often performed in highly controlled systems (e.g., single-crystal substrates, ion-milled tips). In contrast to these studies on ideal systems, many groups have instead focused on applying TERS toward the interrogation of technologically relevant nanomaterials. Many early demonstrations of applied TERS involved the study of carbon nanotubes (CNTs) and

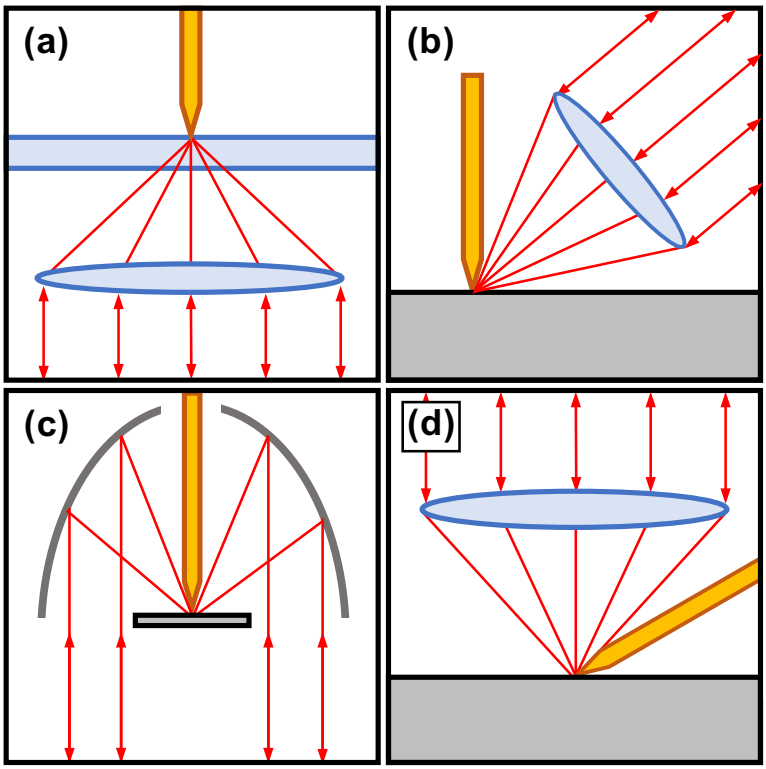

Figure 1.3: **TERS illumination geometries.** Schematic depictions of four different excitation and detection geometries used for TERS: (a) bottom illumination, (b) side-on illumination, (c) parabolic illumination, and (d) top illumination.

graphene because of the local structural information that can be inferred through the relative strengths and energies of their characteristic Raman modes [34]. Yano *et al.* applied TERS to the study of single-walled CNTs and showed that mechanical forces between the tip and a single nanowire could be used to influence the energy of its vibrational modes and improve the effective contrast and resolution of the technique [35]. Novotony *et al.* have reported on several TERS experiments on graphene, including full 2D Raman imaging of graphene layers in which they could spatially resolve local strain and defect sites [36]. In addition to structural interrogation, TERS has also shown potential for local detection of catalytic processes. By positioning a Ag TERS tip above a self-assembled monolayer on a gold surface and optically initializing a reaction at the tip apex, van Schrojenstein Lantman *et al.* were able to monitor in real time the local

catalytic reduction of the monolayer [37]. Not only has TERS been used to detect catalytic events, but also it has recently been demonstrated that the plasmonic field of the tip can itself behave as a catalyst, driving chemical reactions through the generation of "hot" electrons [38].

Lastly, considerable progress has been made in recent years in the application of TERS toward the study of biologically relevant surfaces and materials. Early studies on crystals and self-assembled monolayers of nucleobases showed that they are spectrally distinguishable by TERS [39], which suggests that the technique could, in theory, be applied to the direct sequencing of DNA and RNA strands. Although this goal is very challenging and has not yet been achieved due to several practical issues, noteworthy strides have been made in its pursuit. In 2008, Bailo *et al.* demonstrated local TERS measurements made at multiple locations along the length of a synthetic poly-cytosine homopolymer and showed that the technique was spectrally sensitive to local variations in nucleobase orientation, relative to the surface and tip [40]. Another major goal in the TERS community is to study cell membranes, or other multifunctional biological surfaces, and demonstrate compelling spatial/temporal characterization of their functional properties. This goal has thus far proven extremely challenging, in part because of the highly complex and overlapping vibrational signatures of proteins, amino acids, and nucleotides, as well as the dynamic and sensitive nature of cell membranes. Nonetheless, promising progress in this area has been made by a handful of groups. Neugebauer *et al.* performed tip-enhanced Raman interrogation of *Staphyllococcus Epidermidis* bacterial cell walls and meticulously deconvoluted the resulting spectra [41], and Cialla *et al.* published comparable results on the tobacco mosaic virus [42]. More recently, the Deckert group has demonstrated TERS on supported lipid membranes and human cells [43] and successful used TERS to spatially identify hemozoin crystals in a human blood cell [44].

In the 15 years since its first demonstration, TERS has made considerable progress

in regards to sensitivity and spatial resolution and has been successfully applied to the nanoscale chemical and structural characterization of a variety of material systems. However, the technique has not yet achieved widespread adoption, in part because of the limitations on sample materials and designs, which arise due to the inefficiency of Raman scattering and/or the overwhelming background contributions from sample fluorescence. As such, the development and refinement of new techniques that provide substantial improvements to signal gain would benefit the field and could enable the study of more challenging and complex systems.

1.5 Project goals

The plasmonic resonance characteristics of the tip-surface system are known to dramatically influence the enhancement of Raman scattering because of the critical role that plasmons play in mediating the excitation and scattering processes. Accordingly, incredible Raman gains have been reported in a few special circumstances, such as the single molecule imaging experiment [33], in which the resonance of the plasmonic tip-surface cavity could be tuned to match the frequency of the Raman transitions. However, the Raman enhancements in most TERS instruments are limited because of the inability to monitor or adjust the plasmonic resonance characteristics of the tip-surface system. Based on this principle, we hypothesize that by improving our understanding and control of the resonance behavior of the tip-surface system, we will be able to dynamically optimize this behavior and increase the Raman enhancement of our system. In light of this, the previously stated project goals are reiterated below but with the inclusion of a final item that reflects the broader significance and applicability of our findings to the TERS and TENOM communities:

1. Design and construct a TENOM instrument that combines an atomic force micro-

scope (AFM), a confocal Raman microscope, and a unique attenuated total reflection (ATR)-geometry illumination system for controlled excitation and detection of near-field phenomena.

2. Demonstrate the instrument's ability to locally enhance and measure surface chemistry with nanoscale spatial resolution by performing correlated topographic and Raman imaging of a nanostructured, chemically patterned surface.

3. Evaluate the instrument's ability to excite and measure a variety of near-field optical phenomena using the ATR system and compare experimental results with both theory and simulations.

4. Quantitatively compare the use of ATR and side-on illumination configurations for chemical imaging experiments with emphasis on their relative signal strengths, enhancement factors, and spatial resolution.

5. Use the TENOM instrument to investigate the optical properties of the coupled tip-surface system at short separation distances, particularly as they pertain to plasmonic behavior and spectroscopic enhancement.

6. Leverage insights resulting from tip-surface plasmon resonance studies to develop systematic improvements to the instrument design and operation that expand the ultimate capabilities of near-field optical techniques.

In the following chapters, we (i) discuss in detail how each of these goals was achieved, (ii) summarize the potential impact of our findings on the greater scientific community, and (iii) propose several future directions that would expand the functionality and sensitivity of the TENOM instrument.

References

[1] S. W. Hell and J. Wichmann, "Breaking the diffraction resolution limit by stimulated emission: stimulated-emission-depletion fluorescence microscopy," *Optics Letters*, vol. 19, no. 11, pp. 780–782, 1994.

[2] S. W. Hell and M. Kroug, "Ground-state-depletion fluorescence microscopy: A concept for breaking the diffraction resolution limit," *Applied Physics B: Lasers and Optics*, vol. 60, no. 5, pp. 495–497, 1995.

[3] J. Fölling, M. Bossi, H. Bock, R. Medda, C. A. Wurm, B. Hein, S. Jakobs, C. Eggeling, and S. W. Hell, "Fluorescence nanoscopy by ground-state depletion and single-molecule return," *Nature Methods*, vol. 5, no. 11, pp. 943–945, 2008.

[4] M. G. Gustafsson, "Nonlinear structured-illumination microscopy: Wide-field fluorescence imaging with theoretically unlimited resolution," *Proceedings of the National Academy of Sciences of the United States of America*, vol. 102, no. 37, pp. 13081–13086, 2005.

[5] E. Betzig, G. H. Patterson, R. Sougrat, O. W. Lindwasser, S. Olenych, J. S. Bonifacino, M. W. Davidson, J. Lippincott-Schwartz, and H. F. Hess, "Imaging intracellular fluorescent proteins at nanometer resolution," *Science*, vol. 313, no. 5793, pp. 1642–1645, 2006.

[6] S. T. Hess, T. P. Girirajan, and M. D. Mason, "Ultra-high resolution imaging by fluorescence photoactivation localization microscopy," *Biophysical Journal*, vol. 91, no. 11, pp. 4258–4272, 2006.

[7] M. J. Rust, M. Bates, and X. Zhuang, "Sub-diffraction-limit imaging by stochastic optical reconstruction microscopy (STORM)," *Nature Methods*, vol. 3, no. 10, pp. 793–796, 2006.

[8] U. Dürig, D. W. Pohl, and F. Rohner, "Near-field optical-scanning microscopy," *Journal of Applied Physics*, vol. 59, no. 10, pp. 3318–3327, 1986.

[9] E. Betzig, J. Trautman, *et al.*, "Breaking the diffraction barrier: Optical microscopy on a nanometric scale," *Science*, vol. 251, no. 5000, p. 1468, 1991.

[10] E. Betzig and J. K. Trautman, "Near-field optics: Microscopy, spectroscopy, and surface modification beyond the diffraction limit," *Science*, vol. 257, no. 5067, pp. 189–196, 1992.

[11] T. Kalkbrenner, M. Ramstein, J. Mlynek, and V. Sandoghdar, "A single gold particle as a probe for apertureless scanning near-field optical microscopy," *Journal of Microscopy*, vol. 202, no. 1, pp. 72–76, 2001.

[12] W. Bao, M. Melli, N. Caselli, F. Riboli, D. Wiersma, M. Staffaroni, H. Choo, D. Ogletree, S. Aloni, J. Bokor, *et al.*, "Mapping local charge recombination heterogeneity by multidimensional nanospectroscopic imaging," *Science*, vol. 338, no. 6112, pp. 1317–1321, 2012.

[13] H. Bethe, "Theory of diffraction by small holes," *Physical Review*, vol. 66, no. 7-8, p. 163, 1944.

[14] C. Bouwkamp, "On Bethe's theory of diffraction by small holes," *Rep. Prog. Phys.*, 1950.

[15] F. Keilmann and R. Hillenbrand, "Near-field microscopy by elastic light scattering from a tip," *Phil. Trans. R. Soc. Lond. A*, pp. 787–806, 2004.

[16] L. Novotny and N. Van Hulst, "Antennas for light," *Nature Photonics*, vol. 5, no. 2, pp. 83–90, 2011.

[17] J. M. Gerton, L. A. Wade, G. A. Lessard, Z. Ma, and S. R. Quake, "Tip-enhanced fluorescence microscopy at 10 nanometer resolution," *Physical Review Letters*, vol. 93, no. 18, p. 180801, 2004.

[18] R. Rendell and D. Scalapino, "Surface plasmons confined by microstructures on tunnel junctions," *Physical Review B*, vol. 24, no. 6, p. 3276, 1981.

[19] R. M. Stöckle, Y. D. Suh, V. Deckert, and R. Zenobi, "Nanoscale chemical analysis by tip-enhanced Raman spectroscopy," *Chemical Physics Letters*, vol. 318, no. 1, pp. 131–136, 2000.

[20] P. Hildebrandt and M. Stockburger, "Surface-enhanced resonance Raman spectroscopy of Rhodamine 6G adsorbed on colloidal silver," *The Journal of Physical Chemistry*, vol. 88, no. 24, pp. 5935–5944, 1984.

[21] M. Moskovits and J. Suh, "Surface selection rules for surface-enhanced Raman spectroscopy: Calculations and application to the surface-enhanced Raman spectrum of phthalazine on silver," *Journal of Physical Chemistry*, vol. 88, no. 23, pp. 5526–5530, 1984.

[22] J. T. Krug, E. J. Sánchez, and X. S. Xie, "Design of near-field optical probes with optimal field enhancement by finite difference time domain electromagnetic simulation," *The Journal of Chemical Physics*, vol. 116, no. 24, pp. 10895–10901, 2002.

[23] M. Micic, N. Klymyshyn, Y. D. Suh, and H. P. Lu, "Finite-element method simulation of the field distribution for AFM tip-enhanced surface-enhanced Raman scanning microscopy," *The Journal of Physical Chemistry B*, vol. 107, no. 7, pp. 1574–1584, 2003.

[24] W. Zhang, X. Cui, B.-S. Yeo, T. Schmid, C. Hafner, and R. Zenobi, "Nanoscale roughness on metal surfaces can increase tip-enhanced Raman scattering by an order of magnitude," *Nano Letters*, vol. 7, no. 5, pp. 1401–1405, 2007.

[25] J. Stadler, B. Oswald, T. Schmid, and R. Zenobi, "Characterizing unusual metal substrates for gap-mode tip-enhanced Raman spectroscopy," *Journal of Raman Spectroscopy*, vol. 44, no. 2, pp. 227–233, 2013.

[26] C. Blum, L. Opilik, J. M. Atkin, K. Braun, S. B. Kämmer, V. Kravtsov, N. Kumar, S. Lemeshko, J.-F. Li, K. Luszcz, *et al.*, "Tip-enhanced Raman spectroscopy–an interlaboratory reproducibility and comparison study," *Journal of Raman Spectroscopy*, vol. 45, no. 1, pp. 22–31, 2014.

[27] B. Pettinger, K. F. Domke, D. Zhang, R. Schuster, and G. Ertl, "Direct monitoring of plasmon resonances in a tip-surface gap of varying width," *Physical Review B*, vol. 76, no. 11, p. 113409, 2007.

[28] B. Pettinger, K. F. Domke, D. Zhang, G. Picardi, and R. Schuster, "Tip-enhanced Raman scattering: Influence of the tip-surface geometry on optical resonance and enhancement," *Surface Science*, vol. 603, no. 10, pp. 1335–1341, 2009.

[29] D. Mehtani, N. Lee, R. Hartschuh, A. Kisliuk, M. Foster, A. Sokolov, and J. Maguire, "Nano-Raman spectroscopy with side-illumination optics," *Journal of Raman Spectroscopy*, vol. 36, no. 11, pp. 1068–1075, 2005.

[30] J. Steidtner and B. Pettinger, "High-resolution microscope for tip-enhanced optical processes in ultrahigh vacuum," *Review of Scientific Instruments*, vol. 78, no. 10, p. 103104, 2007.

[31] J. Stadler, T. Schmid, and R. Zenobi, "Nanoscale chemical imaging using top-illumination tip-enhanced Raman spectroscopy," *Nano Letters*, vol. 10, no. 11, pp. 4514–4520, 2010.

[32] B. Ren, G. Picardi, and B. Pettinger, "Preparation of gold tips suitable for tip-enhanced Raman spectroscopy and light emission by electrochemical etching," *Review of Scientific Instruments*, vol. 75, no. 4, pp. 837–841, 2004.

[33] R. Zhang, Y. Zhang, Z. Dong, S. Jiang, C. Zhang, L. Chen, L. Zhang, Y. Liao, J. Aizpurua, Y. e. Luo, *et al.*, "Chemical mapping of a single molecule by plasmon-enhanced Raman scattering," *Nature*, vol. 498, no. 7452, pp. 82–86, 2013.

[34] A. C. Ferrari, J. Meyer, V. Scardaci, C. Casiraghi, M. Lazzeri, F. Mauri, S. Piscanec, D. Jiang, K. Novoselov, S. Roth, *et al.*, "Raman spectrum of graphene and graphene layers," *Physical Review Letters*, vol. 97, no. 18, p. 187401, 2006.

[35] T. Yano, P. Verma, Y. Saito, T. Ichimura, and S. Kawata, "Pressure-assisted tip-enhanced Raman imaging at a resolution of a few nanometres," *Nature Photonics*, vol. 3, no. 8, pp. 473–477, 2009.

[36] R. Beams, L. G. Cançado, A. Jorio, A. N. Vamivakas, and L. Novotny, "Tip-enhanced Raman mapping of local strain in graphene," *Nanotechnology*, vol. 26, no. 17, p. 175702, 2015.

[37] E. M. van Schrojenstein Lantman, T. Deckert-Gaudig, A. J. Mank, V. Deckert, and B. M. Weckhuysen, "Catalytic processes monitored at the nanoscale with tip-enhanced Raman spectroscopy," *Nature Nanotechnology*, vol. 7, no. 9, pp. 583–586, 2012.

[38] M. Sun, Z. Zhang, H. Zheng, and H. Xu, "In-situ plasmon-driven chemical reactions revealed by high vacuum tip-enhanced Raman spectroscopy," *Scientific Reports*, vol. 2, p. 647, 2012.

[39] R. Treffer, X. Lin, E. Bailo, T. Deckert-Gaudig, and V. Deckert, "Distinction of nucleobases–a tip-enhanced Raman approach," *Beilstein Journal of Nanotechnology*, vol. 2, no. 1, pp. 628–637, 2011.

[40] E. Bailo and V. Deckert, "Tip-enhanced Raman spectroscopy of single RNA strands: Towards a novel direct-sequencing method," *Angewandte Chemie International Edition*, vol. 47, no. 9, pp. 1658–1661, 2008.

[41] U. Neugebauer, P. Roesch, M. Schmitt, J. Popp, C. Julien, A. Rasmussen, C. Budich, and V. Deckert, "On the way to nanometer-sized information of the bacterial surface by tip-enhanced Raman spectroscopy," *ChemPhysChem*, vol. 7, no. 7, pp. 1428–1430, 2006.

[42] D. Cialla, T. Deckert-Gaudig, C. Budich, M. Laue, R. Möller, D. Naumann, V. Deckert, and J. Popp, "Raman to the limit: Tip-enhanced Raman spectroscopic investigations of a single tobacco mosaic virus," *Journal of Raman Spectroscopy*, vol. 40, no. 3, pp. 240–243, 2009.

[43] R. Böhme, M. Richter, D. Cialla, P. Rösch, V. Deckert, and J. Popp, "Towards a specific characterization of components on a cell surface–combined TERS-investigations of lipids and human cells," *Journal of Raman Spectroscopy*, vol. 40, no. 10, pp. 1452–1457, 2009.

[44] B. R. Wood, E. Bailo, M. A. Khiavi, L. Tilley, S. Deed, T. Deckert-Gaudig, D. McNaughton, and V. Deckert, "Tip-enhanced Raman scattering (TERS) from hemozoin crystals within a sectioned erythrocyte," *Nano Letters*, vol. 11, no. 5, pp. 1868–1873, 2011.

Chapter 2

Design and validation of a tip-enhanced near-field optical microscopy (TENOM) instrument

2.1 Design overview

As discussed in Chapter 1, a TENOM instrument consists of three component systems: (i) a scanning probe microscope for control of the TENOM tip position, (ii) an optical illumination system for tip excitation, and (iii) a collection and detection system for measurement of tip-enhanced optical signals. Major design decisions, such as the choice of SPM technique and illumination/collection scheme, depend critically on the intended applications of the instrument. In the case of the present microscope, such decisions were made to maximize the versatility of the instrument, as well as to facilitate the inclusion of an additional component, a unique attenuated total reflectance (ATR)-geometry excitation/detection system that will be discussed in detail in Chapter 3.

The overall TENOM instrument designed in this work is shown schematically in Figure 2.1. At its center is a highly modified commercial AFM around which a variety of cameras and custom optical systems are positioned. A compact confocal Raman microscope, equipped with a laser, monochromator, and CCD, is used for both side-on tip excitation and signal collection. The ATR system is built on the optical bench in front of the AFM and couples to the rest of the microscope by way of a custom stage that houses most of the system's critical optics. The present chapter focuses primarily on the design and validation of both the AFM and Raman microscope components of the system, and it concludes with a demonstration of their combined operation to perform super-resolution chemical interrogation of a nanopatterned surface. The following discussion will emphasize the instrument's performance as it relates to the following technical goals:

- Stable AFM operation at small force set point ($\sim$nN)
- Diffraction-limited tip illumination
- Efficient confocal scattered light collection
- Strong plasmonic enhancement from TENOM tips
- Ability to detect chemical variations at sub-diffraction-limited spatial resolutions (i.e., $<$200 nm)

2.2 Atomic force microscope

Perhaps the most critical decision in building a TENOM instrument is the selection of an appropriate SPM technique with which to measure and control tip-surface interactions. While scanning tunneling microscopy (STM) provides several unique benefits, such as

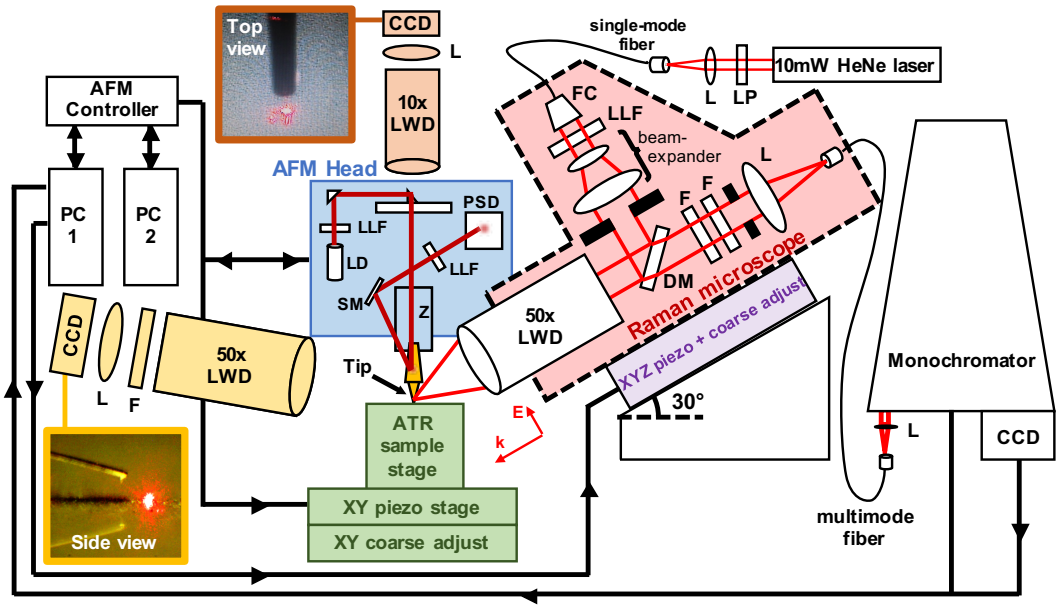

Figure 2.1: **Schematic of the TENOM instrument.** The instrument consists of three main components: (i) an atomic force microscope, (ii) a confocal Raman microscope with fiber-coupled monochromator and CCD, and (iii) an ATR-geometry near-field excitation/detection system (detail shown in Chapter 3) that is coupled to the instrument by way of a custom sample stage. Top- and side-view cameras were used extensively for system observation and alignment. Note: CCD = charge-coupled device, DM = dichroic mirror, F = filter, FC = fiber coupler, L = lens, LD = laser diode, LLF = laser line filter, LP = linear polarizer, LWD = long working distance objective, PSD = position-sensitive detector, SM = steering mirror, Z = z-piezo

exceptional spatial resolution and tip-surface distance control, the technique is inherently limited to use on conducting materials. This restriction precludes the study of a wide range of systems, such as biological surfaces, and makes AFM the ideal SPM technique for a versatile TENOM instrument. Before describing any specifics of the AFM design process, it is important for the coming discussion to briefly explain a few of the relevant principles behind contact mode AFM operation. In contact mode AFM, the probe tip is attached to the end of a flexible cantilever; the deflection of this cantilever is monitored by way of the "beam-bounce" optical technique and is used to measure tip-surface forces. Light from a laser diode is reflected off the back of the cantilever, and the reflected beam is directed onto a four-quadrant, position-sensitive detector (PSD). The PSD measures

the beam position relative to the center of the detector and is used to observe vertical and lateral displacements of the reflected beam, which are related to deflection and twisting of the cantilever, respectively. The vertical displacement signal, hereafter referred to as the "top minus bottom", or T–B, signal (i.e., it is determined from the signal difference between the top and bottom halves of the PSD), is of particular relevance because it is roughly proportional to the tip-surface force. Using this signal as feedback, the computer-controlled electronics can regulate the vertical position of the tip (via a piezoelectric actuator) to keep the tip-surface force at or near a predetermined set-point value while the sample is laterally scanned below the tip. This arrangement enables controlled, constant-force measurement of surface height as a function of stage position and can yield topographic line profiles and images. Given this principle of operation, the stability of the beam-bounce system is critically important in contact mode AFM, as it is the singular feedback mechanism for maintaining constant tip-surface force. In addition to a robust beam-bounce system, there are several other key AFM design criteria that are necessary for successful TENOM operation:

1. **Stable AFM regulation and position control:** The ability to precisely control and maintain both the tip-surface force and the tip position over the course of several minutes is critical for nanoscale optical measurements; this was the justification for starting with a commercial system.

2. **Robust imaging over a range of lengthscales:** Regions of interest are often found via large area topography scans, and the interrogation area is narrowed for high resolution optical measurements.

3. **Open optical access:** To most efficiently collect the desired tip-enhanced signals, the Raman microscope objective must be positioned at its optimal working distance from the tip apex and have an unobstructed "view" of the tip-surface junction.

Furthermore, optical access from the top and side are important for both tip/surface observation and system alignment.

4. **Optically isolated beam-bounce system:** It is important that the Raman laser not interfere with the beam-bounce optical system and that the beam-bounce laser does not interfere with Raman measurements.

In the following sections, we discuss the extensive modification of the commercial AFM to fit these requirements, as well as the validation of the redesigned system to test its capabilities.

2.2.1 AFM design

Considering the aforementioned criteria, we started with a Park XE-100 commercial AFM whose original design had two primary drawbacks. First, the beam-bounce system made use of a 650 nm laser diode, whose emission was broad and would overlap with and overwhelm any Raman measurements done with 633 nm HeNe excitation light (the intended design wavelength of the TENOM system). Second, and more significantly, the physical design of the AFM's beam-bounce housing severely restricted optical access from all sides and prevented even an ultra-long working distance microscope objective from getting sufficiently close to the AFM tip (see Figure 2.2(a) and (b)). Furthermore, the compact and efficient design of the beam-bounce mechanism precluded the simplest solution of re-machining the original parts to accommodate the Raman microscope objective (Figure 2.2(c)). Thus, the beam-bounce mechanism and housing, hereafter referred to collectively as the AFM head unit, had to be redesigned and machined from scratch to provide the necessary access for the optical components of the TENOM instrument.

To maximize the compatibility of the custom-designed head unit with the rest of the commercial AFM, many aspects of the original design, including some original compo-

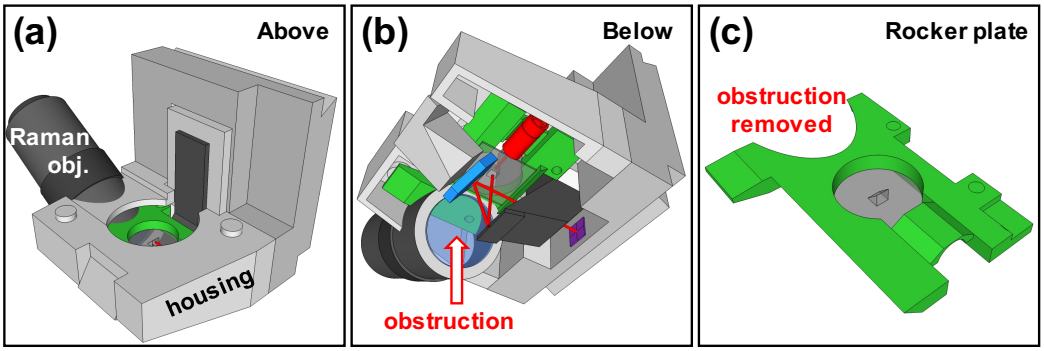

Figure 2.2: **Original commercial AFM design with limited optical access.** (a) Top- and (b) bottom-view renderings of the Park XE-100 commercial AFM head unit and a 0.42 NA objective positioned near the cantilever. The overlap between the two components illustrates the obstructed optical access of the original design. (c) Rendering of the AFM head's rocker plate (a critical component of the beam-bounce mechanism) with the objective-obstructing portion removed. We concluded that removing this section would compromise the mechanical integrity of the beam-bounce system.

nents, were preserved by reverse-engineering the beam-bounce pathway and mechanism. A computer-aided design program (SketchUp) was used extensively in the development of the replacement AFM head and was invaluable in ensuring the mutual compatibility of custom and original AFM parts. Furthermore, the physically precise 3D SketchUp model, which was extended to include all critical components of the commercial AFM, facilitated the design and layout of the TENOM instrument's other components (i.e., the Raman microscope and the ATR system) and was critically important in verifying the alignment of these independent systems with the AFM tip.

The final design of the AFM head, shown in Figure 2.3, retains several of the desirable features of the original, while resolving the issue of spectral overlap and providing open access from three different directions. The beam-bounce pathway, shown schematically in Figure 2.3(b), is similar to the original design in that the laser diode sits inside a "rocker plate" that is mounted to an outer housing via springs. In place of the original 650 nm diode, we instead used an 850 nm near infrared diode; this wavelength is sufficiently

separated in energy from the 633nm Raman excitation light that it does not interfere with Raman measurements from 0–3000 cm^{-1}. A small right-angle prism mounted on a glass slide is attached to the rocker plate and used to steer the laser beam downward toward the cantilever. This clever design enables unobstructed top-side observation of the cantilever and sample through the glass slide by way of a long working distance (LWD) objective and camera. The tip-tilt orientation of the rocker plate controls the path of the beam-bounce laser and can be adjusted using two thumb screws to align the beam with the end of the AFM cantilever. The laser light reflected off the cantilever is directed toward the center of the PSD using a steering mirror; along the way, the light passes through a 850 nm bandpass filter, which is intended to prevent any 633 nm Raman excitation light from reaching the PSD and interfering with the AFM's regulation. Of course, the most important aspect of the custom AFM head is the open optical access afforded by the unique shape of the rocker plate and outer housing; this allows the Raman microscope objective to be positioned with the AFM tip at its optimal focal point. The housing design opposite the Raman microscope also provides access for a side-on observation microscope that is vital for alignment of the tip/cantilever with the beam-bounce laser, the Raman microscope, and the ATR system. The custom housing and rocker plate were machined from aluminum and black anodized to minimize reflections and scattering of stray light during Raman measurements.

The AFM can be operated in either an internal or external control scheme as detailed in the signal routing schematics in Figure 2.4. Under internal control, all piezo movements and instrument parameters are passed to the AFM by its associated commercial software, which runs independently on a dedicated PC (PC2). This software is used extensively for different aspects of instrument operation and control, such as beam-bounce alignment, tip approach, and adjustment of stage scanning parameters (scan size/speed/location) and tip regulation parameters (set-point, gain). It also produces high-quality calibrated

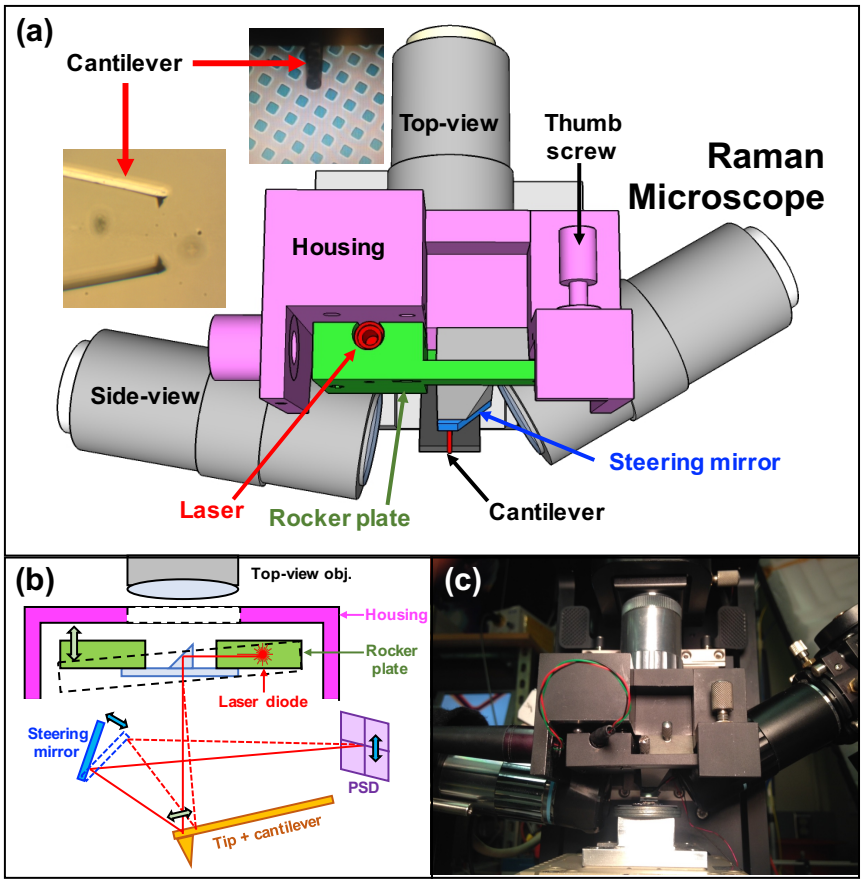

Figure 2.3: **Modified AFM head design.** (a) Front-view rendering of the custom AFM head with the Raman microscope and top- and side-view objectives positioned around the cantilever. Several important elements of the beam-bounce mechanism are also labeled. (b) Schematic of the beam-bounce optical path and steering mechanisms (see text for detailed discussion). Green and blue arrows represent how the beam path changes due to adjustments of the rocker plate and steering mirror, respectively. (c) Photograph of the final AFM head incorporated into the TENOM instrument.

images thanks to its closed-loop piezo correction. While operating in this mode, several important internal signals (e.g., T–B, z-piezo drive voltage) can be passively monitored by way of the AFM's Signal Access Module (SAM). This is particularly useful in the case of the T–B signal, which can be scrutinized with an oscilloscope to qualitatively assess tip-surface forces during tip approach and ensure adequate tip regulation during scanning.

While internal control is useful for simple AFM imaging of surfaces, external control

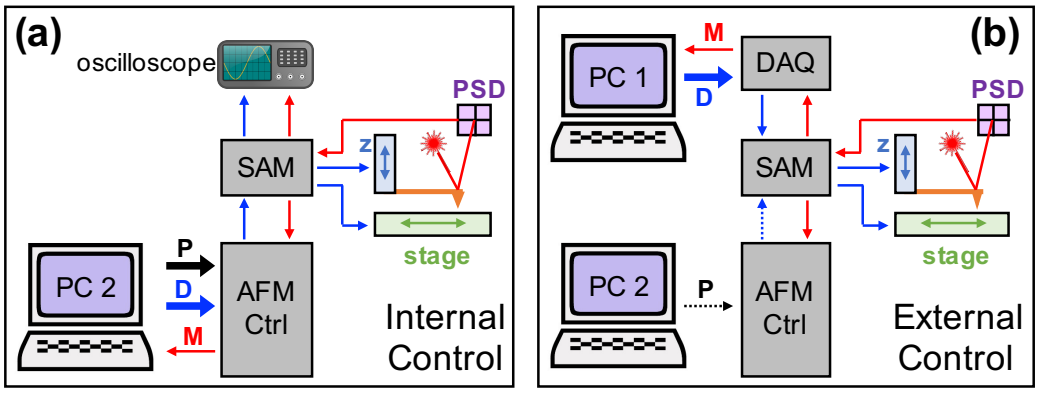

Figure 2.4: **Signal routing schematics for AFM operation modes.** (a) Schematic of the signal routing during internal control of the AFM. PC2 is used to pass feedback parameters (P) and piezo driving signals (D, blue lines) to the AFM controller and also records monitoring signals (M, red lines) during measurements. The signal access module (SAM) enables passive observation of driving and monitoring signals with an oscilloscope. (b) Schematic of the signal routing during external control of the AFM. PC1 is used to pass driving signals to the AFM by way of a data acquisition board (DAQ) and the SAM. In some external control experiments (e.g. topographic imaging), PC2 can simultaneously pass feedback parameters to the AFM controller for active z-piezo regulation.

enables greater versatility and customization of TENOM experiments, as well as being critical for synchronization of AFM movements during near-field optical measurements. Most applications requiring external control consist of timed movements of the AFM piezo elements and concurrent collection of AFM output signals and/or optical signals from the instrument's other components. These synchronized actions are orchestrated by custom LabVIEW programs on a separate PC (PC1) that make use of a digital-to-analog converter (DAQ) board to write and read AFM signals by way of the SAM. In this way, LabVIEW can be used to take over the stage and/or tip scanning operations, as well as perform imaging, approach curves, and a variety of more complex experiments involving the AFM.

2.2.2 AFM validation

Because of the substantial modifications made to the original AFM design, it was important to carefully assess the instrument's performance afterward to confirm the functionality of the custom head. Specifically, we sought to verify the following necessary criteria:

1. **Tip stability with a static sample:** TENOM experiments often require that the tip be stationary relative to the sample for long periods of time (i.e., seconds to minutes)

2. **Large- and small-area scan capabilities:** Many TENOM experiments require large area imaging followed by high resolution, short distance studies.

3. **Accurate piezo calibration:** Piezo calibration is critical for quantitative spatial evaluation of TENOM results.

4. **Low-force (∼nN) imaging:** Because TENOM tips are coated in Au, they are very delicate, as are many samples; operating at a low tip-surface force is important for prolonging tip lifetimes and preserving their plasmonic properties.

5. **External piezo control and imaging:** TENOM experiments are performed exclusively via external control, and thus, proper external operation must be confirmed.

Most of these properties and capabilities were tested by topographically imaging several different samples that spanned a range of feature sizes in X,Y and Z. The grid pattern imaged in Figure 2.5(a) is an AFM calibration standard with a 3 μm in-plane pitch and step heights of 1 μm; imaging this sample is particularly challenging because

of the height and sharpness of the features. The quality of the image clearly demonstrates the instrument's ability to maintain proper regulation, even during large area scans and high tip-scanning speeds. The line pattern shown in Figure 2.5(b) is another calibration standard and is used for higher resolution calibration, as its feature sizes are roughly an order of magnitude smaller than the grid pattern. Both of these images were quantitatively compared against the known features dimensions of the samples, and they confirmed the calibration of the AFM x-, y-, and z-piezos over a range of lengthscales. Figure 2.5(c). is an image of an isolated carbon nanotube on an Au substrate and is the most important display of the instrument's sensitivity. Because the nanotube was not bound to the Au surface by any chemical means, it was extremely susceptible to mechanical disturbances (i.e., being pushed around by the tip); thus, imaging this nanowire required stable AFM operation at a very low set-point force ($<\sim$1 nN). Not only does the latter image demonstrate the AFM's ability to sensitively measure delicate samples, but it also exhibits excellent vertical resolution in both the height of the nanotube ($<$10 nm) and the roughness of the Au surface (RMS $\sim$2 nm).

Lastly, to test the performance of the external control scheme, the custom LabVIEW software was used to pilot the AFM and collect a topographic image of the line pattern shown in Figure 2.5(b) The resulting image, shown in Figure 2.5(d), confirmed the viability of external control and allowed us to estimate the piezos' characteristic voltage-position relations. However, the image exhibits considerable piezo hysteresis artifacts in the form of feature broadening near the edges, despite efforts to mitigate these effects through data treatment and revised scanning protocols. This hysteresis makes internal AFM control preferable for imaging because it is precisely corrected for by the commercial software. However, these results demonstrate that external AFM control is still sufficiently accurate for TENOM experiments.

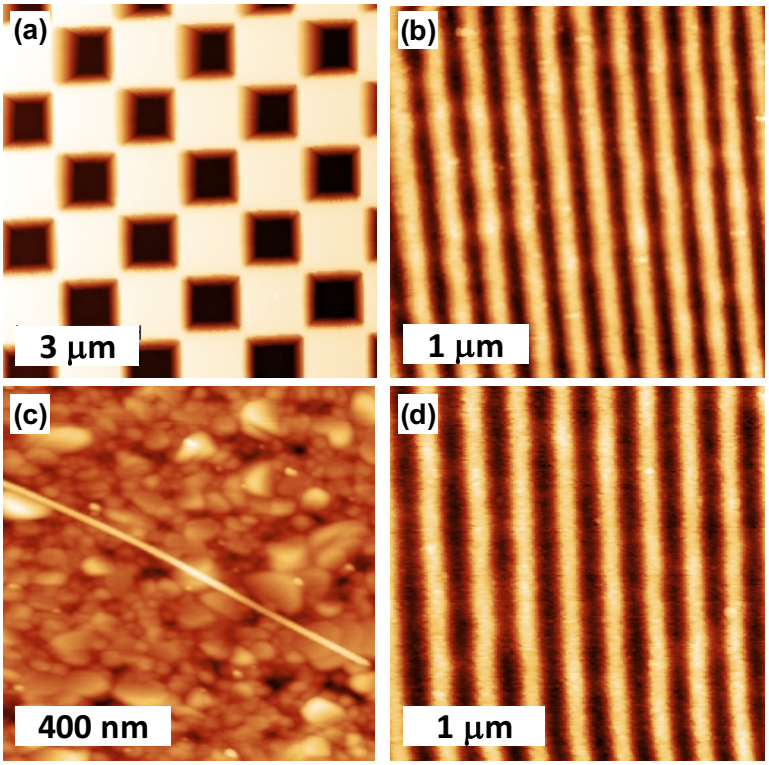

Figure 2.5: **AFM imaging of test structures.** (a) Topographic image of a 2D grid pattern (3 μm pitch in x and y; feature height = 600 nm; internal AFM control). (b) and (d) Topographic images of a 1D grating pattern (300 nm pitch; feature height = 50 nm) measured via internal and external AFM control, respectively. (c) Topographic image of a multi-walled carbon nanotube on a Au substrate (feature height = 8 nm, internal AFM control).

2.3 Raman microscope

The key optical component of the TENOM instrument is a custom-built confocal Raman microscope that is used to focus laser light onto the tip, collect the light that is emitted, and spectrally analyze the collected light to detect chemically specific optical events. The critical design goals for this system were as follows:

1. **Diffraction-limited excitation and collection:** Ensuring that the focused laser spot and the collection volume are as small as possible will maximize the light intensity at the tip and minimize the physical size of the background region, respective.

2. **Efficient confocal collection:** Confocal collection improves the signal-to-noise ratio (S/N) by narrowing the microscope's depth of field to preferentially reject background light.

3. **High-efficiency detection:** Raman scattering is inherently weak; thus, a high-sensitivity, low noise detector is important.

4. **Piezo-controlled positioning:** TENOM experiments require precise alignment of the Raman microscope and the tip to ensure optimal signal collection.

In the following sections, the design and operation of the custom Raman microscope is described, and the results of three validation studies are discussed to assess the performance of the microscope relative to the criteria above.

2.3.1 Microscope design

A schematic of the microscope's optical path is shown in Figure 2.6. The microscope is mounted at 60° from the sample normal on a 3-axis piezo flexure stage (NanoMax, ThorLabs) that allows precise control of the focal point relative to the tip and sample. During top-side illumination experiments, 633 nm laser light from a 10 mW HeNe laser is fiber-coupled to the microscope by way of a panda-style polarization-maintaining, single-mode optical fiber. The linearly-polarized light exiting the fiber is collimated, filtered and expanded to a ∼12 mm parallel beam. An iris reduces the beam diameter to that of the objective rear aperture (∼6 mm) before it is directed towards the objective using a dichroic mirror (RazorEdge, Semrock). The optics are oriented such that the polarization plane of the laser light is parallel to the tip axis to maximize tip-laser coupling. A 0.42 NA, infinity-corrected, 50X LWD objective is used to focus the laser light on the tip.

The same objective is used to collect the light scattered by the tip during TENOM experiments. The collected light passes through the dichroic mirror and a long-pass 633

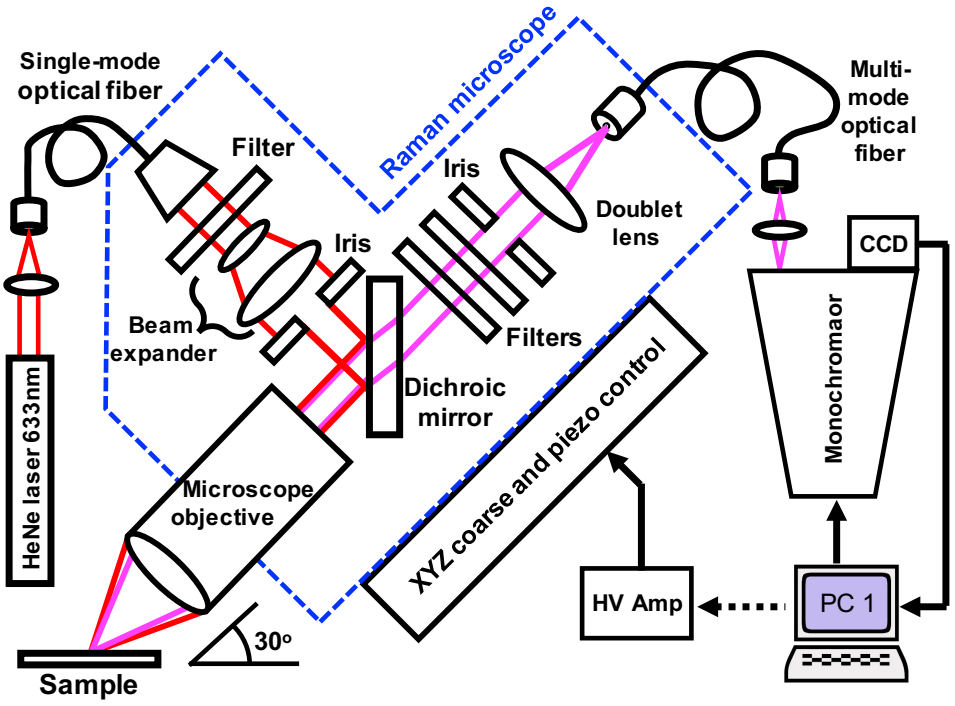

Figure 2.6: **Schematic of Raman microscope design.** Schematic of the optical path of the Raman microscope and the signal routing for PC control of the monochromator and CCD. The PC can also be used to control the Raman microscope's piezo stage for automated scanning protocols (e.g., 2D spectroscopic imaging).

nm Raman filter (RazorEdge ultrasteep, Semrock), attenuating the elastically scattered (Rayleigh) signal by $>10^8$ and allowing simultaneous measurement of Rayleigh and Raman scattering, with Raman detection as low as $\sim$70 cm^{-1}. An 842 nm short-pass filter (BrightLine, Semrock) is used to reject any spurious light from the AFM beam-bounce laser. An achromatic doublet (f = 60 mm) focuses the collected light into the core of a multi-mode optical fiber (interchangeable with avalable core diameters of 50, 100, and 200 μm) that acts as a confocal pinhole (spatial filter) to narrow the microscope's depth of field by rejecting out-of-focus light (see Figure 2.8(a)). The spatial extent of this light rejection is a function of the fiber core diameter, as will be discussed in the next section. Light exiting the other end of the collection fiber is f-matched to a monochromator (550 mm focal length, Jobin-Yvon iHR550), where it is wavelength dispersed by one of three

possible gratings, depending on the signal intensity and desired spectral resolution. The dispersed light is then refocused onto a liquid-nitrogen-cooled CCD detector (Symphony, Jobin-Yvon), which provides high-sensitivity, low-noise detection due to its exceptional suppression of thermal noise.

Both the monochromator and the CCD are controlled by custom LabVIEW programs, which are used to adjust important parameters, such as the monochromator's grating position and entrance slit width and the CCD's acquisition time. LabVIEW is also used to trigger spectral acquisition, often times in synchrony with other instrument operations, and to read out and record the resulting spectra. The position of the Raman microscope relative to the sample and AFM is controlled via the 3-axis stage on which it is mounted; this enables coarse movement, by way of micrometer drives, as well as fine position control, by way of piezoelectric actuators. These piezos are driven by an adjustable high voltage amplifier, which can either be controlled manually or by LabVIEW, similarly to the external AFM control discussed previously. This enables automated stage scanning routines with synchronized spectral collection and facilitated a variety of experiments, including the validation studies detailed in the next section.

2.3.2 Microscope validation

The performance of the Raman microscope was carefully evaluated using a number of experiments that not only provided quantitative metrics for the system's spatial resolution, but also helped in the optimization of its alignment. The in-plane spatial resolution of the optical system was determined by measuring the point-spread function (PSF), which describes how a microscope images a point source (i.e., an infinitesimal light emitter). The PSF was measured by "imaging" the fluorescence from an isolated fluorescent nanoparticle with a diameter (170 nm) much smaller than the diffraction limit. In this

context, "imaging" is performed by raster scanning the microscope in the plane of the sample surface and pausing to collect an optical spectrum at each (x,y) position. A 2D image is subsequently constructed by mapping the intensity of a desired spectral feature, in this case the fluorescence from the nanoparticle, at each (x,y) pixel. Ideally, the emission from the point source should be constant throughout the scan in order to isolate the PSF of the collection pathway. Unfortunately, this is not possible with the present system since the nanoparticle is being excited by the focused laser spot, which has its own spatial distribution. Thus, the resulting PSF, shown in Figure 2.7, is a convolution of the excitation and collection pathways. Nevertheless, it faithfully represents the spatial resolution of the combined optical system. Line-cuts through the center of the 2D PSF pattern exhibit Gaussian profiles, as expected, a full width at half maximum (FWHM) of 3.1 μm and 1.3 μm in the long (x) and short (y) axes, respectively. For comparison, theoretical predictions for the PSF of a diffraction-limited system yield FWHM values of 2.31 μm and 0.63 μm in the x and y axes, respectively [1]. The observed deviations from the theoretical diffraction limit are most likely due to convolution of the excitation and illumination pathways caused by their misalignment. Unfortunately, this is difficult to correct since neither pathway can be measured independently with the present microscope arrangement.

The efficiency of the microscope's confocal light collection and rejection was quantified by measuring the depth of field (DOF) for three different "pinhole" sizes (i.e., collection fibers of varying core diameter). The DOF, which is effectively a measure of the PSF along the microscope's optical axis, was determined experimentally by measuring Raman scattering from a thin film of InSb as the microscope was moved in and out of focus (see Figure 2.8(a)). When the focal point of the objective was aligned with the InSb surface, Raman collection was optimal; moving the microscope either up or down from this point reduced the Raman collection efficiency. Figure 2.8(b) shows the results of the

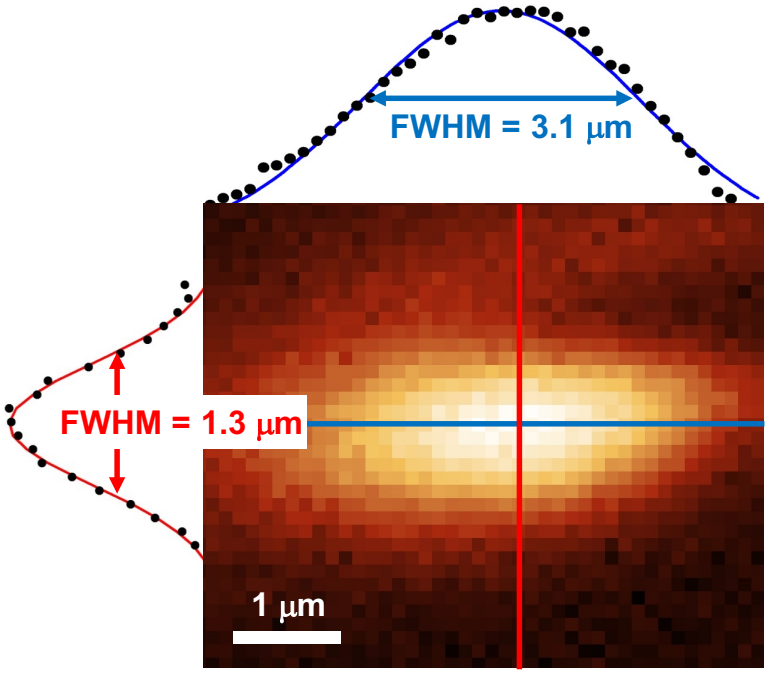

Figure 2.7: **Point spread function of the Raman microscope.** 2D spectral image of an isolated fluorescent nanoparticle (170 nm diameter) on a Si surface taken by raster scanning the Raman microscope relative to the sample surface and measuring a fluorescence spectrum at each pixel. used to quantify the spatial resolution of the optical system. Line profiles through the long (x) and short (y) axes of the image are shown (points above and to the left) with corresponding Gaussian fits (curves), which display FWHMs of 3.1 μm and 1.3 μm, respectively.

DOF experiments for all three collection fibers, along with Gaussian fits whose FWHMs allow us to quantify the DOF. The DOF measurements also provided an absolute and quantitative comparison of the collection efficiency and background rejection of different fibers. Figure 2.8(c) compares the individual spectra (from the same DOF measurements as in (b)) taken at optimal focus for both the 50 μm and 100 μm fibers. The spectra show that the 50 μm fiber collects nearly as much Raman light as 100 μm fiber, but the background intensity (the Rayleigh scattering at 0 cm^{-1}) is reduced by 65%. This demonstrates that not only is the confocal collection working as expected to reduce optical background intensity, but also, the system is clearly in excellent alignment since reducing the fiber size did not result in a considerable loss of signal.

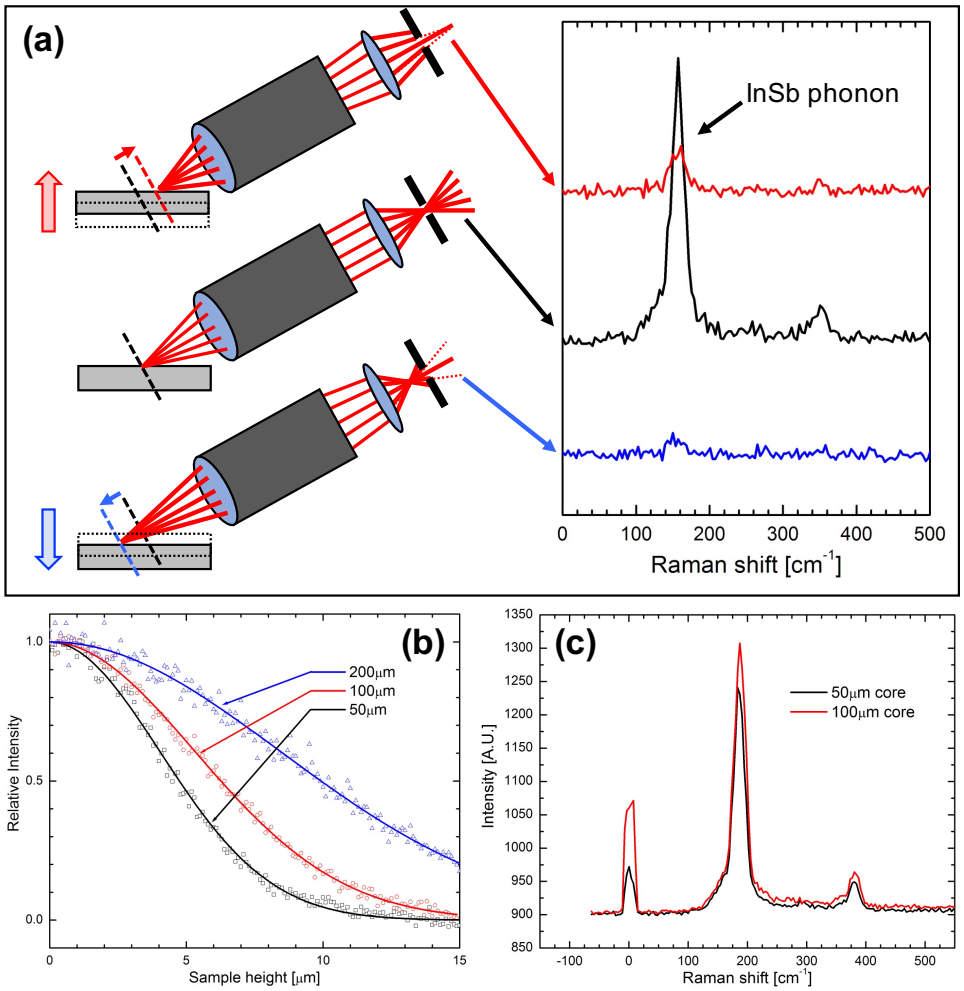

Figure 2.8: **Depth of field of the Raman microscope.** (a) Schematic depiction of the depth-of-field experiment showing how a small aperture (in this case, the core of the collection fiber) can reject out-of-focus light. Spectra on the right in (a) demonstrate the signal of interest: a Raman peak associated with phonon excitation in the InSb sample. (b) Results of the depth-of-field measurements showing the observed intensity of the InSb phonon as a function of sample height (relative to the position of optimal focus) for three different fiber core sizes (50, 100 and 200 μm). Experimental data (points) were fit to Gaussian profiles (curves). (c) Direct comparison of individual spectra from (b) taken at optimal focus ("Sample height" = 0) for fiber core sizes of 50 and 100 μm. Reduction in Rayleigh scattering (0 cm^{-1}) for 50 μm fiber demonstrates effective background light rejection, and small difference in Raman signal (190 cm^{-1}) suggests excellent alignment of collection system.

The final validation study, designed to demonstrate the microscope's sensitivity and practical applicability, involved the imaging of a chemically heterogeneous surface. The

goals of the experiment were twofold:

1. Demonstrate that the system has sufficient sensitivity to detect Raman scattering with reasonably short collection times (e.g., $<\sim$2 sec/pixel), to enable high resolution line scans and 2D optical imaging within a practical timescale (e.g., 30x30 pixel image in <1 hr).

2. Perform full 2D spectral imaging of a heterogeneous surface, mapping different spectral features to form chemical images.

The sample used for this experiment consisted of a glass coverslip with palladium oxide (PdO) squares on the surface. Samples were prepared by using electron beam evaporation to deposit 100 nm of Pd through the holes in a 300 mesh TEM grid and subsequently annealing the Pd in air at 300°C for $\sim$12 hr. PdO was chosen because it supports an optical phonon (a quantized crystal lattice vibration) that can be detected by Raman spectroscopy, however, it is a non-resonant mode and is therefore weak and not trivial to detect. Furthermore, the glass substrate also displays weak optical emission in the form of a broad fluorescent band caused by impurities such as sodium. Thus, the PdO squares and the substrate both exhibit weak spectral signatures by which they can be chemically distinguished. By "imaging" this sample (i.e., raster scanning the microscope in discrete steps and collecting an optical spectrum at each position), two different 2D images can be constructed from the resulting spectral data: one image that spatially plots the intensity of the PdO Raman peak, and one that plots the intensity of the glass fluorescence.

The results of this experiment are shown in Figure 2.9, with panel (a) showing a spatial map of the PdO Raman intensity and panel (c) plotting the glass fluorescence; between them, in panel (b), two individual spectra from the dataset are plotted for comparison. The top spectrum, taken when the microscope was focused on the glass substrate, clearly

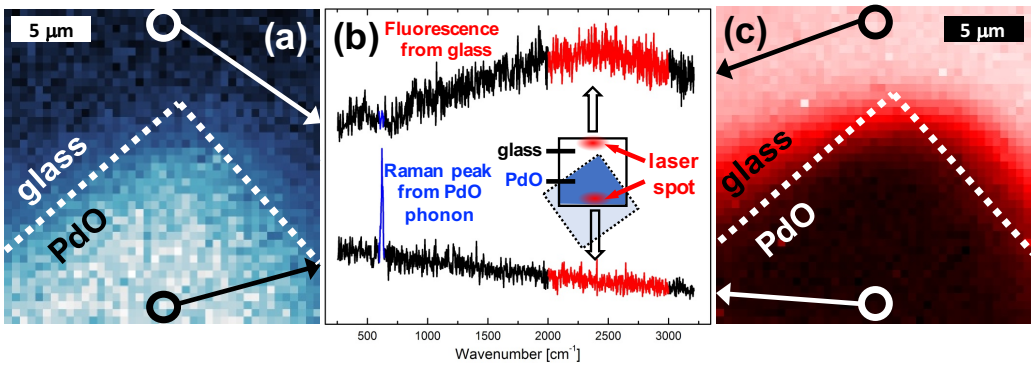

Figure 2.9: **2D Raman/fluorescence mapping of PdO squares on glass.** (a) and (c) Far-field spectral (chemical) images of the corner of a PdO square on a glass coverslip measured using the procedure described in the text. (a) 2D intensity map of the PdO Raman peak (∼550 cm^{-1}). (c) 2D intensity map of the broad fluorescence band generated by impurities in the glass. (b) Two representative spectra from the same dataset as (a) and (c) which demonstrate the shape, intensity, and wavenumber position of two spectral features of interest.

shows the broad fluorescent band expected and exhibits no Raman peaks. Conversely, the bottom spectrum, taken near the center of the PdO square, shows no fluorescence and a clear Raman peak at ∼600 cm^{-1} that is associated with the PdO phonon. As anticipated, the 2D intensity plots of these spectral features are complementary, and the "sharpness" of transition from PdO to glass is consistent with the PSF of microscope, though it may also be convolved with a thinning of the PdO layer near the feature edges. The clarity and S/N of these weak spectral features nicely demonstrates the sensitivity of the Raman microscope, and the pixel density, achieved here in a timescale of roughly one hour, is a testament to the practical applicability of the system for 2D spectroscopic imaging and high-resolution 1D line-scanning.

2.4 Plasmonic tip preparation

As was discussed in Chapter 1, TENOM techniques utilize sharp metallic probes that can couple with light to excite plasmonic modes, leading to strong localized electric fields

at their apexes, which are used to enhance optical emissions from a nanoscale region on the sample surface. In the case of Raman scattering, the magnitude of this signal enhancement scales non-linearly with the intensity of the local field, so even a marginal increase in the field strength can result in substantial Raman signal gain. Thus, the optical properties of the tip, which dictate the efficiency of optical coupling and the intensity of the enhanced field, are of critical importance for TENOM measurements, particularly those measuring Raman scattering. In this brief section, we will discuss the procedure developed for reliable fabrication of plasmonically active tips, as well as the techniques used to assess their performance.

Plasmonically-active TENOM tips were made via electron-beam evaporation of Au onto commercial contact AFM tips (ATECCont, NanoAndMore). Tips were mounted in a planetary arrangement on a rotating stage, with the tip axes aligned roughly along the axis of rotation and angled $\sim$50° relative to the evaporation direction (see Figure 2.10(a)). In this orientation, the evaporated metal atoms were incident upon the tip sidewalls at a low angle, improving the uniformity of the deposition. A thin (5 nm) Cr layer was deposited first at a low deposition rate (0.1 Å/s) to facilitate adhesion of the subsequent Au layer; approximately 50–100 nm of Au was then deposited on the tip at a rate of $\sim$1.5 Å/s. In some cases, the deposition of an additional Au layer (5 nm Cr / 70 nm Au) on the back side of the cantilever was required for adequate reflection of the beam-bounce laser.

After metal deposition, the quality of the coated tips was assessed by several means. SEM was first used to image the tip apexes at high resolution and provide approximations for the radii of curvature (Figure 2.10(b) and (c)). In some cases, the tips were also used for topographic imaging of specific test structures, which can yield additional information about both the geometry of the tip apex/shaft and its stability during imaging. In particular, the imaging of quantum dots (Figure 2.10(d)) enables clear visualization of

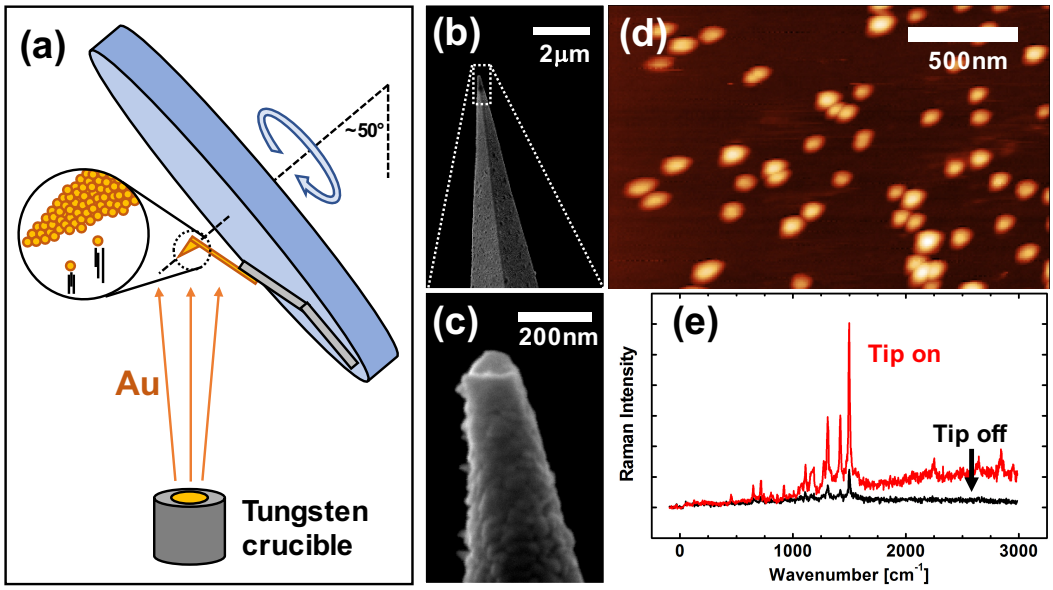

Figure 2.10: **Tip preparation and assessment.** (a) Schematic of the physical arrangement used during the TENOM tip coating procedure to ensure sufficient Au coverage for plasmonic activity. (b) and (c) Electron micrographs of an Au-coated TENOM tip; used to assess coating uniformity and tip radius. (d) AFM topography image of quantum dots on Si; used to evaluate apex symmetry and effective resolution. (e) Tip on and tip off Raman spectra; used to assess plasmonic properties and approximate Raman enhancement factor.

the shape, size and symmetry of the apex, which is the region most responsible for the tip's plasmonic behavior and spatial resolution. The optical activity of these coated tips, which dictates their ultimate performance in TENOM measurements, was qualitatively assessed by a tip-on vs. tip-off experiment. In this measurement, the sample consisted of a thin layer of copper phthalocyanine (CuPc), a strongly Raman-active molecule, atop a substrate of Au (40 nm) on glass. After the focal point of the Raman microscope was carefully aligned with the tip apex, the tip was brought into contact with the CuPc surface and a Raman spectrum taken. The tip was then disengaged from surface and a second spectrum was taken. Comparison of the tip-on and tip-off spectra (Figure 2.10(e)) clearly demonstrates the signal enhancement due to the presence of the tip and allows a qualitative evaluation of the strength of its plasmonic activity.

2.5 Tip-enhanced Raman spectroscopy (TERS)

Having extensively validated the independent performance of both the AFM and the Raman microscope, we next sought to combine and synchronize their operation to perform TENOM (e.g., TERS) measurements of a surface below the diffraction limit. The major goals of this experiment were as follows:

1. Prepare a surface with correlated chemical and topographic variations over nanoscale dimensions.

2. Simultaneously collect topographic and spectroscopic (chemical) data along a line scan of this sample.

3. Demonstrate correlation of chemical and topographic data.

4. Demonstrate sub-diffraction-limited spatial resolution.

In the following sections, we describe the procedures used to prepare the sample and perform the TENOM measurement, and we present and discuss the experimental results, which confirm the successful operation of the TENOM instrument.

2.5.1 Experimental methods

The spatially-patterned sample designed for TERS experiments was prepared using nanosphere lithography (NSL), which provides a straightforward, photoresist-free method to create regular, nanoscale features with well-defined geometries. In this process, Langmuir-Blodgettry was used to deposit a hexagonally close-packed layer of 1 μm silica particles onto the surface of a bare silicon wafer. Electron-beam evaporation was then used to deposit 5 nm of Cr (for adhesion) and 100 nm of Au through the triangular interstitial holes of the microparticle mask. After removing the particles by sonication,

the sample was imaged via AFM, revealing the desired hexagonal array of uniform Au triangles roughly 300 nm across. Next, a two-step process was used to functionalize the Au islands with a monolayer of methylene blue (MB), which was chosen because of its strong Raman scattering under 633 nm excitation. First, the sample was immersed in a 3.5 mM solution of Na_2S for 30 min at 65° to functionalize the Au surface with sulfur, which pulls electron density from the Au and gives the surface a partial negative electrostatic charge. Next, the sulfur-modified Au was immersed in a 0.1 mM solution of MB in 0.1 M NaOH for 30 min, where, due to the basic conditions, cationic MB molecules adhere weakly to the Au surface (procedure adapted from [2]). The result of this procedure is a surface with regular, nanoscale topographic features that are selectively functionalized with a Raman-active molecule. Such correlated topographic and chemical variations make this sample an ideal platform with which to demonstrate the capabilities of the TENOM system.

The first step of the TENOM measurement was to carefully align the focal point of the Raman microscope with the tip apex. First, the tip was engaged on the surface in a suitable region for the desired TENOM experiment. Rough alignment of the system was done by adjusting the micrometer drives of the Raman microscope stage while using the top- and side-view cameras to visually observe the position of the laser spot relative to the tip. From there, the alignment was optimized manually using the microscope's piezo actuators; this optimization process involved iteratively adjusting the three axes of the stage while simultaneously monitoring optical spectra collected by the microscope. As soon as the system was in moderate alignment, a weak photoluminescence signal from the tip was observed in these spectra, and by moving the microscope to maximize this signal, optimal system alignment was achieved. Once aligned, the tip and Raman microscope were held in static alignment for the remainder of the measurement while the sample was independently scanned relative to them both.

The second step of the TENOM measurement, data collection, required controlled stage scanning with synchronized collection of optical spectra and thus, was facilitated by custom LabVIEW software. Using the external control scheme shown in Figure 2.4(b), a topographic image of the sample was acquired to determine a suitable position for a TENOM line scan (i.e., a scan path that passed over several Au islands). Finally, the line scan was performed in the following manner. The sample stage was moved to the selected starting position and a Raman spectrum was collected. The stage was then moved to the next Raman pixel, with LabVIEW recording the surface topography along the way, and the next spectrum was collected. This process was repeated until the line scan was complete, yielding a data set consisting of a 256-pixel topography profile with 50 tip-enhanced Raman spectra taken concurrently at regular intervals along the 3 μm scan line.

2.5.2 TERS results and discussion

The results of the TENOM experiment described above are presented in Figure 2.11, where the left half shows the Raman (top) and topographic (bottom) results of the line scan, along with an inset topographic image of the scan region, and the right half shows selected spectra from the scan alongside a far-field Raman spectrum of bulk MB for comparison. The plots on the left side of the figure are oriented such that the full Raman spectrum corresponding to each position along the topography profile is represented vertically in the column directly above that position. As anticipated, these data demonstrate a clear correlation between raised topography and increased optical signals (i.e., when the tip was positioned over the MB-functionalized Au, optical emission increased). Although most of this signal increase is in the form of a broad fluorescent band, which does not provide the desired local chemical information, there are a few

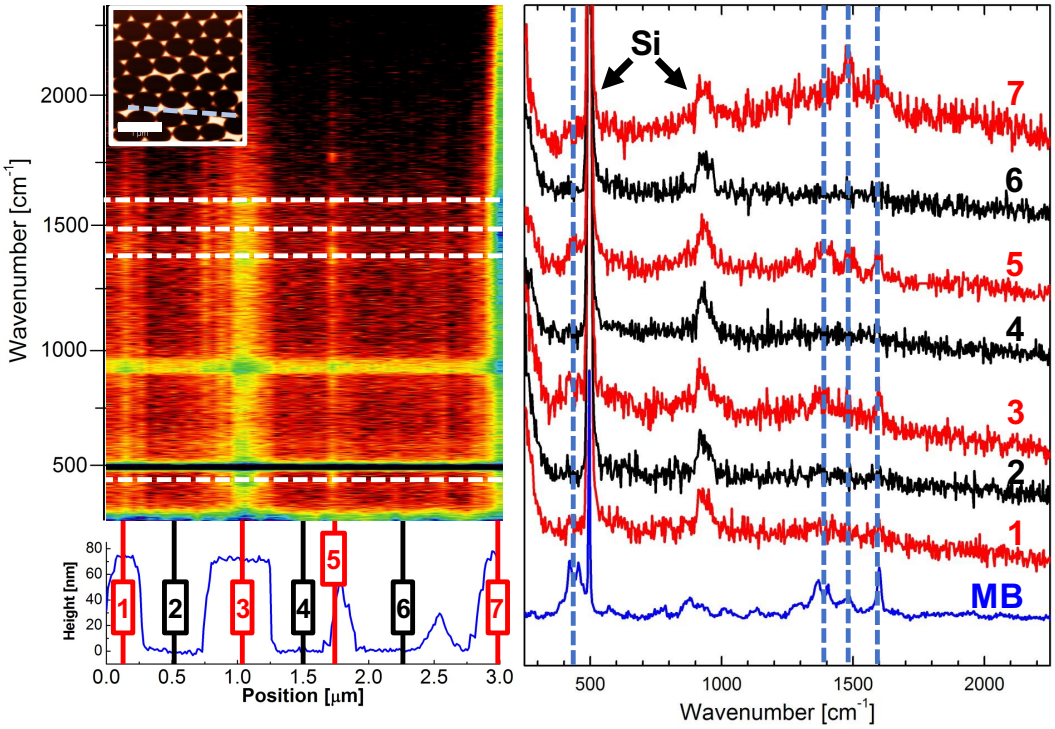

Figure 2.11: **Nanoscale chemical imaging via TERS.** Results of a TERS line scan across methlene blue (MB)-functionalized Au triangles on Si (sample design and experimental procedure described in text). Left: Topography profile (bottom) and corresponding tip-enhanced Raman spectra (above) vertically aligned such that the "Position" axis below applies to both data sets. Spectral variations along the length of the line scan correlate well with changes in the topography and show that optical emission increases when the tip is positioned over the Au features. Right: Individual spectra, taken at the numbered positions marked along the topography profile, plotted along with a far-field Raman spectrum of bulk MB. Vertical dashed lines indicate the characteristic Raman peaks of MB, which are correspondingly shown as horizontal lines in the spectral data on the left. Odd-numbered (red) and even-numbered (black) spectra correspond to the tip being positioned ON and OFF an Au feature, respectively. The ON-Au spectra exhibit spectral features between 1400 and 1600 cm^{-1} that are aligned with the far-field Raman peaks observed in MB. No such features are observed in the OFF-Au spectra, which suggests that they indeed are due to tip enhancement.

spectra that display weak peaks on top of this fluorescence, potentially indicating the local enhancement of MB Raman scattering. To confirm this assertion, some of these enhanced (ON-Au, red) spectra, as well as several featureless (OFF-Au, black) spectra, were plotted alongside a far-field Raman spectrum of bulk MB (blue), and the enhanced

Raman peaks were indexed against the characteristic peaks of MB (dashed lines). The alignment of the enhanced and expected peaks, along with the absence of these peaks in the OFF-Au spectra, strongly suggests that the enhanced Raman scattering in the ON-Au regions was due to the presence of the plasmonic tip, confirming the instrument's ability to locally interrogate surface chemistry. Furthermore, a closer look at the spectra near Position 5 allows an estimate of the system's spatial resolution. The spectrum taken at this position exhibits clear Raman signatures of MB; however, the two spectra taken immediately before and after show no observable Raman enhancement. This suggests that the lateral resolution of the system is smaller than the 60 nm step sized used for this experiment and verifies that the TENOM instrument is capable of chemical imaging at lengthscales well below the diffraction limit.

References

[1] R. Ramos and M. Gordon, "Reflection-mode, confocal, tip-enhanced raman spectroscopy system for scanning chemical microscopy of surfaces," *Review of Scientific Instruments*, vol. 83, no. 9, p. 093706, 2012.

[2] N. G. Tognalli, A. Fainstein, C. Vericat, M. E. Vela, and R. C. Salvarezza, "Exploring three-dimensional nanosystems with raman spectroscopy: methylene blue adsorbed on thiol and sulfur monolayers on gold," *The Journal of Physical Chemistry B*, vol. 110, no. 1, pp. 354–360, 2006.

Chapter 3

Design and validation of an attenuated total reflectance (ATR)-geometry excitation/detection system

Having successfully demonstrated the combined operation of the AFM and Raman microscope for basic TENOM experiments, we now discuss the attenuated total reflectance (ATR) excitation/detection system. This chapter will focus on the design and validation of this system, with a brief explanation of relevant fundamental concepts, as well as a thorough discussion of its applicability toward expanding the capabilities and improving the sensitivity of the TENOM instrument.

3.1 Introduction to ATR principles

One of the primary goals of this thesis project is to improve the understanding of the complex tip-surface optical interactions involved in TENOM experiments, particularly as they pertain to plasmonic excitations, and to leverage this knowledge toward improving Raman enhancement. Although the two-component TENOM instrument demonstrated in Chapter 2 could detect and enhance near-field events, its ability to carefully probe the critical optical interactions between the tip and the surface was inherently limited by several fundamental shortcomings. In theory, the system could be used to measure the tip-surface distance dependence of photoluminescence and Raman and Rayleigh scattering to infer useful information about near-field events and tip-surface coupling. In practice, however, these experiments are very challenging because of the low intensity of the desired signal and the overwhelming contributions from additional optical events. These undesirable background events, often stemming from illumination artifacts such as reflections and multiple-scattering processes [1], are largely irrelevant to the interactions of interest and only serve to convolute the desired signal. Furthermore, these experiments provide no direct measurements of tip-surface optical interactions, but instead require inference from this convolved data. The ATR system was designed and incorporated into the instrument to provide new excitation and detection capabilities and, ultimately, to facilitate flexibility in the design of unique near-field experiments for the careful study of nanoscale tip-surface optical interactions. In particular, the ATR system provides a variety of benefits over the side-on illumination scheme used in the previous chapter:

1. **Highly sensitive to the optical environment at the sample surface:** For reasons that will be discussed below, the ATR system can be acutely sensitive to changes in the optical properties at interfaces, making it useful for detecting important tip-surface optical interactions, such as gap plasmon excitation.

2. **Confined, tunable, and predictable illumination:** The ATR system enables excitation of evanescent fields that are confined to the sample surface and have a well-defined spatial extent that can be tuned by way of the illumination geometry (i.e., angle of incidence).

3. **Reduced spectral background:** Analogously to dark-field optical microscopy techniques, the use of an evanescent illumination scheme prevents direct detection of the pump beam by the Raman microscope (i.e., only scattered light is collected), thereby reducing the optical background compared to side-on illumination.

4. **Decoupled illumination and collection pathways:** The use of separate optical pathways for sample excitation and signal collection (i) enables independent optimization of each system, (ii) simplifies instrument alignment, and (iii) avoids many sources of signal-background convolution that can obscure TENOM results.

5. **Enables the study/use of surface plasmon polaritons:** As will be discussed below, one of the ATR system's most important applications is the excitation and detection of surface plasmon polaritons (SPPs), which are a special type of plasmon mode in the substrate that can be used for signal enhancement and sensitive investigation of tip-surface interactions.

Before elaborating further on the design, applications, and benefits of the ATR system, an understanding of several basic principles is necessary to fully appreciate both the design and operation of the instrument and the subsequent experimental results.

3.1.1 Principles of ATR illumination

ATR is a technique that is used to probe optical interaction (e.g., scattering, absorption) near a dielectric interface (i.e., the sample surface) by controllably generating

evanescent fields at this interface and precisely measuring the flux of optical power across it. As the name implies, these evanescent fields are generated by total internal reflection (TIR) of light at the interface, a process which establishes an optical field that is bound to the interface and decays exponentially with distance (normal to the surface). For the purposes of the TENOM instrument herein, the most important properties of this vertically-confined evanescent field are its spatial extent and how it changes due to interactions with the tip. These properties, which depend on both the material characteristics of the system and the geometry of the excitation configuration, can be understood and predicted using the mathematical formalism of wavevectors.

Wavevectors are a broadly applicable tool for describing the radiative and non-radiative behavior of light in the near-field. A wavevector (k) is a vector representation of the spatial characteristics of a wave; the magnitude of the vector is proportional to the spatial frequency (i.e., 1 / λ), and it points in the direction of propagation. The wavevector of a propagating photon (a.k.a. its momentum) is not a fixed property, like its temporal frequency (ω), but is instead a function of the geometric and material characteristics of its environment, which can be manipulated to control both its direction and magnitude. For example, when light propagates through a high refractive index material, it propagates more slowly than in air; for light of a given energy (fixed ω), this slow propagation results in more closely-spaced wavefronts. Since the wavevector magnitude is inversely proportional to wavelength, the magnitude of the wavevector increases (proportionally to the material index) (see Figure 3.1 (a) and (d)). This has important and relevant consequences regarding the behavior of light at dielectric interfaces. When light is incident upon an interface, Maxwell's equations dictate that the electric and magnetic fields of the light be continuous across the interface. This is mathematically equivalent to requiring that the "interfacial wavevector" (i.e., the spatial frequency of the wavefronts in the plane of the interface) be identical for the incident and transmitted waves. This

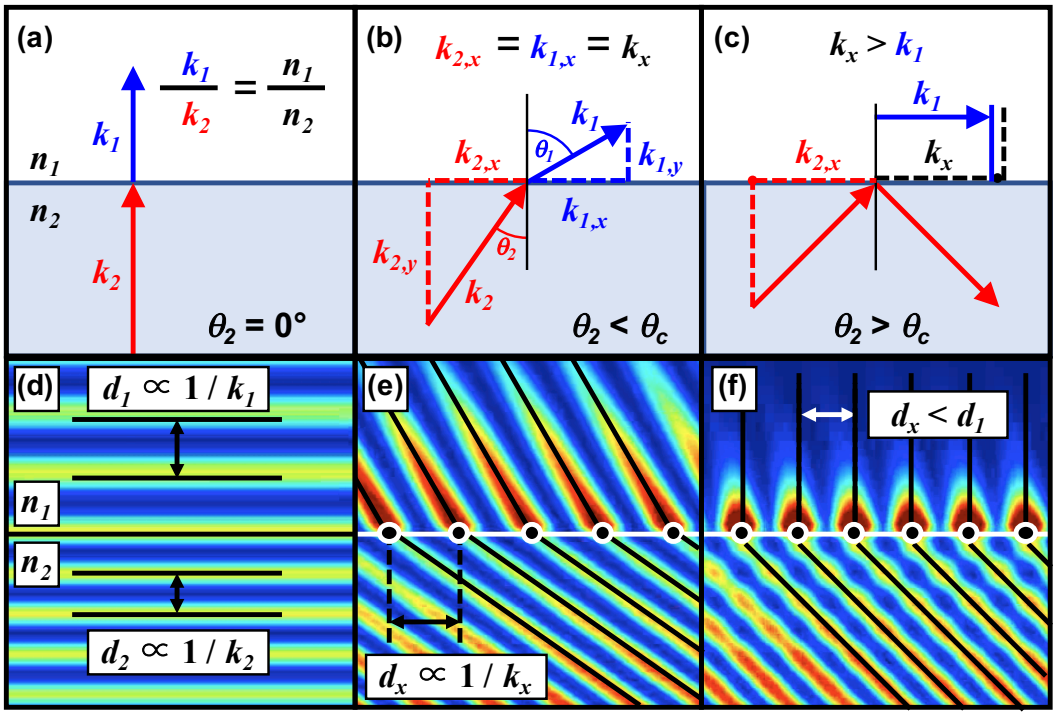

Figure 3.1: **Wavevectors, refraction, and total internal reflection.** (a–c) Wavevector (i.e., reciprocal space) and (d–f) real-space representations of optical phenomena at the interface between a two dielectrics with refractive indices $n_2 > n_1$. (a) and (d) show the effect of refractive index, n_i, on the wavevector, k_i, (a) and wavelength, d_i, (d) of propagating light. (b) and (e) show how the wavevector matching requirement (i.e., $k_{1,x} = k_{2,x}$) at the interface leads to refraction. The real-space equivalent of wavevector matching is the continuity of the electric field across the interface, which is depicted as dots along the interface in (e) and (f). (c) and (f) show the fundamental difference in the system's behavior in the total internal reflection regime. Because the interfacial wavevector of the light, k_x, is larger than the wavevector of propagating light in medium 1, k_1, optical power cannot be transmitted across the interface, and total internal reflection occurs. This results in an evanescent optical field in medium 1 that decays exponentially with distance from the interface.

gives rise to refraction, which is described by Snell's Law:

$$n_1 \sin \theta_1 = n_2 \sin \theta_2 \tag{3.1}$$

where n_i is the refractive index of material i, and θ_i describes the propagation direction in material i, relative to the interface normal (see Figure 3.1 (b)).

In the case of light passing from a high-index dielectric (medium 2) to a lower index material (medium 1) (e.g., light hitting the inside face of a prism), there exists a critical angle, θ_c, beyond which Snell's Law has no real solution because the interfacial wavevector, k_x, is larger than the fixed wavevector, k_1, of propagating light in medium 1 (see Figure 3.1 (c) and (f)). Therefore, this light cannot propagate in medium 1, and all optical power is reflected back into medium 2 (i.e., it undergoes TIR). It is important to clarify that during TIR, optical fields do still exist in medium 1; however, they exhibit a fundamentally different spatial behavior than propagating light. To understand how and why TIR changes the characteristics of these fields, let us first consider the wavevector of a refracted beam in medium 1 (Figure 3.1 (b)) and separate it into its interfacial ($k_{x,1} = k_{x,2} = k_x$) and normal ($k_{y,1}$) components:

$$\begin{aligned} (k_1)^2 &= (k_x)^2 + (k_{y,1})^2 \\ (k_{y,1})^2 &= (k_1)^2 - (k_x)^2 \end{aligned} \tag{3.2}$$

It is apparent here that $k_{y,1}$ becomes purely imaginary when $k_x > k_1$ (i.e., during TIR). The physical consequence of this imaginary value can be seen mathematically using the generic plane wave solution

$$E(x, y, t) = A\, e^{i(k_x x + k_{y,1} y - \omega t)} \tag{3.3}$$

where E is the field strength, and A is the amplitude. For real values of k, this equation describes a propagating plane wave that oscillates in time and space. However, by inserting an imaginary value for $k_{y,1}$

$$E(x, y, t) = A\, e^{i(k_x x - \omega t)}\, e^{-\mathrm{Im}(k_{y,1}) y} \tag{3.4}$$

the spatial behavior of the resulting field transitions from oscillatory to exponentially decaying in the direction normal to the interface. This transition gives rise to an evanescent field in medium 1, which is bound to the interface and decays rapidly with distance. This key conclusion has broad implications regarding the origin and nature of the optical near-field, namely that closely spaced optical fields are evanescent strictly because the fixed wavelength of light prevents them from propagating into the surrounding medium. More specifically to the present discussion, this conclusion aids in the explanation of the ATR system design and provides a simple framework predicting and understanding forthcoming experimental results.

One of the primary benefits of the ATR system is its ability to use evanescent phenomena to confine light to sub-wavelength distances near the sample surface. Although these evanescent fields cannot directly transmit optical power across the interface, they can still interact with matter in many of the same ways as propagating light. As in the case of our system, the presence of analytes or nanostructures near the surface can lead to absorption and scattering of these evanescent fields, which results in a measurable attenuation of the reflected excitation beam. In this way, the ATR system enables the excitation and detection of optical events near the surface with greater "vertical" (normal to the surface) precision than far-field illumination techniques.

By tuning the excitation geometry, the design of our ATR system allows us to access a wider range of interfacial wavevectors at the sample surface than is achievable through far-field illumination. As a result, it enables the direct excitation and detection of a special type of plasmonic mode, called surface plasmon polaritons (SPPs), which can be used to enhance Raman scattering from the sample surface and improve the system's sensitivity to nanoscale tip-surface interactions.

3.1.2 Surface plasmon polaritons

Like other plasmons, SPPs are collective oscillations of the electrons in a metal in response to optical fields, but they differ from the LSPs discussed in Chapter 1 in two important ways. First, SPPs are not localized to sub-wavelength nanostructures like LSPs but are instead a well-defined mode that will propagate along a metal-dielectric interface (Figure 3.2 (a)). Secondly, in contrast to LSPs, which exhibit a sharp resonance at a fixed frequency (as determined by their geometry), SPPs can be resonantly excited over a range of frequencies, so long as the wavevector of the excitation source matches that of the SPP mode. However, because the SPP wavevector is always larger (shorter wavelength) than that of propagating light in the dielectric medium, SPPs cannot be directly excited by far-field illumination of the interface (Figure 3.2 (b)). Thus, to efficiently excite SPPs at, for example, a metal-air interface, large wavevectors must be achieved at the surface using a dielectric material (e.g., glass) with a larger refractive index than air to increase the wavevector of the excitation source. Figure 3.3 (c) shows a common illumination geometry (known as the Kretchmann configuration [2]) for SPP excitation that consists of a thin layer of metal atop a prism. Light that is internally incident upon the prism-metal-air stack will exhibit an interfacial wavevector dependent upon its AOI; by adjusting the AOI, this wavevector can be made to match that of the SPP at the metal-air interface. By optimizing this sensitive wavevector matching condition, optical power can be transferred very efficiently into SPP modes, causing a sharp drop in the reflectance of the prism-metal-air stack that can be measured via ATR techniques. Once excited, these SPPs are confined to the metal-air interface (i.e., they are evanescent in the vertical direction) where they lead to strong electric fields because of the resulting concentration of optical energy.

As with the LSPs discussed in the previous chapters, this enhanced field behaves like

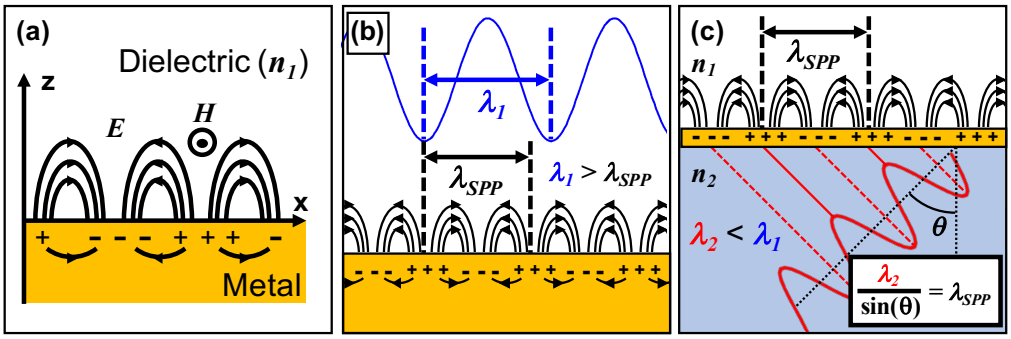

Figure 3.2: **Surface plasmon polaritons.** (a) Depiction of surface plasmon polaritons at a the interface between a metal and a dielectric of index n_1. Charge density waves (+'s and −'s) are shown at the metal surface along with associated electric field lines. (b) The (frequency-dependent) wavelength of the SPP mode is alway shorter than (larger wavevector) that of propagating radiation in the dielectric medium. (c) Schematic representation of the Kretschmann configuration, which uses a second dielectric material (index $n_2 > n_1$) to decrease the excitation wavelength and enable wavevector matching to the SPP mode by tuning the angle of incidence, θ_i.

a strong localized light source and can be used to increase optical emissions (primarily Raman scattering in the present work) from the region near the sample surface, ostensibly leading to improved signal gain. The other major benefit of using SPPs in conjunction with this TENOM instrument is that they provide a sensitive means by which to detect subtle changes in the local optical characteristics near the surface, particularly those caused by the influence of the tip. As alluded to above, the wavevector matching criterion required for SPP excitation is fairly strict, and is, in large part, a function of the dielectric character of the medium near the interface. Even small changes at or near the metal surface, such as the deposition of a few nanometers of analyte, can noticeably change both the efficiency and wavevector dependence of resonant SPP excitation. Thus, with sufficient SPP measurement sensitivity, the ATR system can allow us to dynamically observe tip-induced optical events near the surface by monitoring their effect on SPP resonance.

Having discussed the fundamental physics necessary for understanding the operation

and applications of the ATR system, the remainder of this chapter will focus on the practical design of the system itself and draws on the principles above to interpret and substantiate the results of several validation studies.

3.2 ATR system design

Considering the intended applications described above, the major design requirements for the ATR system are as follows:

1. **Accurate and automated control of AOI:** The interfacial phenomena described above exhibit wavevector-dependent properties that we wish to study; robust control of AOI is necessary to reliably probe these dependences.

2. **Sensitive measurement of reflectance:** Changes in surface reflectance provide insight into near-field events, such as SPP excitation and tip-surface interactions. Given the small size of the tip's near-field interaction volume relative to the far-field excitation volume, highly sensitive reflectance measurements are necessary to detect subtle tip-induced changes.

3. **Mechanically compatible with TENOM instrument:** To incorporate the ATR system with the rest of TENOM instrument, it must be designed with careful consideration of the physical constraints imposed by the preexisting components.

4. **Simple and reproducible sample exchange:** The ability to quickly and easily change between samples in a way that ensures the consistency of results imperative.

This section discusses in detail the physical construction of the ATR system, as well as the principles of its operation and the results of several validation studies.

3.2.1 Physical system design

A schematic representation of the ATR system is shown in Figure 3.3 along with a CAD rendering of the physical design of the system's main component: the custom sample stage. Before describing any components in detail, a brief discussion of the optical pathway is central to understanding the system's basic operation (see Figure 3.3 (a)). Light from a HeNe laser (633 nm, 5 mW) passes through a laser line filter and is directed toward the ATR stage via a series of mirrors. Before reaching the stage, a beam-splitter reflects 8% of the beam onto a reference photodetector that is used to monitor and normalize for fluctuations in the output intensity of the laser. The final mirror in the excitation pathway is mounted on a motor-driven linear translation stage and reflects the beam toward a lens in the stage. Upon exiting the lens, the beam passes through one face of a glass right-angle prism and converges to a focused spot at the sample-air interface. The AOI of the beam at this interface is adjusted by changing the vertical position of the final mirror, which shifts the position of the beam relative to the lens's optical axis. Light that is internally reflected off the sample-air interface is collected by a second lens and focused onto another photodetector, which measures its intensity. Dividing the output of this photodetector by that of the reference detector provides a very precise and stable measurement of surface reflectance (up to five digits of precision) and enables the detection of minute reflectance fluctuations.

In addition to the design and optimization of the optical path, the physical design of the custom stage was also critical in the realization of the ATR system. Because of the size constraints imposed by the fixed geometry of the AFM, Raman microscope, and side-view objective, the design of a stage that could contain the necessary optical components within a sufficiently compact and functional housing was a considerable challenge. The final design of the stage, shown in Figure 3.3 (b), has several features

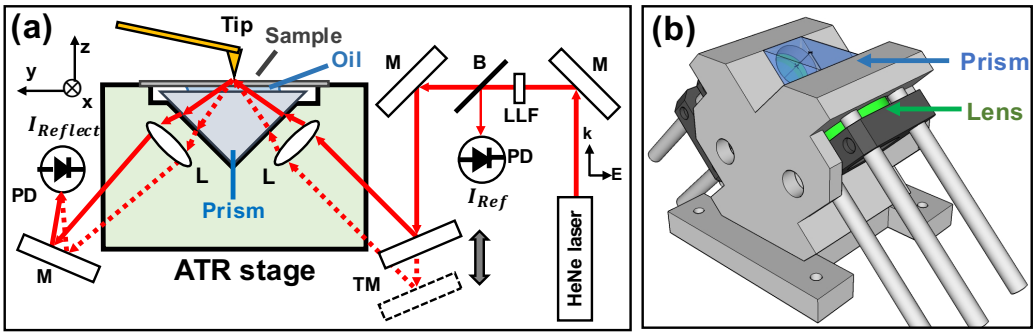

Figure 3.3: **ATR system and stage design.** (a) Detailed schematic of the ATR system's beam path and critical optical elements (B = 92:8 beamsplitter, L = lens, LLF = laser line filter, M = mirror, PD = photodiode, TM = translating mirror). Dashed and solid lines represent two alternate beam paths with different AOIs determined by the position of the translating mirror. (b) Rendering of the physical design of the ATR sample stage, which houses right angle prism and aspheric lenses for focusing the pump beam and collecting the reflected light.

that improve the functionality of the ATR system. In addition to holding the ATR prism, the stage also houses two aspheric lenses (for excitation and collection) and a turning prism, which are attached via an optical cage system. This cage system not only simplifies the adjustment of the lenses for optimization of the excitation and collection pathways, but it also facilitates accurate calibration of the AOI, as will be discussed in the next section.

The other major benefit of the stage design is its compatibility with coverslip samples. Preparing sample surfaces directly on the face of the ATR prism is both expensive and impractical, so the use of glass coverslip samples is preferable. However, this requires that the coverslip be optically coupled to the top surface of the ATR prism to prevent the excitation beam from being reflected and obscured by the air gap between the prism and sample. This is accomplished by bridging this gap with a thin layer of immersion oil, which has the same refractive index as both the prism and coverslip; thus, light is not reflected or refracted at either interface and reaches the sample-air interface unobscured. To enable oil coupling with coverslip samples, the stage was designed with a small gap

to hold immersion oil between the top surface of the prism and bottom surface of the sample. Furthermore, to improve the reproducibility of measurements after removing and replacing a given sample, a ridge was machined into the top surface of the stage to ensure that the sample returned to the same position after each exchange. These two features of the stage enable and simplify the use of coverslip samples in the TENOM instrument.

3.2.2 ATR system alignment and control

In addition to the design of the optical pathway and the custom stage, the development of a functional ATR system also required the establishment of effective alignment, control, and data collection protocols. Quantitative ATR measurements require both accurate angle calibration and precise angle control. As mentioned above, the AOI calibration procedure makes use of the cage system on which the focusing lens is mounted, as well as two alignment plates. These plates each have a 1 mm aperture that, when mounted in the cage system, is exactly aligned with the optical axis of the focusing lens. Thus, with both plates mounted and separated by a few inches, the position and rotation of the translating mirror can be adjusted to maximize the transmission of light through the sequential apertures. At this optimal position, the excitation beam is parallel to and aligned with the optical axis of the lens, which corresponds to an AOI of 45°. After subsequent movements of the translating mirror, the AOI is calculated by comparing the new position back to this reference position and inserting the difference (Δy) into the following relation, which was determined from ray-tracing (i.e., Snell's Law).

$$\theta_i \;=\; \sin^{-1}\!\left(\frac{1}{n}\,\sin\!\left(\tan^{-1}\frac{\Delta y/\sqrt{2}}{f}\right)\right) \;+\; 45^\circ \tag{3.5}$$

where n is the refractive index of the sample, and f is the focal length of the lens.

Irrespective of the accuracy of this calibration process, quantitative determination of the AOI over a range of angles also necessitates precise control and measurement of the mirror position. This requirement motivated the use of a high-precision calibrated servo motor to drive the movement of the mirror. USB interfacing between this motor and LabVIEW provided a continuous digital readout of its position, with micron resolution, and facilitated remote control of the device for automated scan routines. As with the other components of the TENOM instrument, custom LabVIEW programs were used extensively to synchronize numerous aspects of instrument control (e.g., mirror position, XY stage position, tip Z position) and data collection (e.g., ATR reflected and reference intensities, Raman spectra, tip deflection). This exceptional scope of instrument control enabled the development of a wide variety of experiments, ranging from simple validation measurements, such as reflectance vs. AOI, to the complex studies presented in Chapters 4 and 5.

3.3 ATR system validation

Before applying the ATR system to complex TENOM measurements, it was first necessary to rigorously evaluate the capabilities and quantitative accuracy of the system by performing a series of validation experiments and comparing the results to theoretical predictions. The following sections focus on several of these studies, along with corresponding theoretical calculations and simulations, which confirm the accuracy and functionality of the ATR system.

3.3.1 FDTD simulations

While it is straightforward to use electromagnetic theory to assess the results of certain basic measurements that have simple analytical solutions, many applications of the ATR

and TENOM systems cannot be theoretically predicted as easily. Thus, an important aspect of system validation was the development and refinement of optical simulations to accurately model the system and provide predictions that can be directly compared with experimental results. Finite-difference time-domain (FDTD) optical simulations (Lumerical) were used extensively for this purpose. FDTD is a numerical simulation technique that uses Maxwell's equations to predict how a pulse of light will travel through a material system of a given geometry. By appropriately positioning monitors within the simulation, properties, such as surface reflectance and local field strength, can be calculated. In addition to providing insightful visualizations of nanoscale and evanescent optical events, simulation outputs have experimentally testable analogs that enable both instrument validation and simulation refinement. The results discussed in the remainder of this chapter will begin with the most rudimentary application of the ATR system: the study of TIR at a glass-air interface. By directly comparing the experimental and simulation results with well-understood theory, this simple measurement can help determine the FDTD simulation parameters that faithfully represent experimental conditions. As the accuracy of the FDTD model is further refined and the instrument is applied to increasingly complex systems (see Chapters 4 and 5), simulations become a powerful tool for TENOM system optimization, as well as qualitative understanding and corroboration of experimental results.

3.3.2 TIR at a glass-air interface

The first and simplest test of the ATR system involved the study of TIR at a glass-air interface. In this experiment, the AOI-dependent reflectance of the interface was measured over a range of angles near the critical angle, and the results were compared to theory and simulations. The goals of this study were threefold:

1. Assess the quantitative accuracy of the critical angle by comparing experimental results with Snell's Law.

2. Qualitatively compare the angle-dependent reflectance profile to that predicted by the Fresnel equations.

3. Demonstrate good agreement between simulations and experimental results.

Before discussing measurement data from the TIR experiment, it is important to first describe the expected results using Snell's Law and the Fresnel equations. Given the known refractive index of the glass ($n = 1.515$), the critical angle can be easily calculated from Eqn. 3.1:

$$\theta_c \;=\; \sin^{-1}\!\left(\frac{1}{1.515}\,\sin 90^\circ\right) \;=\; 41.3^\circ \tag{3.6}$$

This result suggests that for all AOI greater than 41.3°, the reflectance of the glass-air interface should be 100%. However, Snell's Law alone does not provide insight into the expected profile of the reflectance vs. AOI measurement at angles approaching θ_c; for this, the Fresnel equations must be used. The Fresnel equations describe the transmission and reflection coefficients of light at interfaces as a function of the dielectric properties of the materials and the AOI and polarization of the light. In the case of the simple system of a glass-air interface and purely p-polarized light, the Fresnel equations predict the following angle-dependent reflectance:

$$R\left(\theta_i\right) \;=\; \left|\frac{1.515\sqrt{1-(1.515\,\sin\,\theta_i)^2}-\cos\,\theta_i}{1.515\sqrt{1-(1.515\,\sin\,\theta_i)^2}+\cos\,\theta_i}\right|^2 \tag{3.7}$$

This solution is plotted alongside the corresponding experimental results in Figure 3.4 (a), with the theoretical critical angle also shown by a vertical dashed line. It is immediately clear from this comparison that the qualitative behavior of the experimental reflectance profile differs considerably from the Fresnel prediction. The primary reason

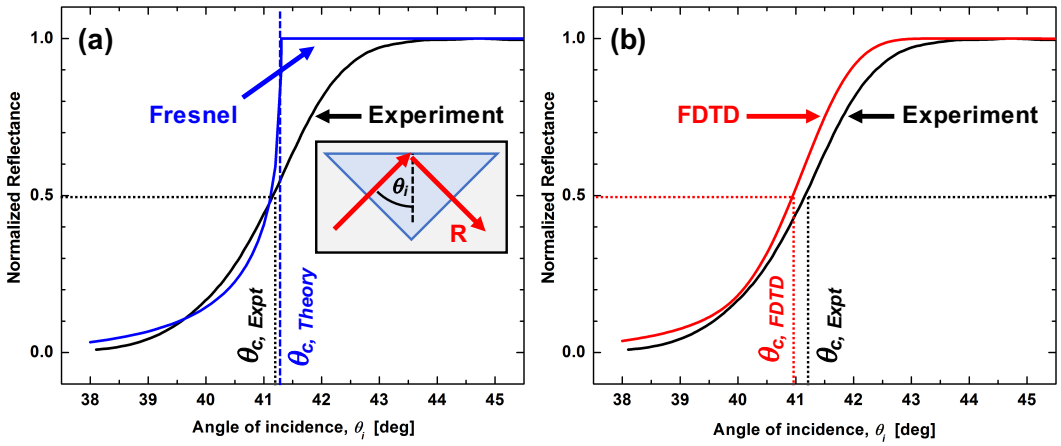

Figure 3.4: **Total internal reflection at a glass-air interface.** (a) Experimentally observed reflectance, R, of a glass-air interface as a function of angle of incidence, θ_i (black) compared with the theoretical prediction from Eqn. 3.7 (blue). The critical angle of the experimental profile, $\theta_{c,Expt}$, is approximated as $\theta(R = 0.5) = 41.2°$; the theoretical critical angle (blue vertical dashed line) is $\theta_{c,Theory} = 41.3°$. (b) Comparison of the experimental reflectance profile with that calculated using FDTD simulations. The estimated critical angle of the FDTD results, $\theta_{c,FDTD} = \theta(R_{0.5}) = 40.9°$, compares well with experiment.

for this is related to the nature of the illumination in the ATR system. Because a lens is used to focus the ATR beam into a small spot ($\sim 8 \times 11$ μm), the light incident upon the surface is not a perfectly parallel beam as Eqn. 3.7 assumes, but is instead converging, meaning that it displays a distribution of wavevector angles. Thus, one would expect the experimental reflectance profile to be a convolution of the Fresnel solution and the angular distribution of the converging ATR beam. Because of the resulting broadening, we approximate $\theta_{c,Expt}$ as the angle at which the reflectance is 0.5 (i.e., the angle at which half of the pump beam's angular distribution is in the TIR regime). This rough estimate of $\theta_{c,Expt} = 41.2°$ is in excellent agreement with Snell's Law.

The discrepancy between theory and experiment, even in this simple case, affirms the importance of simulations that realistically model the behavior of the system and can be used to predict and explain results in more complex studies. FDTD simulations were therefore developed to model the same TIR experiment as above; the results are

compared with experiment in Figure 3.4 (b). Despite the slight difference in critical angle ($\theta_{c,FDTD} = 40.9°$), the overall qualitative agreement between the experimental and simulation profiles confirms the ability of the FDTD model to faithfully represent the true ATR system performance.

3.3.3 SPP excitation

As discussed in Section 3.1.2, SPPs are significant to the ultimate goals of the TENOM instrument because they provide a means to enhance optical signals and to improve tip-surface interaction sensitivity [3–6]. Having demonstrated the use of theory and simulations to validate the accuracy of the ATR system for measuring TIR, we now discuss results of similar investigations regarding SPP excitation. The goals of these experiments were as follows:

1. Use the ATR system to satisfy the SPP wavevector matching criterion and detect the characteristic reflectance drop associated with SPP excitation.

2. Use simulations and theory to validate experimental results regarding the SPP excitation profile and the surface plasmon resonance (SPR) angle.

3. Demonstrate the sensitivity of the SPP excitation profile to changes in the optical characteristics of the sample surface.

Although SPPs can be excited at the surface of any metal, the efficiency of the plasmon excitation depends critically on the frequency of the excitation source relative to an inherent property of the metal known as its plasma frequency. Most metals exhibit plasma frequencies in the ultraviolet range, which prevents the efficient excitation of plasmon modes using visible light. However, a few metals, namely silver and gold, have plasma frequencies that enable strong plasmonic coupling with narrow ranges of the

visible spectrum. In the case of the present instrument, which uses 633 nm excitation, Au is the ideal choice for plasmonic applications. Thus, simulations were used to predict the optimal sample geometry (i.e., Au layer thickness) for efficient SPP excitation at a Au-air interface using 633 nm illumination in a Kretchmann configuration. The results indicated that a Au layer thickness of 40 nm was associated with the most efficient optical coupling and the strongest field enhancement at the sample surface. Electron-beam evaporation was used to prepare a sample consisting of a 40 nm Au layer (with 1.5 nm Cr for adhesion) atop a glass coverslip, and the ATR system was used to measure the angle-dependent reflectance of the sample's surface.

The resulting reflectance profile is shown in Figure 3.5 (black solid line), alongside the profiles predicted by both simulations (red dotted line) and a multi-interface extension of the Fresnel equations (blue dashed line; see [7]). The sharp dip in the reflectance around 44.5°is a characteristic indication of SPP excitation at the Au-air interface, and the position of minimal reflectance (R_{min}) is known as the surface plasmon resonance (SPR) angle, or θ_{SPR}. The experimental results show a broader trend than the Fresnel solution predicts because of the same incident wavevector angular distribution discussed previously. Nevertheless, the SPR angle provides a quantitative measure by which experiment and theory can still be directly compared. The SPR angle of 44.8° exhibited by the data matches very well with that of the Fresnel solution ($\theta_{SPR} = 44.7°$), confirming once again the accuracy of the ATR system's angular resolution. Comparing the simulation results with the experimental data, the excellent agreement further confirms the legitimacy of these simulations as a tool for predicting, explaining, and validating the results of the ATR system.

Finally, to assess the sensitivity of SPP excitation to changes in the dielectric environment near the sample surface, reflectance measurements were performed on a series of Au surfaces, which were coated with alumina (Al_2O_3) layers of varying thickness.

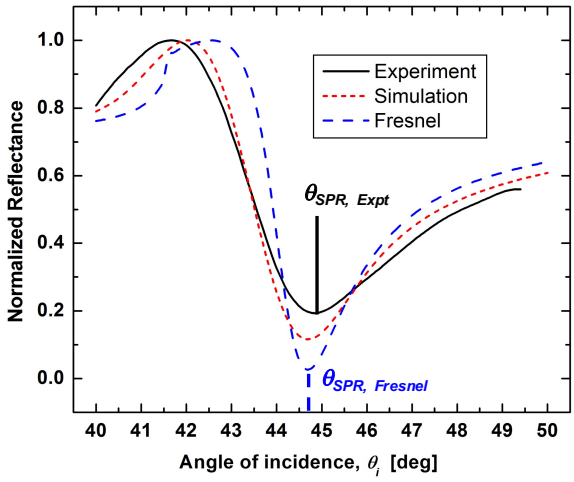

Figure 3.5: **SPP excitation at an Au-air interface.** AOI-dependent reflectance of an ATR-excited thin Au/Cr (40 nm/1.5 nm) layer on a glass coverslip, compared with theory (Fresnel) and FDTD simulations. Maximum coupling to SPPs occurs near $\theta_{SPR,Expt} = 44.8°$; this compares well with the theoretical resonance angle $\theta_{SPR,Fresnel} = 44.7°$.

Atomic layer deposition (ALD) was used to controllably and uniformly deposit Al_2O_3 layers of 2.5, 5.0, 7.5 and 10 nm atop Au substrates, which were prepared by the method described previously. Reflectance profiles of these samples were measured and compared with that of the bare Au substrates in the hopes of observing a significant shift in the SPP resonance properties due to the presence of the thin dielectric layer. Corresponding simulations were also performed for comparison.

Figure 3.6 shows the results of these measurements and simulations. As expected, changes in the reflectance curves, regarding both the position and magnitude of the SPR dip, are observed in response to even a thin Al_2O_3 layer on the Au surface. The experimental data deviate from the simulations more noticeably than in the examples above, possibly due to alloying at the Cr/Au interface during ALD, which is performed at 300°C. Nevertheless, the behavior of the experimental results, namely the increase in θ_{SPR} and decrease in R_{min} with increasing Al_2O_3thickness, exhibits clear monotonic trends that qualitatively mirror those predicted by simulations. These results successfully

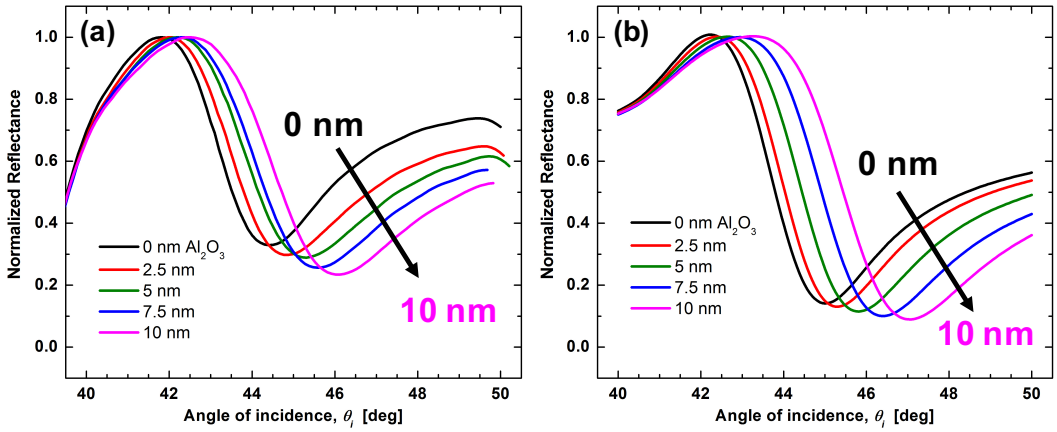

Figure 3.6: **The effect of thin Al_2O_3 layers on surface plasmon resonance at the Au-air interface.** (a) AOI-dependent reflectance, R, of Au/Cr/glass substrates with ALD-deposited Al_2O_3 surface layers of varying thickness. (b) Complementary reflectance profiles calculated using FDTD simulations. Despite quantitative differences between experimental and simulation results, both show similar monotonic changes in R_{min} and θ_{SPR} with increasing Al_2O_3 layer thickness.

demonstrate the sensitivity of SPPs to small changes in the dielectric environment near the Au-air interface. Although, detecting similar dielectric changes caused by the tip is far more challenging because of the nanoscale size of the tip's interaction volume, the ATR system is sensitive to reflectance changes at least three orders of magnitude smaller than those shown above. In the remaining chapters, we will show how this exceptional precision enables the direct detection of a variety of tip-surface optical interactions when the ATR system is used in conjunction with the other two components of the TENOM instrument.

References

[1] R. Ramos and M. Gordon, "Near-field artifacts in tip-enhanced Raman spectroscopy," *Applied Physics Letters*, vol. 100, no. 21, p. 213111, 2012.

[2] E. Kretschmann and H. Raether, "Notizen: Radiative decay of non-radiative surface plasmons excited by light," *Zeitschrift für Naturforschung A*, vol. 23, no. 12, pp. 2135–2136, 1968.

[3] J. Giergiel, C. Reed, S. Ushioda, and J. Hemminger, "Attenuated-total-reflection study of pyridine overlayers on silver films," *Physical Review B*, vol. 31, no. 6, p. 3323, 1985.

[4] B. Rothenhäusler and W. Knoll, "Surface plasmon microscopy," *Nature*, vol. 332, no. 6165, pp. 615–617, 1988.

[5] K. Kato, Y. Aoki, K. Ohashi, K. Shinbo, and F. Kaneko, "Evaluation of C15TCNQ Langmuir-Blodgett ultrathin films on aluminum thin films by attenuated total reflection measurements," *Japanese Journal of Applied Physics*, vol. 35, no. 10R, p. 5466, 1996.

[6] Y. Liu, S. Xu, B. Tang, Y. Wang, J. Zhou, X. Zheng, B. Zhao, and W. Xu, "Note: Simultaneous measurement of surface plasmon resonance and surface-enhanced Raman scattering," *Review of Scientific Instruments*, vol. 81, no. 3, p. 036105, 2010.

[7] M.-S. Tomaš, "Recursion relations for generalized Fresnel coefficients: Casimir force in a planar cavity," *Physical Review A*, vol. 81, no. 4, p. 044104, 2010.

Chapter 4

Nanoscale optical and chemical measurements with the TENOM instrument

In the previous chapters, we discussed in detail the design and validation of the individual components of the TENOM instrument, and in Chapter 2 we demonstrated how the Raman microscope and AFM could be combined to perform nanoscale chemical imaging via TERS. In this chapter, we show how the incorporation of the ATR system dramatically expands the capabilities of the TENOM instrument and enables a variety of unique and meaningful near-field optical experiments. More specifically, this chapter examines the application of the instrument toward achieving the following goals:

1. Demonstrate the unique capabilities of the TENOM instrument by performing experiments that combine the ATR system with the other two components; assess the accuracy of these experiments by comparing results to theory and simulations.

2. Combine the AFM, Raman microscope, and ATR system to perform chemical imag-

ing (via TERS) using the ATR illumination geometry.

3. Quantitatively compare the results of ATR and side-on illumination TERS measurements, with emphasis on the relative signal strengths and enhancement factors.

4.1 Combined operation of the TENOM instrument

By combining and synchronizing the operation of the ATR stage with the AFM and Raman microscope, the TENOM instrument can be used to perform a variety of near-field optical experiments. Because of the number of potential combinations and arrangements of the three main components, the instrument exhibits unique flexibility and versatility regarding the design of such experiments. In this chapter and the next, we will demonstrate and discuss several noteworthy applications of the combined instrument. To aid in visualizing these studies, the schematic of the full TENOM system, previously discussed in Chapter 2, is shown again in Figure 4.1 (a), along with a schematic of the ATR beam path (Figure 4.1 (b)) and a 3D rendering of the physical system layout (Figure 4.1 (c)).

4.1.1 Combined operation modes

The most commonly employed instrument operation mode involves the synchronized use of the AFM and the ATR system to precisely control the lateral and vertical position of the TENOM tip relative to the ATR focal spot and the sample surface, respectively. This allows us to carefully study interactions between the tip and the evanescent field near the surface by measuring changes in reflectance (via the ATR system) and/or far-field scattering (via the Raman microscope) as a function of tip-surface distance. The results of these measurements, referred to broadly as approach curves, provide a wealth

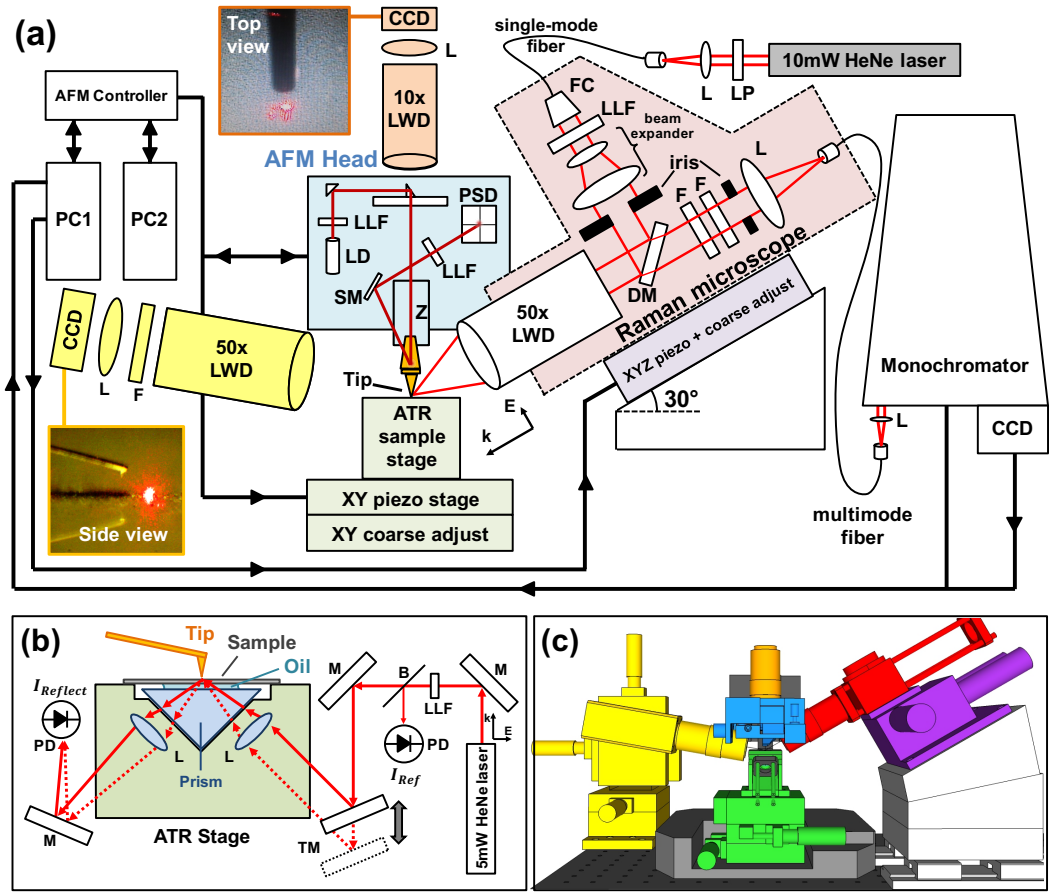

Figure 4.1: **TENOM instrument design.** (a) Schematic of the tip-enhanced near-field optical microscope with side-on and ATR-based illumination systems. (b) Detail of the ATR illumination stage. (c) 3D view of the overall microscope design: yellow = side-view objective and camera; green = coarse and piezo xy stages + ATR sample stage; blue = beam bounce AFM; orange = top-view objective and camera, red = side-on confocal Raman microscope; and purple = xyz piezo stage for Raman microscope. Note: B = beamsplitter, CCD = charge coupled device, DM = dichroic mirror, F = filter, FC = fiber coupler, L = lens, LD = infrared laser diode, LLF = laser line filter, LP = linear polarizer, LWD = long working distance objective, M = mirror, PC = personal computer, PD = photodiode, PSD = position-sensitive detector, SM = steering mirror, TM = translating mirror, and Z = AFM z-piezo.

of valuable information, such as the spatial extent of the evanescent field (see Section 4.2) and the distance scaling behavior of tip-surface plasmonic interactions (see Chapter 5). Another useful system configuration combines ATR sample illumination and side-on optical collection via the Raman microscope; this enables localized excitation and detec-

tion of analytes and fluorophores near the sample surface due to the vertical confinement of the evanescent pump field. As will be discussed in Section 4.3, this configuration also enables the qualitative assessment of SPP field intensity by measuring the AOI-dependent enhancement of Raman scattering from analytes on a Au surface. Finally, the combined operation of all three components facilitates a diverse range of applied and fundamental optical experiments at the nanoscale; two such experiments are discussed in the coming chapters. First, in Section 4.4, we demonstrate that ATR illumination is a viable excitation geometry for nanoscale chemical imaging of surfaces via TERS. Second, in Chapter 5, the TENOM instrument is applied to fundamental studies of plasmonic tip-surface interactions, specifically their distance scaling behavior and their effect on Raman enhancement.

4.1.2 Mutual alignment of TENOM components

Complex TENOM studies that combine all three components of the TENOM instrument require the AFM tip, the Raman microscope, and the ATR system to be mutually aligned. This process consists of two steps: (i) alignment of the ATR excitation spot with the AFM tip apex, and (ii) alignment of the Raman microscope focal point with the tip apex. A thorough description of the alignment procedure can be found in Appendix A; only the critical aspects of the process will be discussed below.

Precise alignment of the AFM tip with the ATR spot is critical for many of the measurements below, particularly those involving approach curves (i.e., $[X]$ vs. tip-surface distance). In these experiments, the position of the tip relative to the spot strongly affects the magnitude—and in some cases the qualitative nature—of the tip-field interactions. Thus, to ensure reproducibility, the tip is realigned with the center of the ATR spot before each measurement. First, the tip and ATR spot are moved

into rough alignment by adjusting the micrometer drives of the stage and using the top- and side-view cameras to monitor the position of the spot relative to the stationary tip. The ATR spot would ideally be "invisible" (i.e., no light escaping into the air above the sample surface), but due to imperfections in the interface, a small fraction of the light is scattered, making the spot visible from above. Fine adjustment of the alignment is performed by first lowering the tip into the evanescent field above the spot, where it acts as an antenna to scatter light into the far-field. This can be clearly observed in the side-view camera, and it also results in a detectable drop in the reflectance of the surface due to the loss of optical power into the far-field. The x and y piezos of the stage are then adjusted via LabVIEW to maximize this reflectance attenuation, at which point the tip is assumed to be in optimal alignment with the ATR spot.

In comparison to the process described in Chapter 2, the alignment of the Raman microscope and the AFM tip is dramatically simplified by using the ATR system. As with the procedure above, the tip lowered into the evanescent field above the ATR spot until it begins to visibly scatter light. The Raman filter, which strongly rejects the 633 nm pump light during Raman measurements, is removed from the microscope momentarily to allow efficient collection and detection of this elastic scattering. The monochromator and CCD are used to measure the amount of scattered light collected by the Raman microscope while the micrometer drives and piezos of the microscope stage are used for coarse and fine alignment of the Raman microscope, respectively. Once the collection efficiency is maximized, the Raman microscope is assumed to be in optimal alignment with the tip apex. The Raman filter is returned to the microscope, and the TENOM instrument is ready for use.

4.1.3 Simulations of the TENOM system

As in Chapter 3, FDTD simulations were carried out to predict and interpret system observables, such as sample reflectance, far-field scattering and E-field profiles as a function of AOI and tip-surface geometry. Simulations were particularly helpful in understanding and validating the results of ATR-illumination experiments, as well as critically comparing ATR with side-on (top-side) illumination. Most simulations (see Figure 4.2) were performed in two dimensions (2D) because memory and time requirements for comparable 3D simulations were prohibitively large in many cases; however, several 3D simulations were performed to validate the use of 2D simulations as a quantitatively accurate alternative. Simulations were performed using perfectly matched layer (PML) boundary conditions to gradually attenuate fields at the boundaries without reflections back into the system. A thin lens-approximated field source was used for both top-side and ATR-illumination simulations to accurately model the convergence of the experimental pump beams, according to the numerical apertures of their respective focusing optics. The frequency of the source was fixed at 473.8 THz (632.8 nm HeNe light), and E-fields were p-polarized relative to the surface. Figure 2 shows the geometric arrangement of typical simulation areas under (a) ATR and (b) top-side illumination. In both cases, the "sample" consisted of 1.5 nm of Cr and 40 nm of Au atop a semi-infinite glass slab of refractive index $n = 1.515$, and a triangular Au tip with a radius of curvature of 50 nm at the apex was positioned 2 nm above the Au-air interface. A field monitor positioned 1 nm above the same interface was used to measure the field intensity in the tip-surface gap, and transmission monitors in the lower left quadrant measured the overall reflectance of the system (ATR simulations only).

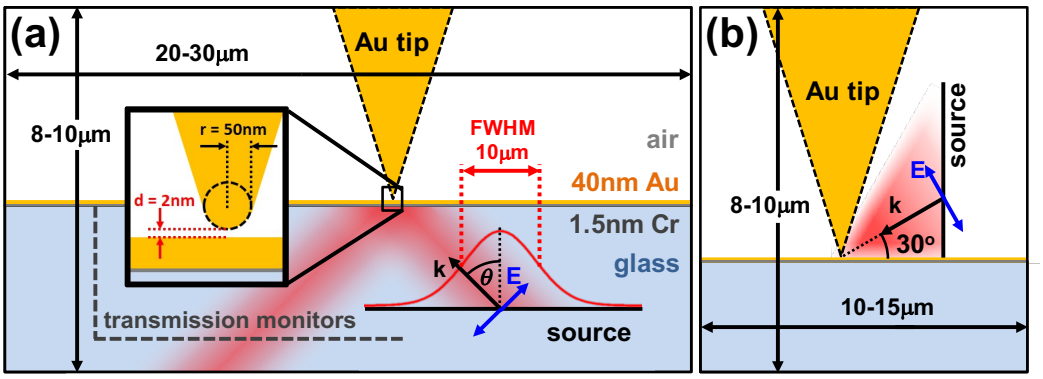

Figure 4.2: **FDTD simulation setup.** Details of FDTD optical simulations of TENOM operation modes for (a) ATR and (b) side-on excitation modes.

4.2 Quantitative assessment of evanescent field profiles

The ability to quantitatively transduce (detect via scattering into the far field) near-field optical phenomena (i.e., local E-fields in x, y and z) is important for interrogating and understanding light-matter interactions at sub-diffraction limited dimensions. The unique design of the present TENOM instrument not only enables tunable excitation of evanescent fields at the sample surface via the ATR illumination geometry, but it can also quantitatively measure the spatial extent of these fields using the AFM tip as a transducer. To demonstrate the latter, we used spectroscopy and reflectance measurements to study the evanescent field generated above an air-glass interface in the total internal reflection (TIR) regime.

4.2.1 Theoretical determination of evanescent decay length

Theoretical predictions of the spatial extent of evanescent fields are essential for quantitative assessment of ATR measurement results. As shown in the previous chapter, the vertical decay of the field is a function of its wavevector (see Eqn. 3.4), which, in turn, is

a function of both the excitation geometry and the refractive indices of the sample and surrounding medium. Thus, the exponential decay length of the field, $d = 1/\mathrm{Im}(k_{y,1})$, can be controlled via the AOI (θ_i) of the excitation beam, and it is predicted by manipulation of Eqn. 3.2:

$$\begin{aligned}
(k_{y,1})^2 &= (k_1)^2 - (k_x)^2 \\
(k_{y,1})^2 &= (k_2 \sin\theta_c)^2 - (k_2 \sin\theta_2)^2 \\
(k_{y,1}) &= \frac{2\pi n_2}{\lambda}\sqrt{\sin^2\theta_c - \sin^2\theta_2} \\
d &= \frac{1}{\mathrm{Im}(k_{y,1})} = \frac{\lambda}{4\pi n_2}(\sin^2\theta_c - \sin^2\theta_2)^{1/2}
\end{aligned} \tag{4.1}$$

where λ is the wavelength (in vacuum), n_2 is the refractive index of the sample, and θ_c is the critical angle, as determined from Snell's Law [1]. This result provides an important and quantitatively testable description of the spatial extent of the evanescent fields generated during ATR experiments.

4.2.2 Experimental measurement of evanescent fields resulting from TIR

To measure these profiles experimentally, optical fields were generated using the ATR system to fix the AOI of the pump laser at an angle greater than $\theta_c = 41.3°$. At each angle, the AFM's z-piezo was used to slowly lower the Au-coated TENOM tip onto the sample surface in the center of the ATR excitation spot. During tip approach, the reflectance of the glass-air interface was monitored while the top-side Raman microscope simultaneously collected and measured the Rayleigh light elastically scattered into the far field by the tip. By plotting the tip-surface distance dependence of the reflectance change and the scattered light intensity, the spatial extent of the evanescent field was

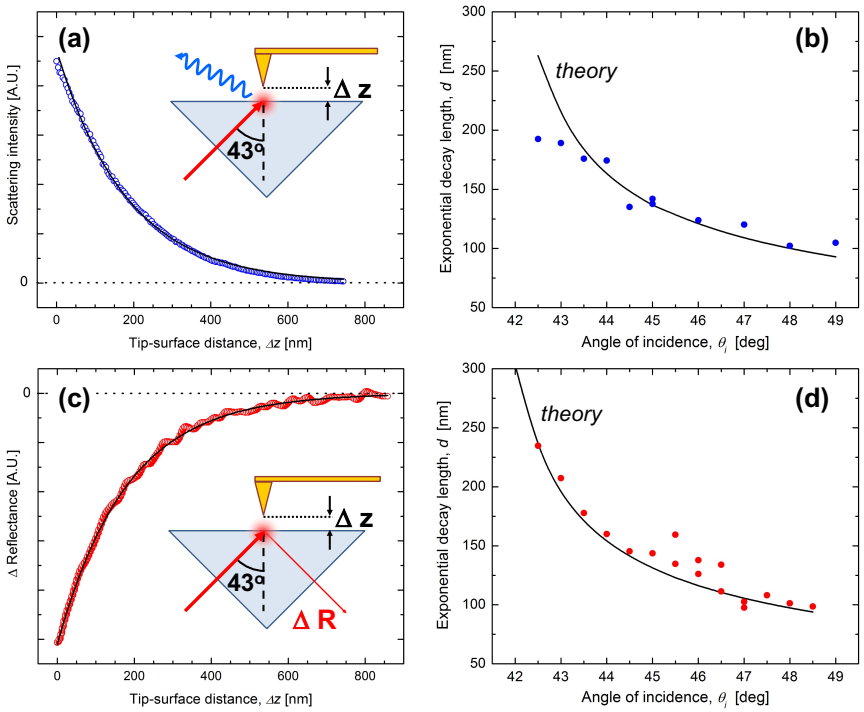

Figure 4.3: **Measuring the spatial extent of the optical near-field.** Example of how evanescent fields above a sample surface excited near the TIR angle can be transduced into the far-field (detected) via (a) tip scattering and (c) spoiling of surface reflectivity as the tip approaches the surface. Black lines are exponential fits to determine the evanescent field decay lengths, with fit data summarized in panels (b) and (d) for tip scattering and surface reflectivity, respectively, at various AOIs. Black lines in panels (b) and (d) are theoretical decay lengths of the evanescent field above a surface excited by TIR for various AOI [1].

measured (see Figure 4.3 (a) and (c)). Similar approach curves were measured over a range of AOIs from 42° to 49°. The resulting experimental profiles were numerically fit to exponential functions of the form $f(\Delta z) = A\ \exp(\Delta z/d)$ to determine the decay length, d, as function of θ_i. Figures 4.3 (b) and (d) show that these experimentally-determined $d(\theta_i)$ agree quantitatively with Eqn. 4.1, demonstrating that the tip can indeed be used as a transducer for optical detection of local E-fields near the surface and that the field distributions match theoretical predictions.

4.3 SPP Raman enhancement

In Chapter 3, SPPs were discussed in detail because of their potential for improving sensitivity and signal strength in TENOM experiments, and measurements of SPP excitation were successfully demonstrated. However, the ATR system alone did not provide direct information about the strength of the SPP-induced E-field at the sample surface or the extent to which it enhances Raman scattering. Thus, we investigated the latter via the following experiment, which combines the operation of the ATR system and the Raman microscope to measure the AOI-dependence of Raman scattering from a thin analyte layer on Au.

Given the strong AOI dependence of the SPR condition, it follows that the intensity of SPP-enhanced E-fields at the Au-air interface is also a function of the AOI of the pump source (i.e., SPP excitation efficiency) and should have a maximum at or near the SPR angle observed in the reflectance profile (Figure 4.4). Raman spectroscopy was used to experimentally measure the angle-dependence of the interfacial E-field intensity by exploiting the fact that Raman scattering scales with pump field intensity. A thin (2–3 nm) film of thermally-evaporated CuPc atop the Au surface was used as a Raman reporter layer; CuPc was chosen for its large resonant Raman cross-section under 633 nm excitation. The ATR illumination configuration was used to pump the sample over a range of AOI while the top-side Raman microscope was used to collect and analyze the light scattered from the surface. Figure 4.4 (b) shows several representative Raman spectra taken during this experiment and illustrates the strong angle dependence of Raman scattering intensity from the CuPc layer at and around the SPR angle. Plotting the integrated intensity of the strongest Raman peak (1490–1510 cm^{-1}) as a function of AOI (Figure 4.4 (c)) reveals a clear maximum at $\sim 44°$; this result is in excellent qualitative agreement with the angle-dependent field intensity predicted by FDTD simu-

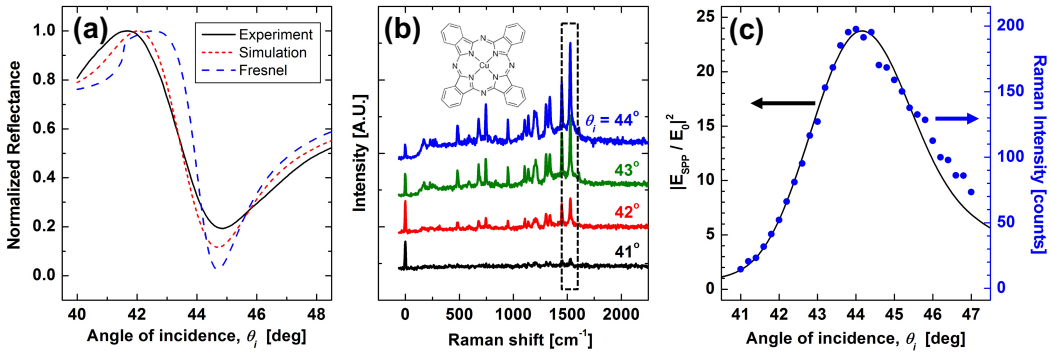

Figure 4.4: **SPP Raman enhancement.** (a) AOI-dependent reflectivity of an ATR-excited thin Au/Cr (40 nm/1.5 nm) layer on a glass coverslip, compared with theory (Fresnel) and FDTD simulation; maximum coupling to SPPs occurs near 44.8°. (b) Far-field Raman spectra of a 2–3 nm thick CuPc layer atop the sample in (a) collected using the side-on confocal microscope from above for various ATR AOI. When SPP excitation is very efficient (∼44–45° AOI), surface reflectivity is low (cf. panel (a)) and Raman signatures of CuPc are very intense (blue trace in (b)). (c) Intensity of the 1500 cm^{-1} Raman band from CuPc (dashed box in panel (b)) for various AOIs, compared to the expected SPP field intensity $(E_{SPP}/E_0)^2$ above the Au/Cr layer determined from FDTD simulations.

lations (black line). We also note that the intensity of the Rayleigh line (0 cm^{-1} Raman shift; Figure 4.4 (b)), relative to the Raman, systematically decreases as the AOI approaches the SPR angle. These results confirm that dramatic Raman enhancement can be attained through the efficient use of SPPs for sample excitation. The quality of the agreement between simulation and experiment also provides further validation that the FDTD simulations yield accurate and meaningful results.

4.4 Quantitative comparison of ATR and side-on excitation for chemical imaging

In the preceding sections, it was shown that ATR illumination enables tunable excitation of evanescent waves and SPPs, and that the TENOM tip can quantitatively

transduce (scatter) these fields into the far-field. These capabilities make the present design well suited to study a variety of near-field optical phenomena, including (i) chemical interrogation of surfaces at super resolutions using TERS, (ii) estimation of Raman enhancement factors, and (iii) direct comparison of side-on and ATR-based excitation schemes. The latter aspect is potentially very important because ATR pump fields can be preferentially channeled into SPPs, which may lead to more "effective" use of pump radiation and larger E-field components along the tip axis, as well as higher SNR due to lower Rayleigh background, i.e., because the sample surface is illuminated in a "dark-field" like mode. Indeed, recent studies of surface-enhanced Raman scattering (SERS) under similar conditions have demonstrated that plasmonic interactions between SPPs and Ag nanoparticles can yield substantial Raman enhancement from analytes positioned in the nanogap between the surface and the nanoparticles [2, 3]. Analogously, by using a single, plasmonically active tip instead of an array of plasmonic nanoparticles, the present system can limit the chemical (Raman) analysis area to a single location, while dynamically measuring interactions between SPPs and the tip.

4.4.1 Sample design

E-beam evaporation was also used to prepare gold-coated glass samples for a variety of TENOM experiments. A 1.5 nm Cr adhesion layer was evaporated onto piranha-cleaned glass cover slips, followed by 40 nm of Au, which optical simulations suggest is the optimal thickness for efficient excitation of SPPs. These samples were further modified for TERS experiments by adding a spatially patterned layer of copper phthalocyanine (CuPc) atop the Au via a three-step process. First, a suspension of silica microspheres (960 nm diameter, Bangs Laboratories) in ethanol was spin-cast onto the gold surface at 2000 rpm, resulting in a colloidal mask of isolated particles and small clusters distributed

randomly across the surface. Next, a 3 nm thick layer of CuPc was slowly deposited (∼0.2 Å/min) onto the exposed Au in a thermal evaporator. Lastly, the sample was sonicated briefly in 18 MΩ water to remove the silica spheres before being dried with N_2. AFM images of the final samples showed a flat, uniform layer of CuPc with a random distribution of "holes", verifying the success of the evaporation and pattern transfer processes.

4.4.2 Chemical imaging

To demonstrate the chemical imaging capabilities of the TENOM instrument, correlated topographic and spectroscopic line scans were performed simultaneously on the spatially patterned samples of CuPc on Au/Cr/glass described above. For these measurements, the tip was engaged on the surface in "attractive" mode (small negative force setpoint) to minimize tip wear and sample damage; topography and Raman spectra (0–3000 cm^{-1} via the side-on objective) were recorded simultaneously along a fast-axis scan line. This procedure was performed twice in approximately the same location (see Figure 4.5), first using ATR illumination (AOI = 45°) and then using side-on illumination via the Raman microscope. In both cases, the optical collection time was 1 sec/pixel (every 40 nm along the scan line) with laser pump powers of 500 μW and 920 μW for ATR and side-on configurations, respectively.

The line scans of Figure 4.5 show that the topography and Raman signatures of CuPc are strongly spatially correlated for both ATR and side-on illumination, with Raman signals from "high" regions (bright areas (1,3)), where CuPc is present, being ∼4–6 times greater than regions without CuPc (dark area (2)). The topo-Raman correlation is particularly good in the latter half of the scans; an abrupt increase in Raman intensity over a single 40 nm step can be seen as the tip climbs out of the "hole" and onto

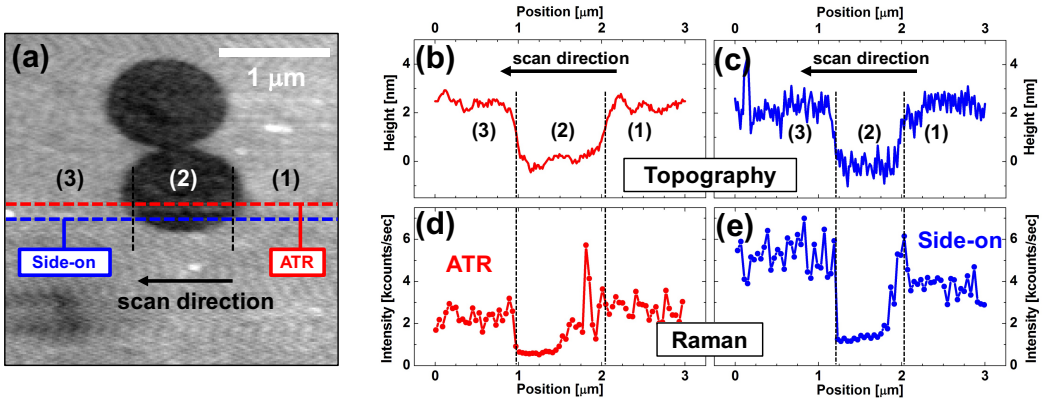

Figure 4.5: **Nanoscale chemical imaging with ATR and side-on illumination geometries.** (a) AFM topography scan of 2-3 nm thick CuPc patterns on Au/Cr (40 nm/1.5 nm) on glass. Bright (high) areas are CuPc on Au/Cr and dark (low) areas are the bare Au/Cr surface. Scan lines where topo and Raman data were collected simultaneously (panels (b)–(e)) are noted by the dashed lines. Topography and Raman data (integrated 1490–1510 cm−1 band of CuPc) for the ATR and side-on illumination geometries along the scan lines in (a) are shown in panels (b,d) and (c,e), respectively. Regions (1,3) and (2) denote areas where CuPc should and should not be present, respectively.

the CuPc layer. The more lazy Raman profile and "noise" at the right side of hole may be due to (i) the tip dragging along a few molecules into the hole, (ii) higher field intensities in the tip-surface gap when the CuPc layer is very thin (on the descent into the hole), and/or (iii) geometric differences or hot spots on different sides of the tip (i.e., ascent is measured with the "left" side of the tip, while descent is measured with the "right" side). Notwithstanding, both the magnitude of the enhanced Raman signal and the lengthscale over which it varies are indicative that tip enhancement is the primary mechanism responsible for the observed results, rather than multiple-scattering events involving the tip shaft (e.g., tip "artifacts") that can negatively affect some TERS measurements [4].

4.4.3 Quantitative comparison of excitation geometries

Enhancement factors (*EF*s) of the aforementioned TER signals for ATR and side-on illumination were estimated using the ON CuPc (region 3) vs. OFF CuPc (region 2) signals from Figure 4.5, as detailed in Figure 4.6. Multiple spectra in regions (3) and (2) were averaged, background subtracted for CCD readout noise, and integrated from 1490–1510 cm^{-1}. *EF*s were then calculated using the following formula:

$$EF = \left(\frac{Signal_{ON} - Signal_{OFF}}{Signal_{OFF}}\right) \times \left(\frac{Area_{far-field}}{Area_{near-field}}\right) \tag{4.2}$$

where the "active" areas of collection for the far-field and near-field signals were estimated at $Area_{far} = 11.3\ \mu m^2$ (1.2 μm × 3.0 μm radii ellipse for the side-on Raman objective, from the experimentally measured point spread function in Chapter 2) and $Area_{near} = 0.005\ \mu m^2$ (40 nm radius circle as an upper bound, i.e., Figure 4.5 shows that the near-field signal changes over distances smaller than the 40 nm pixel size), respectively. Using these values, EF_{ATR} and $EF_{side-on}$ were quite comparable (∼6600 vs. 6800) and similar to values in the few thousands that have been reported previously [5, 6]. Indeed, it is comforting that both methods result in similar enhancements because the ON/OFF signal ratio should only depend on the plasmonic characteristics of the tip-surface system and not the excitation configuration, provided that differences in excitation/collection geometry are taken into account.

We should also mention that variations in surface roughness could potentially affect both the background (OFF) intensity via the SERS effect [7], and the tip-enhanced (ON) signal due to surface geometry modifying plasmonic coupling with the tip [8]. However, we do not believe that roughness significantly influences the *EF*s calculated above because: (i) the surface of the Au substrate was very smooth (roughness of ∼0.3 nm rms) compared to common SERS-active substrates (roughness of order 10 nm rms or

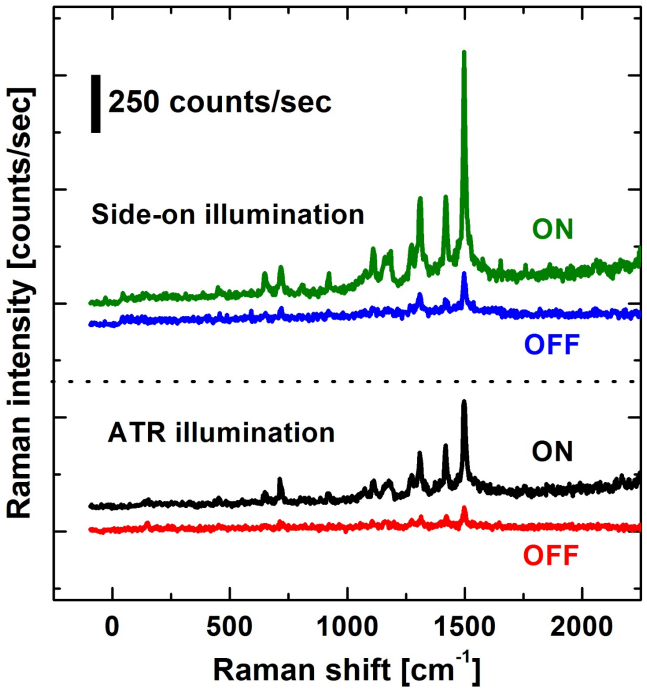

Figure 4.6: **Tip on / tip off Raman comparison for ATR and side-on illumination.** Representative Raman spectra measured in regions (2) and (3) for the line scans shown in Figure 4.5, where the TENOM tip is OFF or ON the CuPc layer, using side-on and ATR illumination of the sample. Overall laser pump powers for these spectra were 920 μW and 500 μW for the side-on and ATR configurations, respectively. Spectra are vertically offset for clarity.

more [9]), (ii) multiple Raman spectra from ON vs. OFF regions were spatially averaged to minimize the effect of local variations on the calculated *EF*s, and (iii) the ATR and side-on data were collected at virtually the same locations across the sample (i.e., nearby scan lines in Figure 4.5 (a)). Therefore, any surface roughness effects on the Raman background signal would be similar for both scans and not affect *EF*s. Furthermore, if surface roughness was indeed contributing to an increased OFF signal due to SERS, then the "true" *EF*s (in the absence of SERS effects) would be *larger* than the conservative estimate of ∼6700 presented above.

Finally, it is noteworthy to compare the absolute Raman signals for the two excitation configurations while considering the dramatic difference in local intensity of pump light

near the tip-surface junction. In the ATR case, 500 μW of pump light was focused into a large elliptical spot (8 μm x 11 μm FWHM); in the side-on configuration, almost twice as much laser power (920 μW) was focused into a much smaller area (1.2 μm x 3.0 μm FWHM). Thus, assuming the tip to be in the middle of the pump spot and neglecting (for now) any other effects (e.g., SPP contributions or tip-light interactions), one would expect the pump intensity in the tip-surface gap to be ∼50x higher in the side-on case. Normalizing the TER intensity (from Figure 4.5, region (3)) to account for this difference, the data suggest that ATR illumination provides an enhancement of more than 20x over side-on illumination when comparing I_{Raman}/I_{pump} (Raman counts/s per $\mu W_{pump}/\mu m^2$) from the active region near the tip apex. This enhancement is a result of the fact that the majority of the pump energy that excited the tip-surface gap in the ATR configuration was supplied *not* by the small amount of light directly incident upon the active volume, but instead by SPPs propagating into the same region. Under the SPR conditions used, the ATR pump light was efficiently coupled into SPPs, which confined the energy to the sample surface and carried it "down" the length of the ATR spot, where it could eventually couple with the tip, increasing the local field at the apex and enhancing Raman scattering. This aspect of ATR-mode TERS may be important when studying optically fragile systems where bleaching or heating are a concern.

In this chapter, we demonstrated several of the TENOM instrument's unique capabilities, which allow us to excite and detect evanescent optical fields and achieve super-resolution chemical interrogation and imaging of surfaces. It was shown that (i) Au-coated AFM tips could be used as optical antennas to quantitatively transduce (scatter) evanescent optical fields near the surface into the far-field for detection, (ii) the resonant characteristics of SPPs, excited in a Kretschmann fashion using the ATR stage, could be qualitatively measured and exploited to enhance Raman scattering, and (iii) SPPs are an effective alternate method for plasmonic excitation of the tip in TERS measurements.

Raman enhancement factors were conservatively estimated at >6500 for both side-on and ATR-based illumination, and spatial resolutions better than 40 nm were achieved. Finally, it was also seen that ATR illumination yielded similar Raman signal levels at lower "effective" pump powers due to SPP-mediated delivery of additional optical energy into the tip-surface gap region. In the next chapter, we will apply the TENOM instrument to fundamental studies of the complex tip-surface optical interactions that occur at small separation distances, with emphasis on how these phenomena contribute to strong local fields and large Raman enhancement.

References

[1] A. L. Mattheyses and D. Axelrod, "Direct measurement of the evanescent field profile produced by objective-based total internal reflection fluorescence," *Journal of Biomedical Optics*, vol. 11, no. 1, pp. 014006–014006, 2006.

[2] H. Chiba, H. Suzuki, and M. Futamata, "Highly sensitive Raman spectroscopy using a gap mode plasmon under an attenuated total reflection geometry," *Vibrational Spectroscopy*, vol. 73, pp. 19–23, 2014.

[3] K. Akai, C. Iida, and M. Futamata, "Gap mode Raman spectroscopy under attenuated total reflection geometry," *Journal of Optics*, vol. 17, no. 11, p. 114008, 2015.

[4] R. Ramos and M. Gordon, "Near-field artifacts in tip-enhanced Raman spectroscopy," *Applied Physics Letters*, vol. 100, no. 21, p. 213111, 2012.

[5] R. Ramos and M. Gordon, "Reflection-mode, confocal, tip-enhanced raman spectroscopy system for scanning chemical microscopy of surfaces," *Review of Scientific Instruments*, vol. 83, no. 9, p. 093706, 2012.

[6] S. Kawata and V. M. Shalaev, *Tip Enhancement*. Elsevier B. V., 2007.

[7] Y. Zhao, X. Liu, D. Y. Lei, and Y. Chai, "Effects of surface roughness of Ag thin films on surface-enhanced Raman spectroscopy of graphene: spatial nonlocality and physisorption strain," *Nanoscale*, vol. 6, no. 3, pp. 1311–1317, 2014.

[8] W. Zhang, X. Cui, B.-S. Yeo, T. Schmid, C. Hafner, and R. Zenobi, "Nanoscale roughness on metal surfaces can increase tip-enhanced Raman scattering by an order of magnitude," *Nano Letters*, vol. 7, no. 5, pp. 1401–1405, 2007.

[9] R. Koh, S. Hayashi, and K. Yamamoto, "Optimum surface roughness for surface enhanced Raman scattering," *Solid State Communications*, vol. 64, no. 3, pp. 375–378, 1987.

Chapter 5

Direct detection of gap plasmon resonances using the TENOM instrument

5.1 Introduction

TENOM allows detailed structural and chemical interrogation and imaging of materials, i.e., via photoluminescence [1–3] and/or vibrational (e.g., Raman [4–10] and IR [11–13]) spectroscopies at the nanoscale, through excitation, enhancement, and/or detection of optical interactions between an optical antenna tip and a surface at sub-wavelength (super-resolution) spatial dimensions. These methods are heavily influenced by the optical properties of the 'coupled' tip-surface system [4, 14]; local field intensity, wavelength and polarization-dependent plasmonic coupling with the surface and/or tip, and spectral overlap of plasmonic modes with excitations and emissions of surface moieties can all affect detection limit, (Raman) enhancement factors, oscillator strengths, radiative/non-radiative transition rates, and imaging resolution. Moreover, at short (nm-scale) dis-

tances, mutual interactions between the metallic TENOM tip and surface [15–18] can give rise to strongly-coupled optical modes, known as gap plasmons [19–23], whose resonance (frequency response) is a strong function of the system geometry, and can be tuned by changing the tip-surface spacing. The optical behavior of these gap modes is a topic of current experimental and theoretical research, and they can potentially be harnessed to create and manipulate extremely intense optical fields at nm-scale dimensions for photonic devices, chemical sensing, and materials characterization applications [4, 14, 24].

In this chapter, we show how the TENOM instrument's unique design can be used to achieve exceptional sensitivity toward the tip's interactions with the optical near-field above the sample surface. Through careful measurements of surface reflectance and elastic scattering by the tip, the instrument is able to detect changes in the plasmonic response of the tip-surface system, namely the resonant excitation of gap plasmon modes at small tip-surface distances. FDTD optical simulations are used to help elucidate the primary mechanisms that influence the optical behavior of this plasmonic mode, and spectroscopic measurements are used to demonstrate its effect on Raman and fluorescence enhancement. Finally, we discuss how these results can be applied to improve the design of future TENOM experiments.

5.2 Experimental methods

5.2.1 Instrument modifications

The TENOM instrument configuration used for the present study is shown schematically in Figure 5.1 (a) and (b). This design differs from that presented in Chapter 4 in two ways. First, an electrical circuit was added to enable direct detection of tip-surface

electrical contact in a Boolean manner by applying a small bias (∼50 mV) to the tip and monitoring the tip-surface voltage (V_{t-s}). Upon conductive contact, the circuit (see Figure 5.1 (b)) acts like a simple voltage divider; because of the small resistance of the tip-surface junction relative to the 300 MΩ resistor in series, V_{t-s} effectively drops to zero. As will be discussed below, electrical contact between the tip and surface has important consequences regarding the optical response of the system; thus, the ability to unambiguously detect this event is extremely important. The second instrument modification involved reconfiguring the Raman microscope for light collection only (no side-on illumination). Light collected by the microscope's objective exits the rear aperture as a collimated beam and follows one of two paths, depending on the wavelength. Elastically scattered light (i.e., $\lambda = 633$ nm) reflects off a dichroic mirror and is coupled into a multimode optical fiber (600 μm core); light exiting the fiber is focused onto a silicon photodetector, which outputs a voltage proportional to the intensity of the Rayleigh scattered light. Wavelengths longer than 633 nm pass through the dichroic mirror, as well as a Raman filter that further attenuates elastic scattering, and the light is then focused into a 50 μm core optical fiber that functions as a confocal pinhole to reject out-of-focus light. Light exiting this fiber is f-matched to the monochromator, wavelength dispersed, and detected with an LN2-cooled CCD.

5.2.2 Approach curve measurements

The primary goals of this work were to (i) elucidate the mechanisms by which the TENOM tip interacts with evanescent fields near the sample surface, (ii) demonstrate the TENOM instrument's ability to detect resonant gap plasmon excitation, and (iii) study the influence of gap plasmon modes on light emission and Raman enhancements. To achieve these goals, various optical (ATR reference and reflectance; Rayleigh scattering

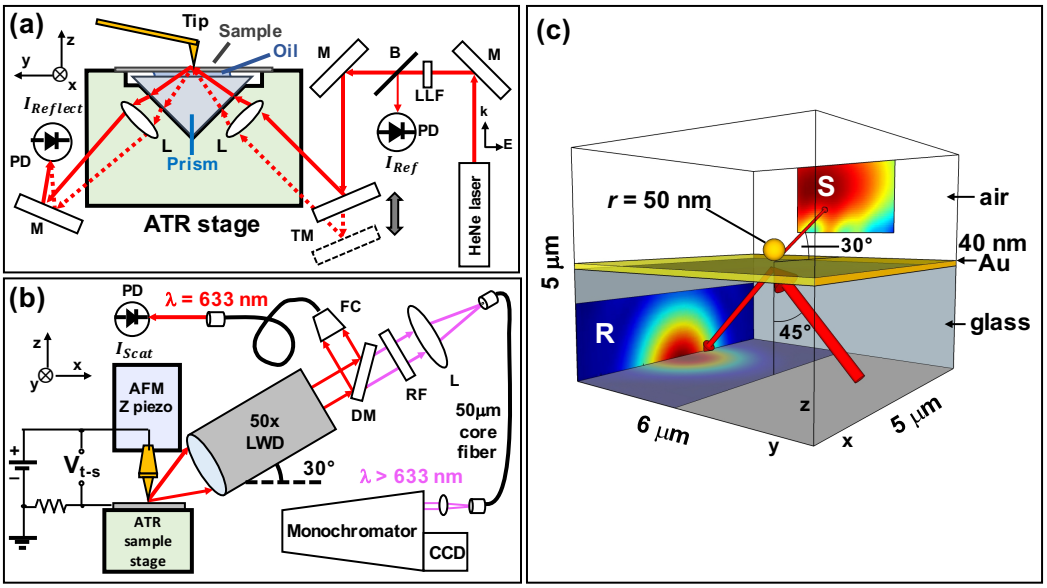

Figure 5.1: **Experimental apparatus and FDTD simulation setup.** (a) Detailed schematic of the ATR system's beam path and critical optical elements (B = 92:8 beamsplitter, L = lens, LLF = laser line filter, M = mirror, PD = photodiode, TM = translating mirror). Dashed and solid lines represent two alternate beam paths with different AOI determined by the position of the translating mirror. (b) Schematic of the combined TENOM system, including tip-sample voltage (V_{t-s}) circuit and Raman microscope, which collects elastic (red) and inelastic (magenta) scattering from the tip and measures each by a separate pathway. Optical elements include: CCD = charge-coupled device, DM = dichroic mirror, FC = fiber coupler, L = lens, LWD = long working distance objective, PD = photodiode, RF = Raman filter. (c) Depiction of the FDTD simulation setup consisting of a Au sphere above a "sample" of Au on glass. Transmission monitors in the lower and upper half-spaces were oriented and sized to approximate the experimental apertures for collection of reflected (R) and scattered (S) light, respectively.

from the tip via the side-on Raman microscope) and electrical (T–B cantilever deflection and V_{t-s} indicating tip-surface "contact") signals were measured as a function of tip-surface separation (z) during a tip "approach" curve. Approach curves were taken in two modes: (i) without optical spectra, where tip deflection, ATR signals, and electrical data were collected continuously, yielding smooth run-in profiles (Figure 5.2); and (ii) with optical spectra, where the tip was moved in discrete steps with spectra acquired over a 0.5–1 s collection interval at each tip-surface distance (Figures 5.4 and 5.5). For

runs without spectra (where piezo creep and thermal drift were minimal), tip-surface separation was quantified by setting the $z = 0$ contact point to be the point of zero cantilever deflection ($F_N = 0$) after snap-on, along with an experimentally determined z-piezo distance-voltage gain factor (nm/V), obtained by scanning a step-height calibration standard. For runs with spectra (where piezo creep and thermal drift can lead to errors), tip-surface distance was evaluated by shifting and scaling the z-axis to match the scattering and ATR reflection profiles of the discrete step run-in to the trend seen for a continuous run-in measured immediately before.

5.2.3 FDTD optical simulations

Approach curves provide a wealth of insight regarding the nuanced interactions between the TENOM tip and the optical near-field. These interactions were investigated theoretically using FDTD optical simulations (Lumerical) in an effort to qualitatively reproduce empirical trends and gain additional insight into the optical response of the system. Optical modeling was performed on a simplified analog of the experimental system, whose simulation volume is shown schematically in Figure 5.1 (c). The 3D model contains a Au sphere of radius 50 nm positioned at varying distances above a "sample" consisting of 40 nm of Au and 1.5 nm of Cr atop a semi-infinite slab of glass with refractive index $n = 1.515$. A polychromatic (600–800 nm) light source with a Gaussian spatial distribution is generated in the glass and propagates upward at a 45°AOI (relative to the surface), converging to a focused spot (FWHM = 1 μm) centered at the sphere-surface axis. Light that reflects off the surface passes through two monitors positioned along the simulation boundary that measure the wavelength-dependent transmission as a percentage of the input power. Similarly, light scattered by the sphere into the air above the sample is detected with another transmission monitor whose size and position were

chosen to mirror the collection geometry (i.e., NA and angle) of the Raman microscope objective in the experimental system.

The FDTD model and experimental system have three main differences. First, simulations use a Au sphere instead of a rounded cone, which would more faithfully represent the AFM tip. This substitution dramatically simplifies the behavior of the system, as it eliminates the spurious scattering events caused by the tip shaft that can obscure or overwhelm the desired optical response of the sphere-surface system (i.e., the gap plasmon). Second, in contrast to the fixed wavelength of the experimental system, the FDTD simulations use a broadband source, which can be used to investigate the frequency-dependent response of the gap plasmon and, more importantly, how it changes with sphere-surface distance. Lastly, practical considerations, such as computational expense and file size, restrict the size of the simulation volume, necessitating the use of a smaller focal spot (1 μm) than that of the ATR pump spot in the TENOM system ($\sim$8 μm). As a result, the convergence angle of the beam (i.e., the range of AOIs incident upon the sample surface) is broader in the simulations. Although this has several direct effects on important phenomena in the system, such as SPP excitation efficiency and the magnitude of the sphere-light coupling, we have confirmed (via larger simulations) that its effect on the qualitative trends of interest is minimal.

5.3 Results and discussion

5.3.1 "Long-range" (z >15 nm) approach curve trends

Figure 5.2 shows the results of a typical approach curve, in which the sample reflectance (R) and far-field elastic scattering (S) are plotted as a function of the tip-surface distance (z). Focusing first on the long-range (z >100 nm) behavior, the reflectance pro-

file demonstrates an exponential z-dependence and can be accurately fit with a simple model (solid black line): $\Delta R(z) = R(z) - R(\infty) = A \exp(-z/d)$. As shown in previously reported measurements of evanescent field profiles above a glass-air interface [10], the fit parameter d provides a quantitative measure of the characteristic decay length of the evanescent field above the sample surface. In this case, the observed value of ∼200 nm compares reasonably well with the field profile expected for SPPs at a Au-air interface [16, 25], suggesting that the tip's influence on the reflectance signal is proportional to the local strength of the SPP field. The long-range scattering profile is roughly the inverse of the reflectance, increasing as z decreases; however, it is governed by a slightly more complex z-dependence. Though the underlying trend still appears to be exponential, it is convolved by an additional oscillatory behavior that is reminiscent of interference effects, which have been shown to influence the radiative efficiency of a dipole emitter near a mirror [26, 27]. Considering that the Au sample surface is partially reflective and that the observed scattering signal originates—at least in part—from a radiating dipolar mode of the tip apex, it is not surprising that the scattering profile shows similar interference artifacts. Thus, to fit the profile of the scattering data, the following model was used, which includes an oscillatory term that is fixed at the wavelength of the excitation source (633 nm):

$$S(z) = \left[A + B \sin\left(2\pi \frac{z}{633 \text{ nm}} + \phi\right)\right] \times \exp\left(\frac{-z}{d}\right) \tag{5.1}$$

where A, B and ϕ are arbitrary constants and d is the same decay length determined from fitting the reflectance profile. This model (solid blue line in Figure 5.2 (a)) matches the scattering profile well, suggesting, as in Ref. [27], that the oscillatory behavior of the scattering profile can indeed be attributed to interference effects.

For tip-surface distances less than ∼100 nm, the scattering profile begins to deviate strongly from the simple model presented above, and at tip-surface distances smaller

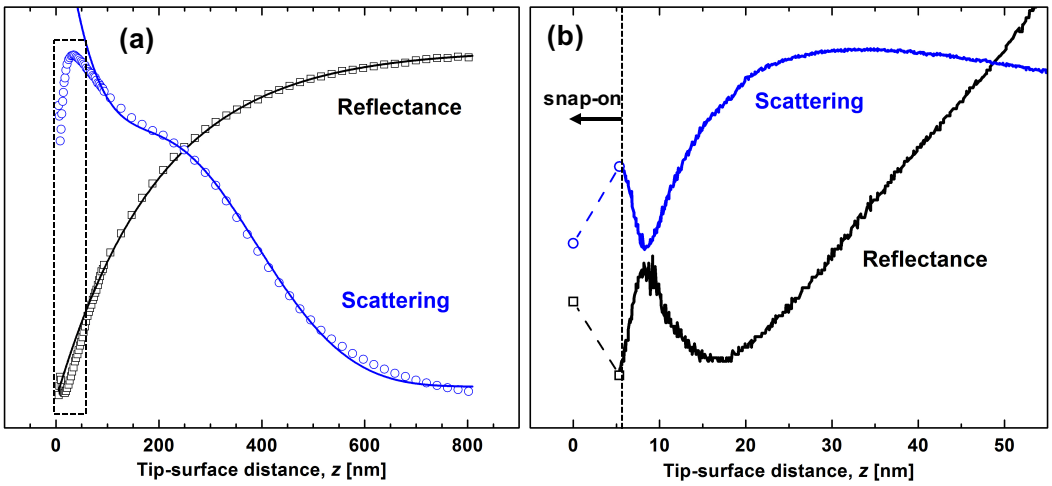

Figure 5.2: **Long- and short-range approach curve trends.** (a) Experimental profiles (points) and fits (solid lines) of reflectance and elastic scattering as a function of tip-surface distance, measured above a sample of Au/Cr (40/1.5 nm) on glass at AOI = 45°. (b) Rescaled plot of data from dashed box in (a), highlighting behavior at small z. Discontinuous jump in data at $z \approx 5$ nm is due to "snap-on", at which point the tip is pulled into mechanical contact with the surface. Note: Only 1 in 20 data points are shown in panel (a) to ensure visibility of fit lines.

than ∼50 nm, S drops sharply and no longer mirrors the inverse trend of the reflectance. To understand the origin of this abrupt change, it is helpful to consider the mechanisms by which light is reflected and scattered in the tip-surface system. In the absence of a tip, light incident upon the Au-air interface (from below at 45°) generates an evanescent field in the air above the surface. A large fraction of the energy in this evanescent field excites SPPs at the interface and the remainder is specularly reflected back into the glass substrate, where it can be measured by the ATR system. Because SPPs are evanescent, no optical power can radiate into the air above the interface in such a system (i.e., $S = 0$). When a metallic tip is introduced into this system, it can interact with the evanescent fields of the indent beam and the SPPs; this influences the surface reflectance and far-field scattering intensity by way of the following two-step process. First, the oscillating evanescent field excites a dipole in the tip; because of the associated energy transfer away from the evanescent field, the reflectance of the interface drops. As evidenced by

the observed exponential trend in ΔR, the magnitude of this energy transfer process is proportional to the local field strength. The second step of this process involves the decay of the tip dipole into all available modes. When the tip is far from the Au surface (z >100 nm), the dominant decay pathway is via radiation of photons into the surrounding air [26, 27]. However, when the tip is close to the surface, a variety of non-radiative decay pathways, such as excitation of surface plasmons and lossy surfaces waves (LSWs), are also possible. The probability of dipole decay into each of these different optical modes is a strong function of the tip-surface distance and tends to favor non-radiative modes for z <100 nm. Thus, returning to the approach curves in Figure 5.2 (a), we attribute the observed drop in scattering within the last 50–100 nm to the preferential decay of the tip dipole into non-radiative modes. The mechanism described above, which is fully consistent with the scattering and reflectance behavior presented, provides a useful framework to understand and explain near-field tip-surface interactions, as well as the complex and nuanced behavior of the system at small z.

5.3.2 Short-range ($z < 15$ nm) approach curve trends

Figure 5.2 (b) shows the same approach data as in panel (a) but is rescaled to highlight the unique behavior at tip-surface distances below ∼15 nm. The reflectance signal abruptly deviates from its downward exponential trend and goes through a sharp maximum (FWHM < 5 nm) at a tip-surface distance of ∼9 nm. Correspondingly, the scattering signal shows the inverse behavior, with a local minimum at the same position. As the tip-surface distance is decreased further, attractive forces inevitably pull the tip down into mechanical contact with the surface, an event referred to as "snap-on", at which point the reflectance and scattering signals both undergo an abrupt change. As will be discussed below, these trends provide valuable insight into tip-induced changes

in the optical environment near the surface and correlate with changes in the spectral emission behavior of the system, which is relevant for tip-enhanced spectroscopies, such as TERS.

To appreciate the significance of the short-range approach curve behavior, it is first important to consider how tip-surface interactions in this distance regime modify the scattering mechanism discussed in the previous section. When the tip is near the Au sample surface, the dipole field of the tip apex induces a mirror dipole in the substrate; if the tip is sufficiently close, the presence of this induced dipole significantly alters the optical response of the tip (i.e., the resonance properties of its localized surface plasmon, or LSP, modes). In this so-called strong-coupling regime ($z \lesssim 30$ nm [16]), it is no longer appropriate to consider the tip and surface as independent objects interacting via photons (as in the case of the two-step scattering process above); one must instead consider the optical response (i.e., frequency-dependent excitation efficiency and preferential decay pathways) of the combined hybrid tip-surface system. The rapid changes observed in approach curves immediately before snap-on are suggestive of the emergence and disappearance of a resonant tip-surface mode that dramatically redistributes the optical energy of the system. Because the phenomenon occurs over such a narrow z range, we hypothesize that this behavior is due to resonant excitation of a gap plasmon, which is a hybrid plasmonic mode of the strongly-coupled tip-surface system, whose resonance properties are largely dictated by geometry. As the tip approaches the surface, the resonant frequency of the gap plasmon, $\omega_{gap}(z)$, red-shifts relative to that of the tip's free-space LSP mode. When ω_{gap} matches the frequency of the excitation source, energy is transferred very efficiently into the gap plasmon, which consequently alters the distribution of optical power in the various modes of the system. Furthermore, the resonant behavior of the gap plasmon also influences the favored pathways for decay of the associated dipole because of the dramatic change in its scattering cross-section.

The combination of these effects can help explain the observed approach curve behavior in the following way, beginning with the increase in reflectance. When the tip-surface distance is at or near the position corresponding to $\omega_{gap}(z) = \omega_{pump}$, the evanescent pump field efficiently excites the gap plasmon mode, which then radiates its energy. Because the orientation of the gap plasmon dipole is normal to the Au surface, the primary wavevector component of this radiation is in the plane of the surface. Due to the necessary wavevector matching condition, optical fields in the glass substrate below gain a large normal wavevector component (as per Snell's Law), which leads to propagation of light into the glass at angles equal to and greater than the critical angle. A portion of this light is collected and detected by the ATR system, where it contributes to an observed increase in the reflectance signal. Several important caveats should be noted at this point in the discussion. First, this increase in the reflectance signal is not actually caused by an abrupt change in the specular reflectance of the sample interface, but is instead an artifact of a separate phenomenon to which the ATR system is sensitive. Second, resonant excitation of the gap mode is not required to facilitate the optical pathway described above; rather, the efficiency of resonant energy transfer into the gap plasmon increases the fraction of the total optical power that is scattered by this pathway. This second point is particularly relevant in describing the qualitative behavior of the scattering profile.

Given the efficiency of the gap plasmon's excitation and radiation, one might reasonably expect that the scattering profile should exhibit a peak during resonant gap plasmon excitation; however, the opposite is observed. To explain this trend, it is helpful to first consider the two main optical events that contribute to the scattering signal: (i) dipole radiation from the tip apex (or the gap plasmon at small z), and (ii) scattering of the evanescent field by the tip shaft [28]. When the gap plasmon is resonant with the excitation source, we have seen (via the reflectance signal) that optical power is efficiently transferred into this dipole mode and subsequently radiated, presumably into both the

glass substrate and the surrounding air, where it should contribute to an increase in the scattering signal. However, by the conservation of energy, resonant excitation of the gap mode must deplete energy from other optical modes of the system, including the scattering pathways of the tip shaft; this energy loss should, therefore, contribute to a decrease in the scattering signal. Because the net result of these competing effects is an observed decrease in scattering during resonant gap excitation, we infer that the dominant contribution to the scattering signal at small z is due to interactions between the evanescent near-field and the tip shaft and not photon emission from the gap plasmon.

Considering the sensitivity of the reflectance and scattering signals to changes in the plasmonic resonance of the tip-surface system, the discontinuous jump observed in both signals after snap-on is not surprising. The plasmonic behavior of nanostructures generally relies on the accumulation of electron density at a metal-dielectric boundary; changing this boundary condition dramatically influences the optical response of the plasmon modes. Thus, when the tip is pulled into electrically-conductive contact with the Au surface (as confirmed by monitoring V_{t-s}), the fundamental plasmon modes of the tip-surface system change in response. As with the emergence of the gap plasmon resonance, this change affects the distribution of optical energy in the system in ways that are observable through the scattering and reflectance measurements.

5.3.3 FDTD results

Although the mechanisms described above constitute a framework for explaining the qualitative behavior of the reflectance and scattering profiles, they do not give detailed information about the effect of tip-surface distance on the optical properties of the gap plasmon. To investigate these phenomena more rigorously, FDTD simulations were used to model the optical response of a simplified version of the experimental system. As de-

scribed in Section 5.2.3, the FDTD models consisted of a Au sphere positioned at various distances away from a substrate of Au on glass. A suite of simulations was performed to assess the wavelength-dependent reflectance and scattering of this system for five sphere-surface distances, ranging from 2 to 10 nm; the results of these simulations are shown in Figure 5.3. The wavelength dependence of the sphere-surface scattering (Figure 5.3 (a)) clearly demonstrates the presence of an optical mode that preferentially increases scattering from a narrow wavelength range. As the sphere-surface distance decreases, this wavelength range red-shifts noticeably, suggesting that the scattering phenomenon is due to the resonance of the hybrid sphere-surface optical system (i.e., the gap plasmon). Similarly, the change in wavelength-dependent reflectance, relative to the no-sphere simulation (Figure 5.3 (b)), shows the emergence of a shoulder at approximately the same wavelength position as the peak in scattering; like the scattering event, this shoulder clearly red-shifts and becomes more prominent with decreasing sphere-surface distance. By extracting the distance-dependent scattering and reflectance behavior at a fixed wavelength (630 nm) near that of the experimental excitation source (Figure 5.3 (c)), we can directly compare these results to the small-z approach curves (Figure 5.2 (b)) discussed in the previous section. As can be seen, the tip-surface distance dependences of the experimental and simulated reflectance data are qualitatively similar, with both exhibiting a maximum, presumably when the frequency of the gap plasmon resonance matches that of the excitation source. However, the simulated scattering profile, which also exhibits a maximum, shows the inverse trend of the experimental results; this can be explained via the scattering mechanisms presented in Section 5.3.2. The simplified FDTD model of the system does not include a tip shaft because the scattering effects associated with it tend to obscure and overwhelm the resonance events of interest. As is consistent with the relative scattering contributions of the shaft and the gap plasmon discussed above, it is, therefore, expected that these simulations should fail to qualitatively capture the

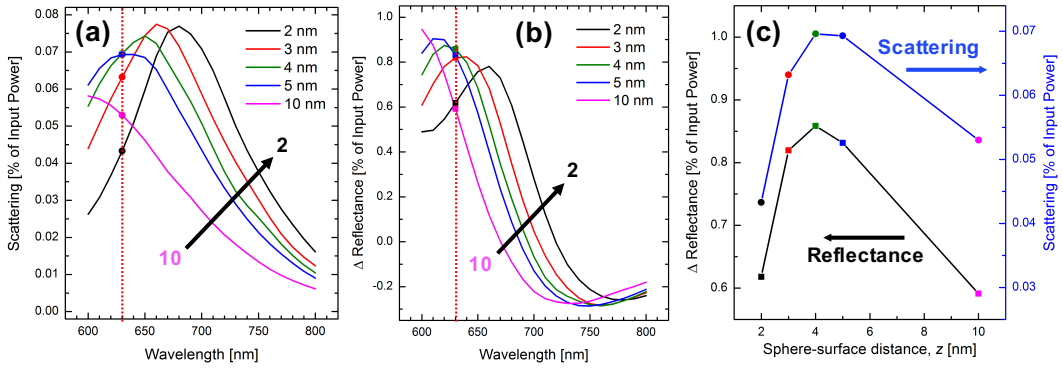

Figure 5.3: **FDTD simulation results of gap plasmon resonances.** (a) Wavelength dependence of scattering from sphere-surface system for five separation distances ranging from 2 to 10 nm. (b) Wavelength-dependent reflectance change, relative to no-sphere simulation, for the same simulations as in (a). (c) Scattering and reflectance change at 630 nm excitation (dashed lines in (a) and (b)) as a function of sphere-surface distance. These results show the emergence and shift in resonance of the gap plasmon mode; the qualitative behavior of the reflectance change matches particularly well with experimentally observed trends.

scattering behavior of the experimental system, as they are only sensitive to the relatively small contribution of the gap plasmon.

In addition to this inconsistency between the experimental and simulated scattering profiles, the FDTD results appear to exhibit several other contradictions that should be clarified before continuing our discussion. First, the simulations suggest that resonant excitation of the gap mode results in an increase in both reflectance and scattering, which seems to contradict the necessary energy balance around the system. This can be reconciled, however, by remembering that the sphere and substrate are composed of Au, which is a lossy material. Thus, when performing a photon balance around the simulation volume, input-to-output power ratio is far from unity and is lowest for wavelengths that most efficiently transfer their power into inherently lossy plasmon modes. Therefore, the simultaneous increase in reflectance and scattering associated with resonant gap plasmon excitation can be attributed to an increase in the efficiency of the plasmon's radiative decay into the substrate and air, respectively, and a corresponding decrease

in the efficiency of its decay into lossy, non-radiative modes in the substrate. Another obvious discrepancy between the experimental and simulated results is the tip-surface position at which the gap plasmon is resonantly excited. This is largely due to the fact that the resonance condition depends strongly on the geometry of the tip-surface system, including not only the tip-surface distance but also the apex radius and shaft geometry. Since the simulations were performed with a fixed sphere radius (not necessarily that of the real tip apex) and no tip shaft, it is expected that both the resonant position and distance scaling of the gap plasmon should be quantitatively different from experiments.

Despite these issues, the qualitative behavior of the simulated sphere-surface system is still consistent with the experimental data and the hypotheses proposed in previous sections. Furthermore, it reveals an important characteristic of the gap plasmon to which the approach curves in Figure 5.2 are not sensitive: the FDTD results show that the air-side scattering efficiency of the gap plasmon increases dramatically near its resonant frequency. This property has important consequences regarding the spectral response of the system in the small-z regime.

5.3.4 Spectral behavior of the tip-surface gap

The wavelength-dependent optical response of the gap plasmon is particularly relevant to spectroscopic TENOM techniques, such as tip-enhanced Raman spectroscopy (TERS), because it may provide an efficient pathway for light emission at frequencies near that of the gap plasmon resonance. This enhanced resonant emission can lead to a considerable increase in signal strength, which can, in turn, improve the sensitivity and practicality of traditionally signal-starved near-field optical techniques [29]. To this end, the spectral response of the gap plasmon was studied as a function of tip-surface distance by performing approach curves while simultaneously using the side-on Raman

microscope to collect and analyze the light emitted from the tip-surface gap. The results of one such experiment are shown in Figure 5.4, where panel (a) shows the familiar reflectance and scattering profiles, as well as the two tip-monitoring signals, T–B and V_{t-s}, used to detect snap-on. Panel (b) shows five optical spectra (after removal of the baseline spectrum shown) taken at the tip positions marked by vertical lines in panel (a). These spectra clearly display a Lorentzian photoluminescence (PL) band that emerges at a tip-surface distance near the position of optimal gap plasmon excitation (i.e., the peak in reflectance) and red-shifts with decreasing z. Furthermore, it was observed that this spectral feature disappeared upon snap-on (not shown).

Because of the shape and z-dependence of the PL band, we hypothesize that the observed spectral behavior is an indication of a resonant gap plasmon mode that locally modifies the photoluminescence characteristics of the Au tip and substrate via the following mechanism (See Ref. [30]). Weak photoluminescence (quantum efficiency $\sim 10^{-10}$) from Au is a well-understood phenomenon in which holes in the d-band radiatively recombine with electrons in the sp-band [31]; this results in a broad emission band like that observed in the baseline spectrum in Figure 5.4 (b), which was measured in the absence of the tip. As the tip approaches the surface, the emergence of a resonant gap plasmon mode influences this PL process in two ways. First, resonant excitation of the gap plasmon (i.e., when $\omega_{gap} = \omega_{pump}$) increases the rate of electron-hole pair generation, which increases the quantum efficiency, and hence the intensity, of the PL emission. Second, the frequency response of the gap plasmon modifies the energy-dependent emission efficiency, preferentially enhancing PL at wavelengths that overlap with the resonance of the gap plasmon. Bearing this mechanism in mind, one would predict the z-dependent PL emission to exhibit three qualitative trends: (i) an enhanced PL band should emerge when the gap plasmon is resonantly excited, presumably near the peak in sample reflectance (R); (ii) the PL band should red-shift with decreasing tip-surface distance, mirroring the shift

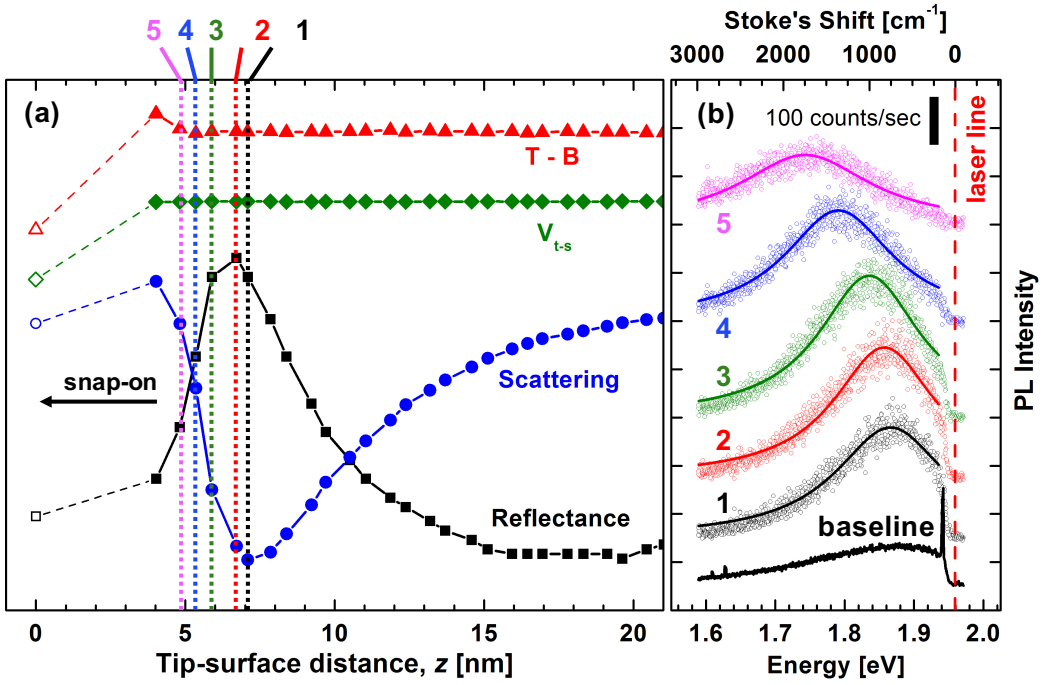

Figure 5.4: **Photoluminescence enhancement from the gap plasmon.** (a) Experimental reflectance and scattering profiles measured concurrently with optical spectra (one at each tip-surface distance). Also shown are the "top minus bottom" (T–B) and tip-surface voltage (V_{t-s}) signals used for tip monitoring (i.e., snap-on detection). (b) Five optical spectra (points) taken at the corresponding tip-surface distances shown by the numbered vertical lines in (a) and fit with Lorentzian profiles (solid lines). The baseline spectrum shown, which demonstrates the weak photoluminescence from the Au substrate, was subtracted from each of the spectra (the peak at ~1.94 eV in the baseline spectrum is an undesired emission line from the HeNe laser). Spectra are vertically offset for clarity but were not rescaled; the collection time was 1 second.

in the gap plasmon resonance; and (iii) the intensity of the PL band should decrease as the overlap between the pump frequency and the gap plasmon resonance decreases (i.e., as the electron-hole pair generation rate decreases). Indeed, the data shown in Figure 5.4 clearly demonstrate the predicted behavior. This not only validates the proposed mechanism, but it also reveals that the features in the R and S profiles correspond with the resonant excitation of the gap plasmon, confirming the central hypothesis of this chapter.

As mentioned previously, the spectral behavior of the gap plasmon is particularly

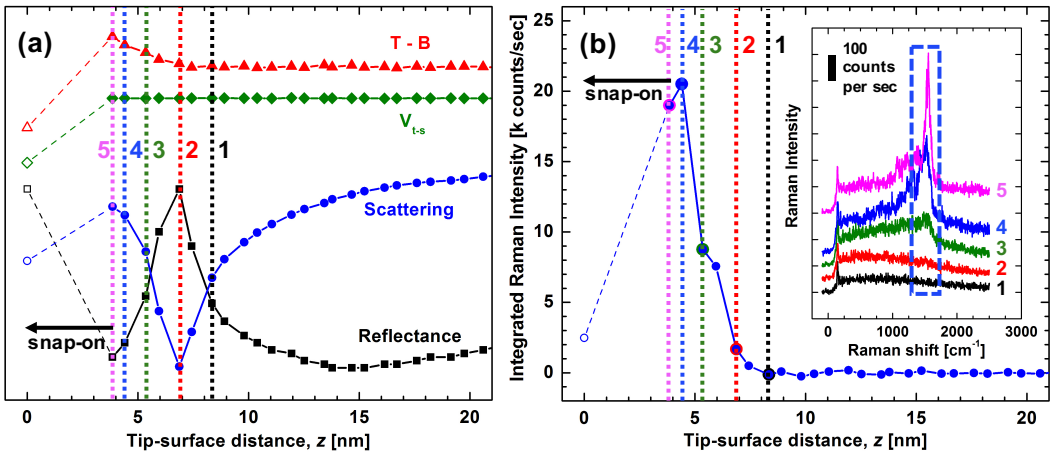

Figure 5.5: **Raman enhancement from the gap plasmon.** (a) Experimental reflectance and scattering profiles, as well as T–B and V_{t-s}, measured concurrently with optical spectra (one at each tip-surface distance). (b, inset) Five optical spectra (no baseline subtraction), taken at the corresponding tip-surface distances shown by the numbered vertical lines, demonstrating the emergence of a broad Raman feature near 1500 cm^{-1} for z $\lesssim$ 5 nm. (b) Integrated intensity (after baseline subtraction) of each Raman spectrum (integration range = 1400–1600 cm^{-1}) as a function of tip–surface distance. The Raman approach profile shows an increase in Raman intensity as the gap resonance overlaps with the primary Raman line, as well as a sharp drop in Raman intensity upon snap-on. As in Figure 5.4, the peak at ~200 cm^{-1} is from the HeNe laser, spectra are vertically offset for clarity but were not rescaled, and the collection time was 1 second.

relevant to TERS because of the potential to achieve dramatic signal gain by tuning the plasmon resonance to match the frequency of a desired Raman transition [29]; this is demonstrated in Figure 5.5. Panel (a) shows the reflectance and scattering profiles alongside the two tip-monitoring signals (analogously to Figure 5.4), and the inset of panel (b) shows five optical spectra taken at tip positions denoted by the numbered vertical lines. After baseline removal, the integrated spectral intensity from 1400–1600 cm^{-1} was calculated for all spectra and plotted in panel (b) as a function of tip-surface distance. The features observed in these spectra are likely due to Raman scattering from small amounts of carbonaceous contamination that adsorbed on the surface during exposure to ambient conditions. Although the features are poorly defined and uncharacteristically broad for Raman bands, their wavenumber position and line shape are consistent with

previously reported examples of tip-enhanced Raman scattering from undefined organic contamination [32]. Unfortunately, the lack of control over the uniformity and density of analyte coverage on the surface makes rigorous quantitative evaluation of these results a challenge; however, the qualitative behavior of the system shows a clear and reproducible trend.

As the tip-surface distance decreases and the gap plasmon resonance red-shifts toward the frequency of the primary Raman band ($\sim$1500 cm^{-1}), the intensity of the Raman scattering increases sharply. Of course, this is due in part to the increase in the intensity of the field in the tip-surface gap, which increases monotonically as the tip approaches the surface, irrespective of the gap plasmon resonance. However, when the tip snaps into contact with the surface and the tip-surface distance is at a minimum, the Raman intensity drops abruptly. This suggests that the optical characteristics of the gap plasmon, particularly the overlap of its resonance with the frequency of the Raman emission, may contribute to a significant enhancement in Raman scattering. Furthermore, the sharp decrease in Raman scattering upon snap-on, presumably due to a discontinuous change in the plasmonic behavior of the system, implies that careful tuning of the tip-surface distance in the gap plasmon regime can yield much stronger Raman enhancements than are achievable though common contact-mode TERS methods.

References

[1] E. J. Sánchez, L. Novotny, and X. S. Xie, "Near-field fluorescence microscopy based on two-photon excitation with metal tips," *Physical Review Letters*, vol. 82, no. 20, p. 4014, 1999.

[2] A. Hartschuh, H. Qian, A. J. Meixner, N. Anderson, and L. Novotny, "Nanoscale optical imaging of excitons in single-walled carbon nanotubes," *Nano Letters*, vol. 5, no. 11, pp. 2310–2313, 2005.

[3] P. Anger, P. Bharadwaj, and L. Novotny, "Enhancement and quenching of single-molecule fluorescence," *Physical Review Letters*, vol. 96, no. 11, p. 113002, 2006.

[4] N. Mauser and A. Hartschuh, "Tip-enhanced near-field optical microscopy," *Chemical Society Reviews*, vol. 43, no. 4, pp. 1248–1262, 2014.

[5] S. Kawata and V. M. Shalaev, *Tip Enhancement*. Elsevier B. V., 2007.

[6] A. Hartschuh, "Tip-enhanced optical spectroscopy," *Phil. Trans. R. Soc. A*, vol. 362, no. 1817, pp. 807–819, 2004.

[7] R. M. Stöckle, Y. D. Suh, V. Deckert, and R. Zenobi, "Nanoscale chemical analysis by tip-enhanced Raman spectroscopy," *Chemical Physics Letters*, vol. 318, no. 1, pp. 131–136, 2000.

[8] N. Hayazawa, Y. Inouye, Z. Sekkat, and S. Kawata, "Near-field Raman scattering enhanced by a metallized tip," *Chemical Physics Letters*, vol. 335, no. 5, pp. 369–374, 2001.

[9] A. Hartschuh, E. J. Sánchez, X. S. Xie, and L. Novotny, "High-resolution near-field Raman microscopy of single-walled carbon nanotubes," *Physical Review Letters*, vol. 90, no. 9, p. 095503, 2003.

[10] A. Heilman and M. Gordon, "Tip-enhanced near-field optical microscope with side-on and ATR-mode sample excitation for super-resolution Raman imaging of surfaces," *Journal of Applied Physics*, vol. 119, no. 22, p. 223103, 2016.

[11] B. Knoll and F. Keilmann, "Near-field probing of vibrational absorption for chemical microscopy," *Nature*, vol. 399, no. 6732, pp. 134–137, 1999.

[12] A. Dazzi, C. B. Prater, Q. Hu, D. B. Chase, J. F. Rabolt, and C. Marcott, "AFM–IR: combining atomic force microscopy and infrared spectroscopy for nanoscale chemical characterization," *Applied Spectroscopy*, vol. 66, no. 12, pp. 1365–1384, 2012.

[13] F. Huth, M. Schnell, J. Wittborn, N. Ocelic, and R. Hillenbrand, "Infrared-spectroscopic nanoimaging with a thermal source," *Nature Materials*, vol. 10, no. 5, pp. 352–356, 2011.

[14] A. Hartschuh, "Tip-enhanced near-field optical microscopy," *Angewandte Chemie International Edition*, vol. 47, no. 43, pp. 8178–8191, 2008.

[15] J. Stadler, B. Oswald, T. Schmid, and R. Zenobi, "Characterizing unusual metal substrates for gap-mode tip-enhanced Raman spectroscopy," *Journal of Raman Spectroscopy*, vol. 44, no. 2, pp. 227–233, 2013.

[16] S. F. Becker, M. Esmann, K. Yoo, P. Gross, R. Vogelgesang, N. Park, and C. Lienau, "Gap-plasmon-enhanced nanofocusing near-field microscopy," *ACS Photonics*, vol. 3, no. 2, pp. 223–232, 2016.

[17] B. Pettinger, K. F. Domke, D. Zhang, R. Schuster, and G. Ertl, "Direct monitoring of plasmon resonances in a tip-surface gap of varying width," *Physical Review B*, vol. 76, no. 11, p. 113409, 2007.

[18] B. Pettinger, K. F. Domke, D. Zhang, G. Picardi, and R. Schuster, "Tip-enhanced Raman scattering: influence of the tip-surface geometry on optical resonance and enhancement," *Surface Science*, vol. 603, no. 10, pp. 1335–1341, 2009.

[19] K. Tanaka and M. Tanaka, "Simulations of nanometric optical circuits based on surface plasmon polariton gap waveguide," *Applied Physics Letters*, vol. 82, no. 8, pp. 1158–1160, 2003.

[20] K. Tanaka, M. Tanaka, and T. Sugiyama, "Simulation of practical nanometric optical circuits based on surface plasmon polariton gap waveguides," *Optics Express*, vol. 13, no. 1, pp. 256–266, 2005.

[21] B. Wang and G. P. Wang, "Metal heterowaveguides for nanometric focusing of light," *Applied Physics Letters*, vol. 85, no. 16, pp. 3599–3601, 2004.

[22] B. Wang and G. P. Wang, "Surface plasmon polariton propagation in nanoscale metal gap waveguides," *Optics Letters*, vol. 29, no. 17, pp. 1992–1994, 2004.

[23] F. Kusunoki, T. Yotsuya, J. Takahara, and T. Kobayashi, "Propagation properties of guided waves in index-guided two-dimensional optical waveguides," *Applied Physics Letters*, vol. 86, no. 21, p. 211101, 2005.

[24] W. L. Barnes, A. Dereux, and T. W. Ebbesen, "Surface plasmon subwavelength optics," *Nature*, vol. 424, no. 6950, pp. 824–830, 2003.

[25] A. V. Zayats, I. I. Smolyaninov, and A. A. Maradudin, "Nano-optics of surface plasmon polaritons," *Physics Reports*, vol. 408, no. 3, pp. 131–314, 2005.

[26] G. W. Ford and W. H. Weber, "Electromagnetic interactions of molecules with metal surfaces," *Physics Reports*, vol. 113, no. 4, pp. 195–287, 1984.

[27] J. R. Lakowicz, "Radiative decay engineering 5: metal-enhanced fluorescence and plasmon emission," *Analytical Biochemistry*, vol. 337, no. 2, pp. 171–194, 2005.

[28] R. Ramos and M. Gordon, "Near-field artifacts in tip-enhanced Raman spectroscopy," *Applied Physics Letters*, vol. 100, no. 21, p. 213111, 2012.

[29] R. Zhang, Y. Zhang, Z. Dong, S. Jiang, C. Zhang, L. Chen, L. Zhang, Y. Liao, J. Aizpurua, Y. e. Luo, *et al.*, "Chemical mapping of a single molecule by plasmon-enhanced Raman scattering," *Nature*, vol. 498, no. 7452, pp. 82–86, 2013.

[30] C. Lumdee, B. Yun, and P. G. Kik, "Gap-plasmon enhanced gold nanoparticle photoluminescence," *ACS Photonics*, vol. 1, no. 11, pp. 1224–1230, 2014.

[31] A. Mooradian, "Photoluminescence of metals," *Physical Review Letters*, vol. 22, no. 5, p. 185, 1969.

[32] M. Chaigneau, G. Picardi, and R. Ossikovski, "Tip enhanced Raman spectroscopy evidence for amorphous carbon contamination on gold surfaces," *Surface Science*, vol. 604, no. 7, pp. 701–705, 2010.

Chapter 6

Summary and future directions

6.1 Summary of results

The previous chapters discussed in detail the design, validation, and application of a TENOM instrument that can study a wide variety of near-field optical phenomena. In particular, we demonstrated the instrument's exceptional sensitivity to the subtle interactions between the TENOM tip and evanescent fields above the sample surface. Before concluding this thesis with a discussion of potential instrument modifications and future applications, we briefly recapitulate the key results and conclusions of the previous chapters.

The TENOM instrument described in this work consists of three main components: (i) a heavily modified commercial AFM, (ii) a compact confocal Raman microscope, and (iii) a custom ATR-geometry excitation/detection system. In Chapter 2, we first discussed the design of a heavily modified commercial AFM with optical access for the side-on Raman microscope, as well as side-view and top-view observation cameras. The performance of the AFM was assessed by imaging several test structures that spanned a range of lengthscales, and we confirmed the instrument's ability to regulate tip height

over large and small scan areas, as well as at small force setpoints (< 1 nN). The design of the Raman microscope was also described, along with the results of several validation studies that were used to quantify its performance. The most important among these were the point spread function and depth-of-field measurements, which were used to assess the in-plane ($1.3\ \mu m\ \times\ 3.1\ \mu m$) and out-of-plane ($< 10\ \mu$m) spatial resolution of the optical system, respectively. Finally, through combined operation of the Raman microscope and the AFM, along with the use of a plasmonically active TENOM tip, a TERS line scan was performed on a sample of functionalized Au nanotriangles, and sub-diffraction-limited spatial resolution was successfully demonstrated.

In Chapter 3, we discussed the development and evaluation of the TENOM instrument's third component, the so-called ATR system, which was added to expand the capabilities and sensitivity of the instrument. The performance of the ATR system was quantitatively assessed by measuring the angle-dependent reflectance of several model systems (e.g., a glass-air interface and a glass-Cr-Au-air stack) and comparing the results to theoretical predictions determined from the Fresnel equations. The validation process also involved the development and refinement of FDTD optical simulations that accurately reproduced the experimental behavior of the system and provided a valuable method for predicting and understanding results for the more complex systems discussed in Chapters 4 and 5. Lastly, the validation studies of the ATR system demonstrated that the instrument could be used to both excite SPPs at a Au-air interface and detect shifts in the SPP resonance due to small changes in the dielectric properties at the sample surface.

In Chapter 4, the AFM, Raman microscope, and ATR system were combined in a variety of arrangements to showcase the broad capabilities of the TENOM instrument. By performing approach curves above a glass-air interface during ATR excitation in the TIR regime, the TENOM tip was shown to transduce the local evanescent field, leading to an

increase in elastic tip scattering (as measured by the Raman microscope) and a decrease in the reflectance of the sample (as measured by the ATR system) proportional to the local strength of the optical field. In this way, the spatial extent of the evanescent field was directly measured, and its profile was shown to match theory quantitatively. Another important demonstration of the instrument's abilities involved the study of SPP-enhanced Raman scattering from a thin CuPc layer on a Au/Cr/glass substrate. Not only was it shown that the use of resonantly-excited SPPs could lead to an order-of-magnitude increase in Raman scattering from surface adsorbates, but the results were also in excellent qualitative agreement with FDTD predictions of the angle-of-incidence-dependent E-field intensity at the sample surface. Lastly, the combined TENOM instrument was used to perform TERS line scans across a chemically and topographically patterned sample of CuPc on Au/Cr/glass using two different illumination schemes (i.e., side-on and ATR-mode) in order to critically assess their relative performance. It was determined that both illumination geometries demonstrated spatial resolutions of < 40 nm and enhancement factors of roughly 6500. Furthermore, the ATR illumination yielded similar absolute Raman signal levels at lower "effective" pump powers due to SPP-mediated delivery of additional optical energy into the tip-surface gap region.

Finally, in Chapter 5, we demonstrated the TENOM instrument's ability to investigate the nuanced optical behavior of the tip-surface system over a range of tip-surface distances. In particular, we showed that through careful measurements of sample reflectance and tip scattering at small tip-surface distances, the instrument could detect the emergence of a resonant gap plasmon mode that dramatically altered the optical behavior of the system. FDTD simulations were successfully used to reproduce experimental trends and corroborate the hypothesized mechanisms. Most importantly, the spectral response of the gap plasmon was also studied, and the results showed that the resonance of the gap plasmon had a strong effect on the enhancement of both fluorescence

and Raman scattering. This result has significant implications regarding the operation and practical applications of this TENOM instrument moving forward.

6.2 Future directions

In the remainder of this chapter, we present several potential directions in which this project could be continued, organized in roughly ascending order by the scope of the endeavor.

6.2.1 Observation of water meniscus formation

Capillary condensation of water in the nanocavity between a sharp tip and a surface is a common and well-understood phenomenon when performing AFM experiments under ambient conditions [1–3]. This condensation leads to the formation of a water meniscus that encompasses a portion of the tip apex. As was clearly demonstrated by the results of Chapter 5, the TENOM instrument is remarkably sensitive to the optical behavior of the coupled tip-surface system, and this behavior depends critically on the local dielectric environment in the tip-surface gap. One might, therefore, expect the instrument to be well suited to directly observe and study the formation of such a meniscus by measuring changes in the reflectance, scattering, and spectral response of the system while the tip and surface are held in close proximity.

Occasionally, an approach curve will appear to contain hints of this phenomenon in the form of reflectance and scattering fluctuations immediately after snap-on. In these cases, the cantilever deflection (T–B) and tip-surface voltage (V_{t-s}) signals can provide important additional insight into the state of the tip-surface junction at each time point, and often display apparent contradictions that are difficult to reconcile *unless* a water meniscus was present in the gap. For example, these signals often reveal that the moment

of snap-on as detected by the cantilever deflection is not always concurrent with the moment of conductive contact between the tip and surface, as determined by V_{t-s}. This suggests that despite the mechanical adhesion forces holding the tip on the surface after snap-on, an insulating physical gap still exists between them. Furthermore, as the tip is moved toward the surface, it is common that the reflectance and scattering signals change considerably in the time between the initial mechanical snap-on event and the point of conductive contact, after which time they remain roughly constant.

This behavior is demonstrated in Figure 6.1, where the reflectance and scattering profiles of an approach curve are shown alongside the corresponding T–B profile; the trends displayed by the latter are particularly insightful in this case. Because the AFM cantilever can be reasonably approximated as a spring, one should expect a rigid mechanical interaction between the tip and surface to result in a linear relation between the cantilever's position and its deflection after snap-on (blue line in Figure 6.1 (a)). The T–B profile clearly deviates from this behavior; this could be explained by the formation of a water meniscus whose associated capillary force pulls the tip toward the surface but not into rigid mechanical contact. This rapid change in tip-surface distance at snap-on, along with the change in the dielectric properties of the medium in the gap (i.e., from air to water), leads to the simultaneous jump in the reflectance and scattering behavior of the tip-surface system. As the tip continues its approach and the tip-surface distance is reduced further, the reflectance and scattering behavior change until rigid mechanical contact occurs (determined by the linear position-deflection relation).

Although these results help corroborate the likely hypothesis that a water meniscus forms in the tip-surface junction during TENOM experiments, additional experiments are still necessary to fully understand this behavior. Perhaps the most unique capability of the present TENOM instrument is its sensitivity to the plasmonic behavior of the tip-surface system, namely its ability to directly monitor resonant gap plasmon excita-

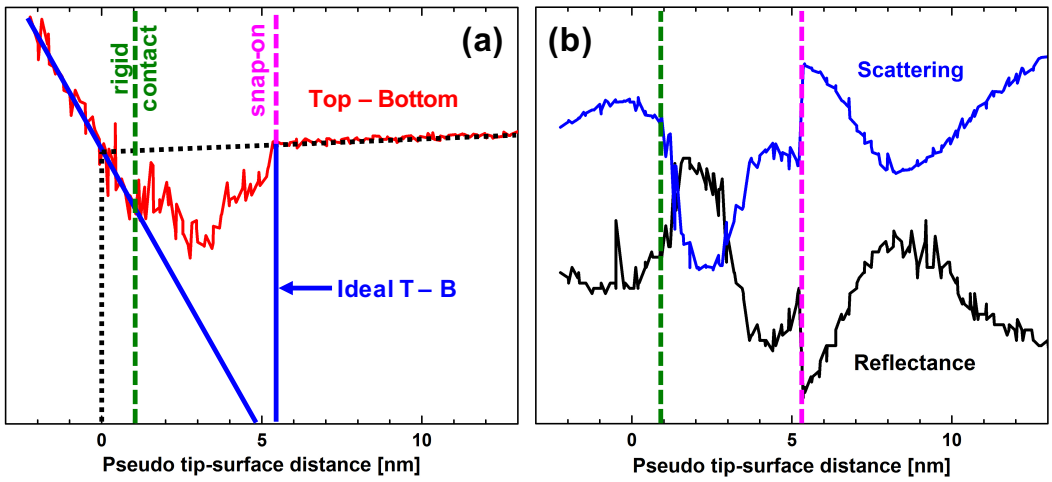

Figure 6.1: **Influence of a water meniscus on approach curve measurements.** (a) Top – botttom (T–B) and (b) scattering and reflectance profiles from a TENOM approach curve measurement that demonstrate artifacts suggestive of a water meniscus in the tip-surface gap. Difference between experimental (red) and ideal (blue) T–B profiles indicates non-rigid mechanical interaction between tip and surface from ∼1–5 nm, and reflectance and scattering signals show large variations over the same range. Rigid contact regime (left of green dashed line) determined by linear trend in T–B signal; reflectance and scattering also show roughly constant behavior in this regime. Note: x-axis does not accurately represent true tip-surface separation to the left of "snap-on" (pink dashed line).

tion. Therefore, using the instrument to study similar phenomena to those discussed in Chapter 5 (e.g., gap plasmon resonance and the associated spectral response) in a system containing a water meniscus could provide insights into the influence of capillary condensation on ambient TENOM measurements. By investigating the effects of variables like humidity and surface hydrophobicity on the gap plasmon resonance and spectroscopic enhancement, one could demonstrate the practical relevance of water meniscus formation in the design and interpretation of TENOM results. Furthermore, if water meniscus formation is determined to be detrimental to TENOM measurements, tip and/or substrate surface treatments (e.g., hydrophobic self-assembled monolayer coatings [1, 4]) could also be investigated to prevent capillary condensation and improve the performance of the TENOM instrument in ambient conditions.

6.2.2 Instrument modifications

Unfortunately, because of the strength of the adhesive forces associated with water meniscus formation, it is very challenging to perform the experiments described above with a cantilever-based AFM system. Due to the flexibility of the cantilever, the combination of capillary and van der Waals forces unavoidably pull the tip into proximity with the surface during snap-on, effectively skipping over the final ∼5 nm of the approach curve and precluding the careful study of the tip-surface optical behavior in this crucial range. The inability to accurately probe the small tip-surface distance regime ($z < 5$ nm) is a considerable limitation of the instrument that, if corrected, would dramatically improve its functionality and versatility. The most straightforward approach to resolving this inadequacy would be to retrofit the AFM to enable operation in a STM mode, in which the tunneling current between a rigid tip (no cantilever) and the sample would be used for z-piezo feedback. In addition to avoiding the troublesome snap-on issue, the use of STM feedback would enable direct and accurate measurements of tip-surface distance at small z instead of relying on indirect approximations inferred from the approach curves, as is necessarily the case for the current cantilever-based system. Alternatively, sheer-force AFM techniques, which use the tip's lateral oscillation frequency for feedback, could also be employed to achieve a similar level of tip-surface distance control. Furthermore, they could provide additional insight into water meniscus formation dynamics through changes in the resonance of the tip's lateral oscillations.

Fine control of the tip-surface distance in the small z regime would likely produce additional insights that would complement the results of Chapter 5. As those results clearly showed, the influence of tip-surface distance on the system's spectroscopic behavior becomes increasingly pronounced at small z. Thus, it is not unlikely that significant plasmonic events (e.g., higher-order resonances with corresponding spectroscopic effects)

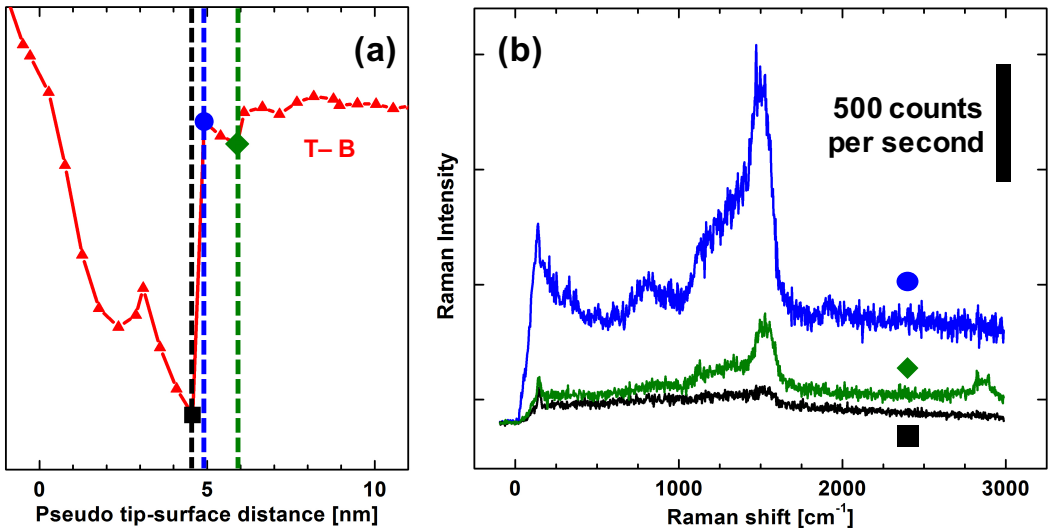

Figure 6.2: **Raman enhancement during snap-on.** Results from a TENOM approach curve measurement showing three Raman spectra (b) taken before (green, ◊), during (blue, ◯), and after (black, □) snap-on, as shown in the top – bottom (T–B) profile in (a). Data demonstrate a dramatic increase in Raman enhancement at the moment of snap-on followed by an equally sharp decrease, and suggest the existence of a strong plasmonic resonance in the tip-surface distance range of 0–5 nm. Note: x-axis in (a) does not accurately represent true tip-surface separation to the left of "snap-on" (blue dashed line).

can occur in the distance regime skipped due to snap-on. In fact, there is fleeting evidence of this in some approach curves, like that shown in Figure 6.2. It is commonly observed in these experiments that the optical spectra taken during snap-on and snap-off (if the events occur while the Raman microscope is acquiring signal) show extraordinarily strong Raman enhancement, in some cases an order of magnitude more than any other spectrum in the entire scan. This suggests that for a brief moment during snap-on/-off, the tip-surface system exhibits an extremely strong resonant behavior that dramatically enhances Raman scattering. If this is indeed the case, STM-mode operation would not only allow us to probe this behavior carefully, but it would also enable optimization of the tip-surface distance during TENOM imaging experiments to make use of this Raman enhancement and achieve stronger signal, shorter collection times and/or higher pixel density scans.

Another potential benefit of STM-mode operation is that it enables direct spectroscopic measurement of the gap plasmon's frequency response by studying the light emitted from the tip-surface junction due to inelastic electron tunneling (IET) [5, 6]. Because this light emission process is facilitated by strong interactions between tunneling electrons and localized plasmon modes, the light emission characteristics (i.e., wavelength dependence) depend strongly on the plasmonic response of the tip-surface system. Thus, IET could provide an additional pathway by which to observe changes in the gap plasmon resonance of the system as a function of tip-surface distance and/or water meniscus formation.

Along the same vein, modifying the instrument to enable white light ATR measurements could also allow direct observation of gap plasmon resonances in a similar way. It has been previously reported that when a plasmonic tip is lowered into a broadband evanescent field, the wavelength-dependent scattering echoes the frequency response of the tip's LSP modes [7, 8]; this is in keeping with the results of Chapter 5, particularly the FDTD scattering profiles. The present instrument is particularly well suited to make use of this phenomenon not only to observe changes in the gap plasmon resonance as a function of tip-surface distance but also to characterize the plasmonic behavior of each TENOM tip in the absence of any convolving effects caused by a nearby sample surface. By directly measuring and quantifying the scattering properties of different tips in free space and correlating these properties with its preparation conditions, geometry, and TENOM performance, one could rapidly evaluate each tip's quality and optimize tip preparation procedures to maximize signal enhancement.

6.2.3 TENOM applications

The directions proposed above primarily focus on improving our understanding of the factors that influence the system's optical response and leveraging those insights to optimize spectroscopic enhancement through the careful tuning of resonant plasmonic modes. To complement these fundamental studies, it is important to also consider practical applications that would make use of our findings to enable valuable new characterization experiments. Thus, this section will highlight a few potential systems toward which the TENOM instrument could ultimately be applied and in which the signal enhancements discussed above would be critical for its success.

Perhaps the most promising field for the application of TENOM techniques is the study of biological surfaces, particularly the mapping of chemical functionalities on multifunctional surfaces with nanoscale spatial resolution [9–13]. Biological systems are challenging to study at the nanoscale for many reasons, and each measurement technique has associated strengths and shortcomings. TERS is attractive for these applications because of the richness of the chemical information attainable through Raman spectroscopy. However, the nearly ubiquitous tendency of biological materials to fluoresce often leads to overwhelming optical background emissions that inhibit the detection of the desired Raman signal. Nevertheless, this obstacle can be overcome if sufficiently large Raman enhancements are achieved. As discussed above, a few straightforward instrument modifications could enable precise tuning of the gap plasmon resonance, and preliminary results suggest that this optimization process could yield an order of magnitude increase in Raman enhancement. If this is indeed the case, then it will dramatically improve the instrument's potential for applications in biological systems. Logical targets for initial proof-of-concept and sensitivity studies in this realm include monolayers of nucleobases or peptides, DNA or RNA strands, and supported lipid bilayers.

Another practically relevant field toward which the TENOM instrument could potentially be applied is the study of inorganic semiconductor materials. In addition to its sensitivity toward molecular vibration energies, Raman spectroscopy can also measure the energies of optical phonons in crystalline materials, which can be related to properties such as defect density and lattice strain. In this way, it has been shown that TERS can be used to spatially resolve variations in the local crystal properties of semiconductor nanowires and structured semiconductor surfaces, making it a valuable characterization technique for these materials [14–16]. Applying the present TENOM instrument to similar semiconductor applications would require careful consideration of several factors. First, many of the key results discussed herein are a consequence of the intense optical fields that arise because of the strong-coupling interaction between the tip and the surface. If the TENOM instrument was used to investigate, for example, a semiconductor layer or nanowire whose height was larger than $\sim$10 nm, the resulting tip-substrate spacing would be too large to support a resonant gap plasmon and the associated benefits would be lost. Thus, the instrument is ideally suited only for the study of very small/thin nanostructures, such as nanoplatelets or thin films, though larger/thicker structures could still be interrogated, albeit with considerably lower sensitivity. Additionally, if TENOM measurements of semiconductor materials were performed in the resonant gap plasmon regime, it would be important to carefully consider the effect of the semiconductor's presence on the optical behavior of the plasmon mode. As in the case of the water meniscus formation, the local dielectric environment near the tip apex can dramatically affect the optical response of the system and must be accounted for.

6.3 Conclusion

In this work, we have described in detail the design, construction, and rigorous validation of a TENOM instrument with a unique ATR-geometry excitation/detection system, which can perform a wide variety of near-field optical experiments. We assessed the instrument's ability to controllably excite and spatially probe evanescent phenomena, such as SPPs, near the sample surface and showed that experimental observations were consistent with both theory and FDTD simulations. Furthermore, we successfully applied the TENOM instrument to perform local chemical interrogation of a nanostructured, chemically-patterned surface and demonstrated its ability to locally enhance Raman scattering and measure surface chemistry with sub-diffraction-limited spatial resolution. By repeating this chemical imaging experiment using two different excitation geometries (i.e., side-on and ATR-mode), we were able to quantitatively compare their relative signal strengths, enhancement factors, and spatial resolutions and show that the novel ATR illumination scheme yielded comparable results. Finally, we used the TENOM instrument to study the optical behavior of the coupled tip-surface system over a range of separation distances and demonstrated the instrument's excellent sensitivity toward subtle changes in the plasmonic response of the tip-surface gap. In particular, we showed that the instrument could detect the resonant excitation of a gap plasmon mode and that the properties of this mode have important consequences regarding the enhancement of fluorescence and Raman scattering. Moving forward, we proposed two potential modifications that could dramatically expand the instrument's capabilities and facilitate important fundamental studies of the system's behavior at small tip-surface distances. Preliminary evidence suggests that these fundamental studies could yield dramatic improvements in signal strength and sensitivity, which would pave the way to practical applications of the TENOM instrument in the fields of biology and materials science.

References

[1] X. Xiao and L. Qian, "Investigation of humidity-dependent capillary force," *Langmuir*, vol. 16, no. 21, pp. 8153–8158, 2000.

[2] S. Rozhok, P. Sun, R. Piner, M. Lieberman, and C. A. Mirkin, "Afm study of water meniscus formation between an AFM tip and NaCl substrate," *The Journal of Physical Chemistry B*, vol. 108, no. 23, pp. 7814–7819, 2004.

[3] B. L. Weeks, M. W. Vaughn, and J. J. DeYoreo, "Direct imaging of meniscus formation in atomic force microscopy using environmental scanning electron microscopy," *Langmuir*, vol. 21, no. 18, pp. 8096–8098, 2005.

[4] U. Srinivasan, M. R. Houston, R. T. Howe, and R. Maboudian, "Alkyltrichlorosilane-based self-assembled monolayer films for stiction reduction in silicon micromachines," *Journal of Microelectromechanical Systems*, vol. 7, no. 2, pp. 252–260, 1998.

[5] J. Lambe and S. McCarthy, "Light emission from inelastic electron tunneling," *Physical Review Letters*, vol. 37, no. 14, p. 923, 1976.

[6] R. Berndt, J. K. Gimzewski, and P. Johansson, "Inelastic tunneling excitation of tip-induced plasmon modes on noble-metal surfaces," *Physical review letters*, vol. 67, no. 27, p. 3796, 1991.

[7] C. Neacsu, G. Steudle, and M. Raschke, "Plasmonic light scattering from nanoscopic metal tips," *Applied Physics B*, vol. 80, no. 3, pp. 295–300, 2005.

[8] D. Mehtani, N. Lee, R. Hartschuh, A. Kisliuk, M. Foster, A. Sokolov, F. Čajko, and I. Tsukerman, "Optical properties and enhancement factors of the tips for apertureless near-field optics," *Journal of Optics A: Pure and Applied Optics*, vol. 8, no. 4, p. S183, 2006.

[9] U. Neugebauer, P. Roesch, M. Schmitt, J. Popp, C. Julien, A. Rasmussen, C. Budich, and V. Deckert, "On the way to nanometer-sized information of the bacterial surface by tip-enhanced Raman spectroscopy," *ChemPhysChem*, vol. 7, no. 7, pp. 1428–1430, 2006.

[10] K. F. Domke, D. Zhang, and B. Pettinger, "Tip-enhanced Raman spectra of picomole quantities of DNA nucleobases at Au (111)," *Journal of the American Chemical Society*, vol. 129, no. 21, pp. 6708–6709, 2007.

[11] A. Rasmussen and V. Deckert, "Surface-and tip-enhanced Raman scattering of DNA components," *Journal of Raman Spectroscopy*, vol. 37, no. 1-3, pp. 311–317, 2006.

[12] E. Bailo and V. Deckert, "Tip-enhanced Raman spectroscopy of single RNA strands: Towards a novel direct-sequencing method," *Angewandte Chemie International Edition*, vol. 47, no. 9, pp. 1658–1661, 2008.

[13] L. Opilik, T. Bauer, T. Schmid, J. Stadler, and R. Zenobi, "Nanoscale chemical imaging of segregated lipid domains using tip-enhanced Raman spectroscopy," *Physical Chemistry Chemical Physics*, vol. 13, no. 21, pp. 9978–9981, 2011.

[14] Y. Saito, M. Motohashi, N. Hayazawa, M. Iyoki, and S. Kawata, "Nanoscale characterization of strained silicon by tip-enhanced Raman spectroscope in reflection mode," *Applied Physics Letters*, vol. 88, no. 14, p. 143109, 2006.

[15] N. Hayazawa, M. Motohashi, Y. Saito, H. Ishitobi, A. Ono, T. Ichimura, P. Verma, and S. Kawata, "Visualization of localized strain of a crystalline thin layer at the nanoscale by tip-enhanced Raman spectroscopy and microscopy," *Journal of Raman Spectroscopy*, vol. 38, no. 6, pp. 684–696, 2007.

[16] S. Berweger, C. C. Neacsu, Y. Mao, H. Zhou, S. S. Wong, and M. B. Raschke, "Optical nanocrystallography with tip-enhanced phonon Raman spectroscopy," *Nature Nanotechnology*, vol. 4, no. 8, pp. 496–499, 2009.